Nonlinear optical spectroscopy of exciton-polaritons in Cu_2O, ZnSe and semiconductor quantum wells

Dissertation

presented to the Faculty of Physics of the
TU Dortmund University, Germany,
in partial fulfilment of the requirements
for the degree of

Dr. rer. nat.

by

Johannes Mund

Dortmund, August 2019

Accepted by the Faculty of Physics of the TU Dortmund University, Germany

Day of the oral examination: 8th November 2019

Examination board:
Prof. Dr. Dmitri R. Yakovlev
Prof. Dr. Markus Betz
Prof. Dr. Matthias Schneider
Dr. Bärbel Siegmann

Contents

Summary

The goal of this thesis is to gain fundamental information about exciton states in semiconductor materials by nonlinear optical spectroscopy. Excitons are present in the energy range below the material's band gap, where they dominate the optical properties. In contrast to linear optics, states are excited by two, or more photons. The process of excitation and emission is a coherent one. That is, the emitted photon contains the sum of k-vectors and the sum of energies of the incoming photons.

As the generation of harmonics is particularly efficient at exciton resonances, these can be identified as maxima in the spectra. Therein, harmonic intensity is plotted in dependence of emission energy. Furthermore, the intensity is detected in dependence of polarizations of incoming and outgoing photons. Thus, excitation selection rules are determined which are in general complementary to those in linear optics. This allows to trace mixing of states in case of external perturbations, e.g. in magnetic fields.

First of all, a new method of harmonic exciton spectroscopy is presented in this thesis. By spectrally broad femtosecond laser-pulses, several exciton resonances are detected at once. In contrast to measurements by nano- or picosecond pulses, there is no need for tuning the laser emission wavelength. Thus, the time consumption of experiments is reduced. Advantages and drawbacks of both methods are discussed.

In the following, measurements on Cu_2O are presented. This material is known to show excitons of high principal quantum number n. Indeed, states up to $n = 9$ are observed in second harmonic generation. Excitation mechanisms are discussed by analysis of selection rules. Furthermore, the implications of internal strain in the samples on the 1S exciton and exciton lifetime measurements in magnetic field are investigated.

Experiments in ZnSe samples demonstrate the influence of the exciton-polariton dispersion on the 1S exciton resonance. An energy shift is observed, depending on the exciting photon wavelength.

For the first time, second and third harmonic spectra are presented for multiple quantum well structures. These are of interest, as the energy levels of excitons can be tailored by well width and material compositions of well and barrier.

Firstly, a ZnSe/BeTe structure of type-II band alignment is investigated. Therein, electrons and holes are confined in deep barrier potentials. Secondly, measurements on a set of ZnO/(Zn,Mg)O structures of well widths between 1.8 and 10 nm are presented. In this type-I structure, energy shifts of confined exciton resonances and effects of internal electric fields are documented.

Zusammenfassung

Das Ziel dieser Arbeit ist es, durch nichtlineare optische Spektroskopie grundlegende Informationen über Exziton-Zustände in Halbleiter-Materialien zu erhalten. Exzitonen treten im Energiebereich unterhalb der Bandlücke des Materials auf und dominieren dort die optischen Eigenschaften. Im Unterschied zur linearen Optik geschieht die Anregung im nichtlinearen Fall durch zwei, oder mehr Photonen. Dabei ist die Erzeugung der zweiten und höheren Harmonischen ein kohärenter Prozess. Somit erhalten die emittierten Photonen jeweils die Summen der k-Vektoren und Energien der einge-strahlten Photonen.

Da die Erzeugung der Harmonischen bei den Resonanz-Energien der Exzitonen besonders effektiv ist, können diese als Maxima in Spektren identifiziert werden. Diese zeigen in Abhängigkeit der Emissions-Energie die Intensität der Harmonischen. Zudem wird die Intensität in Abhängigkeit der Polarisationen der eingestrahlten und emittierten Photonen gemessen. Hierdurch werden Auswahlregeln der Zustände ermittelt, die komplementär zu denen in linearer Optik sind. Insbesondere können Mischungen von Zuständen bei externen Störungen, etwa magnetischen Feldern untersucht werden.

Zunächst wird in dieser Arbeit eine neue Methode vorgestellt, wie mit spektral breiten Femtosekunden Laserpulsen Spektren von mehreren Exzitonresonanzen aufgenommen werden können. Im Gegensatz zur Messung mit Nano- oder Pikosekunden-Pulsen muss dabei die Emissions-Wellenlänge des Lasers nicht durchgestimmt werden, was eine große Zeitersparnis birgt. Vor- und Nachteile beider Methoden werden diskutiert.

Anschließend werden Messungen an Cu_2O vorgestellt, das dafür bekannt ist, dass Exzitonen mit hohen Hauptquantenzahlen n beobachtet werden können. So werden Zustände bis $n = 9$ in zweiter Harmonischer detektiert. Zudem werden an Hand der Auswahlregeln die Mechanismen diskutiert, durch die die zweite Harmonische erzeugt wird. Weiterhin werden der Einfluss von internen Verspannungen in den Proben auf das 1S Exziton und die Messung der Exziton-Lebensdauer im Magnetfeld untersucht.

Experimente an ZnSe-Proben demonstrieren, dass die Exziton-Polariton Dispersion für energetische Verschiebungen der 1S Exzitonresonanz in Abhängigkeit der eingestrahlten Wellenlänge verantwortlich ist.

Weiterhin werden erstmalig Spektren der Exzitonen in zweiter und dritter Harmonischer in Quantentrogstrukturen gezeigt. In diesen lassen sich die Energieniveaus von Exzitonen durch Trogbreiten und Barrieren-Potentiale gezielt beeinflussen.

Zum einen ist dies eine ZnSe/BeTe-Struktur, deren Bänder in Typ-II Ordnung vorliegen und sich Elektronen, sowie Löcher in tiefen Potentialtrögen befinden. Zum anderen wird ein Satz von ZnO/(Zn,Mg)O-Trögen mit Breiten zwischen 1.8 und 10 nm untersucht. In dieser Typ-I Struktur werden insbesondere Energieverschiebungen der Zustände durch Quantisierung deutlich, sowie Effekte durch interne elektrische Felder.

1 Introduction

Investigation of nonlinear effects has become a broad field of research in modern optics [1, 2] with a manifold of applications. One main area is frequency conversion. Laser radiation of certain wavelengths and lasers with tunable emission wavelengths were not possible without nonlinear effects. Even supposedly simple devices as a laser pointer are based on the conversion of two photons of infrared wavelength to one photon of higher energy in the green spectral range.

Nonlinear effects were described theoretically in the 1930's, decades before first experiments could be carried out. A prerequisite for successful nonlinear experiments was the invention of the laser by Maiman *et al* [3] in 1960, who was awarded the noble price in physics for the ruby laser in 1964. Only then, sufficiently intense light fields were feasible which are necessary to investigate nonlinear effects that show in general low efficiency.

Shortly after, first experiments in solid state spectroscopy in the field of nonlinear optics were performed. Franken *et al.* [4] measured second harmonic generation (SHG) from a quartz crystal in 1961 and two-photon absorption (TPA) was shown in CaF_2:Eu^{2+} [5] and KI [6, 7] which was predicted by Maria Göppert-Mayer already in 1931 [8]. An enormous diversity has developed since the 1960's of which some are mentioned in Ref. [9]. There are methods similar to SHG, like sum and difference frequency generation and those which involve a fourth transition like third harmonic generation (THG) and various types of experiments that involve Raman scattering, e.g. stimulated Raman scattering [10].

The focus of this thesis is set to SHG and THG, wherein two (three) photons are absorbed by the crystal and one photon of twice (triple) energy is emitted. By the use of a laser system with widely tunable emission wavelength, spectra of semiconductor bulk material and quantum well structures are investigated. The spectral range close to the respective band gap of a material is of particular interest. There, fundamental crystal states are located that comprise an excited electron in the conduction band which is coupled to the remaining hole in the valence band by Coulomb-interaction. This two-particle state is called an exciton and is located energetically below the semiconductor band gap energy by the value of its binding energy.

It was found that the conversion process of fundamental light frequency to twice, or tripple, frequency is especially efficient at exciton resonances. Still, to observe an exciton resonance in a SHG spectrum, several conditions have to be fulfilled. First of all, the exciton state under investigation has to be two-photon allowed. That is, absorption of two photons of proper polarization needs to be allowed by symmetry arguments. This step equals the TPA experiments. Secondly, for SHG, the emission of one photon from

the same state has to be allowed at the same time. Therefore, stricter conditions apply to a state in order to be observable in SHG as compared to TPA. In principle, these conditions originate from wavefunction symmetries and can be predicted in terms of the group theory. It is used extensively throughout this thesis to analyse the symmetries of states and propose involved mechanisms.

In experiment, information on exciton symmetries are attained by detecting the SHG intensity in dependence of photon polarization angles. These polar diagrams, so called rotational anisotropies, provide a powerful tool for symmetry analysis of excitons, particularly under influence of perturbations, such as strain and magnetic fields [11]. A recent overview of exciton spectroscopy can be found in [12].

In former work [13–16], the light wavelength of a nanosecond laser system was scanned at half the photon energy of the exciton resonances to detect SHG. The resolution in the spectra was determined by the laser linewidth. In this thesis, the new technique of exciton spectroscopy by a femtosecond laser with spectrally broad laser pulses is introduced. Thereby, no scanning of the laser wavelength is necessary. Measurements are done much faster with this technique while the resolution depends on the detection system.

By this method, measurements on excitons in Cu_2O and ZnSe bulk crystals are presented in this thesis. For Cu_2O, the effect of internal strain is considered and the exciton lifetime in magnetic field determined. The resonance energy of the 1S exciton in ZnSe is shown to be influenced by the exciton-polariton dispersion.

When reducing a sample from a bulk crystal to quantum wells of several nm width, i.e. from three to two dimensions, a whole new field of research is opened up [17]. The first to propose a quantum well structure were Esaki and Tsu in 1970 [18], after growth of thin layers of high quality was feasible by molecular beam epitaxy and metal-organic chemical vapour deposition. In such structures, electrons and holes are restricted to two dimensions, giving rise to effects as the quantized hall effect [19] and applications as the quantum cascade laser [20]. Excitons are influenced by the reduced dimensionality, too. Their motion is quantized in the well growth direction whereas it is continuous in the plane perpendicular to it. The presence of internal electric fields due to carriers separated in the well and barrier layers, or piezoelectric effects from strain in the interfaces between the layers affect the excitons.

In this thesis, ZnSe/BeTe and Zn/(Zn,Mg)O multiple quantum well (MQW)s are investigated. Mechanisms responsible for SHG and THG are deduced from comparison to linear measurements (photoluminescence (PL)) and symmetry analysis.

2 Theory

In this section, basic theoretical concepts shall be presented that are required for understanding the excitation processes throughout this thesis. Further theory which is necessary for particular materials only, is given in the corresponding sections. Starting from the Maxwell Equations, the nonlinear polarization, induced in a medium, is discussed. It is closely related to susceptibility tensors of different order which, in turn, can be defined by matrix transition elements. The operators in these elements arise directly from the light-matter interaction that is responsible for exciton generation. In the case of strong coupling of light and excitons, the regime of exciton-polaritons is entered leading to a manifold of new phenomena. Finally, the process of SHG is introduced along with the group theory formalism which is a powerful tool to predict possible experimental outcomes. In each section, textbooks are cited which were used to design the parts and where further information can be found.

2.1 Maxwell equations and nonlinear polarization

The Maxwell equations build the bedrock of electrodynamics. They describe the relations of electric and magnetic fields in vacuum and media, such as semiconductors. Here, as a starting point for the theory [2, pp.70 ff.], they are given in their differential macroscopic form, letters in bold print denote vector quantities:

$$\nabla \cdot \mathbf{D} = \rho, \tag{2.1}$$

$$\nabla \cdot \mathbf{B} = 0, \tag{2.2}$$

$$\nabla \times \mathbf{E} = -\frac{\partial}{\partial t}\mathbf{B}, \tag{2.3}$$

$$\nabla \times \mathbf{H} = \mathbf{j} + \frac{\partial}{\partial t}\mathbf{D}, \tag{2.4}$$

with $\nabla = (\partial_x,\, \partial_y,\, \partial_z)^{\mathrm{T}}$, the nabla operator, ρ and $\mathbf{j}$, the densities of free charges and free currents in the material which are both set to zero here. $\mathbf{E}$ and $\mathbf{H}$ are the electric and magnetic field strength, respectively. The electric displacement $\mathbf{D}$ comprises the applied electric field and the induced polarization $\mathbf{P}$ in the material:

$$\mathbf{D} = \epsilon_0 \mathbf{E} + \mathbf{P}, \tag{2.5}$$

with the electrical permittivity of the vacuum ϵ_0. In analogy to $\mathbf{D}$, the magnetic flux density $\mathbf{B}$ is made up of magnetic field $\mathbf{H}$ and the magnetization $\mathbf{M}$ in the material:

$$\mathbf{B} = \mu_0 \mathbf{H} + \mathbf{M}, \tag{2.6}$$

with μ_0, the magnetic permeability of the vacuum.

By combination of Eqs. (2.1−2.4) the inhomogeneous wave equation is constructed:

$$\nabla^2\mathbf{E} - \epsilon_0\mu_0\partial_t^2\mathbf{E} = \mu_0\partial_t^2\mathbf{P} \tag{2.7}$$

Therefore, the polarization $\mathbf{P}$ in the material is the driving force of electric fields, i.e. the emitted photons.

The polarization itself is induced by electric fields, or, in the quantum mechanical picture, by photons of frequency ω incident to the sample material. Whereas the polarization depends linearly on the field strength for small intensities, this relation becomes nonlinear for high intensities, as in the case of laser light. More specific, the relation is a power series in $\mathbf{E}^\omega$:

$$\mathbf{P}_i(t) = \epsilon_0\left[\chi_{ij}^{(1)}\mathbf{E}_j^\omega(t) + \chi_{ijk}^{(2)}\mathbf{E}_j^\omega(t)\mathbf{E}_k^\omega(t) + \chi_{ijkl}^{(3)}\mathbf{E}_j^\omega(t)\mathbf{E}_k^\omega(t)\mathbf{E}_l^\omega(t) + \dots\right]. \tag{2.8}$$

The $\chi_{ijk\dots}^{(d)}$ are susceptibility tensors of the order d. The components decrease for each order by a factor of $1.94\cdot10^{-12}\ \frac{\mathrm{m}}{\mathrm{V}}$ [2, p.3]. Indices i, j, k, l denote polarization directions of the fields and the induced polarization. The different terms in Eq. (2.8) are associated with corresponding optical effects. Linear optics is described by the lowest order term. One photon of polarization j is incident to the sample and induces a polarization along i in the medium. The higher terms describe induction of a polarization by two (three, ...) photons of polarizations j, k, l, ... Therefore, the second (third) term correspond to SHG (THG) which will be treated in more detail in Sec. 2.5. In principle, SHG is not the only effect connected to the second term. By applying plane waves for the electric fields, it becomes clear that two photons can induce a constant electric field in the sample (optical rectification). Furthermore, by choosing different frequencies for the two photons also sum- and difference-frequency generation (SFG and DFG) is possible. For SHG, Eq. (2.8) reduces to:

$$\mathbf{P}_i^{2\omega}(t) = \epsilon_0\chi_{ijk}^{(2)}\mathbf{E}_j^\omega(t)\mathbf{E}_k^\omega(t). \tag{2.9}$$

At this point, knowledge about the susceptibility tensor is necessary to link the polarizations of the incoming photons, which can be controlled in the experiment, to the induced polarization. The tensor of second rank (a $3\times3\times3$ matrix) contains 27 entries. These can often be reduced by symmetry considerations which arise from the crystal structure of the sample. To gain information about which of the entries vanish due to symmetry reasons, at least two formalisms can be applied that give the same information in the end. Note, that symmetry arguments are only necessary conditions for an entry to be allowed, not sufficient ones.

(i) Tensor formalism: Depending on the crystal symmetry and its symmetry operations, the number of tensor entries is reduced. For a cubic crystal of T_d ($\bar{4}$3m) symmetry six entries remain. These are all the permutations of χ_{xyz}. In this example, two photons of different polarizations, e.g. y and z, induce a polarization along the third independent direction, e.g. x, in the medium. Note, that all directions are defined with respect to the crystal lattice and not to the lab system. Tables of tensor components for all point groups and the derivation of those can be found in [21, 22].

(ii) Group Theory: The mathematical concept of groups and their symmetry operations is applied to photons, crystal states and perturbations to calculate possible excitations by light of certain polarizations. Therefore, symmetries will be assigned to photons, Sec. 2.2, and to crystal states, Sec. 2.3. The group theory formalism is used throughout the remainder of this thesis. It is introduced in Sec. 2.6.

Both concepts are linked by the definition of the susceptibility tensor to matrix transition elements [23] which can be calculated by group theory:

$$\chi^{(2)}_{ijk} \propto \sum_{\nu} \frac{\langle g|\mathrm{V}^{2\omega}_{k}\,|f\rangle\langle f|\,\mathrm{V}^{\omega}_{j}\,|\nu\rangle\langle\nu|\,\mathrm{V}^{\omega}_{i}\,|g\rangle}{\left(E_f - E_g - 2\hbar\omega\right)\left(E_\nu - E_g - \hbar\omega\right)}. \tag{2.10}$$

$|g\rangle$, $|\nu\rangle$ and $|f\rangle$ are the crystal ground state, virtually excited intermediate states and final state after excitation, respectively. Their energies are given by E_g, E_ν and E_f. The energy of the photons involved is the product of the reduced Planck's constant $\hbar$ and the photon frequency ω. The operators V^{ω}_{i}, V^{ω}_{j} and $\mathrm{V}^{2\omega}_{k}$ correspond to photons of polarization i, j and k, that mediate the transitions between the states. Implications of Eq. (2.10) will be discussed in detail in the following sections.

2.2 Light-matter interaction

In the last section, the susceptibility was connected to matrix transition elements, $\langle f|\,\mathrm{V}\,|g\rangle$, with the operator V that is given by the exciting photon. Deeper insight into V is gained by investigating the interaction between an electron in the crystal and the incoming light field.

Following the derivation of [24, 254 ff.], the Hamiltonian for one electron is given by:

$$H_0 = \mathbf{p}^2/2m_0 + V(\mathbf{r}), \tag{2.11}$$

with the momentum $\mathbf{p}$ and mass m_0 of a free electron. $V(\mathbf{r})$ represents an arbitrary potential. Minimal coupling connects the electron to the electro-magnetic field. In Coulomb gauge, the momentum operator $\mathbf{p}$ is extended to $p + e\mathbf{A}$. Herein, e is the elementary charge and $\mathbf{A}$ is the vector potential which depends on the magnetic field by $\mathbf{B} = \nabla \times \mathbf{A}$. The total Hamiltonian reads then:

$$H = \frac{(\mathbf{p} + e\mathbf{A})^2}{2m_0} + V(\mathbf{r}) = \frac{\mathbf{p}^2}{2m_0} + \frac{e}{m_0}\mathbf{A}\cdot\mathbf{p} + \frac{e^2A^2}{2m_0} + V(\mathbf{r}) = H_0 + H_{\mathrm{eR}} + H_{\mathrm{dia}}, \tag{2.12}$$

where the term H_{dia} is quadratic in magnetic field and describes the diamagnetic shift experienced by electrons in magnetic field. The term H_{eR} corresponds to the interaction of electron and light field. Therefore, the transition from a ground state $|g\rangle$ to a final state $\langle f|$ is given by:

$$\langle f|\,H_{\mathrm{eR}}\,|g\rangle = \frac{e}{m_0}\langle f|\,\mathbf{A}\cdot\mathbf{p}\,|g\rangle\,. \tag{2.13}$$

The operator $\mathbf{A}$ is considered a plane wave:

$$\boldsymbol{A} = A_0 \cdot \hat{e}\,\exp\left[i(\mathbf{k}\cdot\mathbf{r} - \omega t)\right], \tag{2.14}$$

with amplitude A_0, unit direction vector $\hat{e}$, wave k-vector and direction $\mathbf{r}$. Usually, the light wavelength is much larger than the crystal unit cell. Therefore, $\mathbf{k}$ is small and the spacial part of the exponential function in Eq. (2.14) can be developed in a Taylor series:

$$\exp\left[i(\mathbf{k}\cdot\mathbf{r})\right] = 1 + i(\mathbf{k}\cdot\mathbf{r}) - \frac{1}{2}(\mathbf{k}\cdot\mathbf{r})^2 + \dots . \tag{2.15}$$

The first, $\mathbf{k}$-independent term is the so-called electric dipole approximation, whereas the term linear in $\mathbf{k}$ provides the electric quadrupole and magnetic dipole contributions of the light field. In total, the electric-dipole (V_{D}) and electric-quadrupole/ magnetic-dipole ($V_{\mathrm{EQ/MD}}$) transition matrix elements have the forms:

$$\langle f|\, V_{\mathrm{D}}\, |g\rangle = \frac{e}{m_0}\langle f|\, \mathbf{p}\, |g\rangle \qquad \text{and} \qquad \langle f|\, V_{\mathrm{EQ/MD}}\, |g\rangle = \frac{e}{m_0}\langle f|\, \mathbf{k}\cdot\mathbf{p}\, |g\rangle . \tag{2.16}$$

Transitions induced by a photon in quadrupole order are expected to be less efficient by a factor of 10^{-2} compared to those by a dipole. The operators $\mathbf{p}$ and $\mathbf{k}$, as well as the ground and final state will be connected to symmetry representations in Sec. 2.6.

2.3 Excitons

In the preceding sections, transitions between unspecified crystal states were mentioned which will now be filled with life. In general, semiconductor materials exhibit a highest valence band filled completely with electrons and a lowest, completely empty, conduction band, separated by an energy band gap E_{g} of several eV, see Fig. 2.1(a). Whenever an incident photon has an energy $\hbar\omega$ larger than the band gap, an electron is excited into the conduction band leaving behind a positively charged hole in the valence band. Both oppositely charged particles are bound to each other by the Coulomb interaction and form an exciton [25, 26] with a binding energy E_{bind} of a few, up to tens of meV. Due to the binding energy, excitons are located energetically below the band gap, forming a hydrogen-like series [Fig. 2.1(b)] with energies:

$$E_{\mathrm{ex}}(n,\boldsymbol{K}) = E_{\mathrm{g}} - Ry^*\frac{1}{n^2} + \frac{(\hbar\boldsymbol{K})^2}{2M}. \tag{2.17}$$

Exciton energies levels comprise (at least) three parts. Firstly, the band gap E_{g} of the material. Secondly, the exciton binding energy which is the effective Rydberg energy Ry^* divided by the squared exciton principal number n. To get Ry^*, the hydrogen Rydberg energy is modified by the material's dielectric constant ϵ_{r}, the effective reduced mass μ of effective electron (m_{e}) and effective hole (m_{h}) mass and the exciton Bohr radius a_{B},

$$Ry^* = \frac{\hbar^2}{2\mu a_{\mathrm{B}}^2}, \quad \text{with} \quad \mu = \frac{m_{\mathrm{e}}m_{\mathrm{h}}}{m_{\mathrm{e}}+m_{\mathrm{h}}} \quad \text{and} \quad a_{\mathrm{B}} = \frac{\hbar^2\epsilon_{\mathrm{r}}}{\mu e^2}. \tag{2.18}$$

And thirdly, the centre-of-mass motion of the exciton has to be considered for the exciton energy. Therefore, $\mathbf{K}$ and M represent the sum of electron and hole wave vector and the sum of effective masses m_{e} and m_{h}.

In principle, also the absorption continuum of photons with energies larger than the band gap of a crystal can be explained by generation of dissociated exciton states.

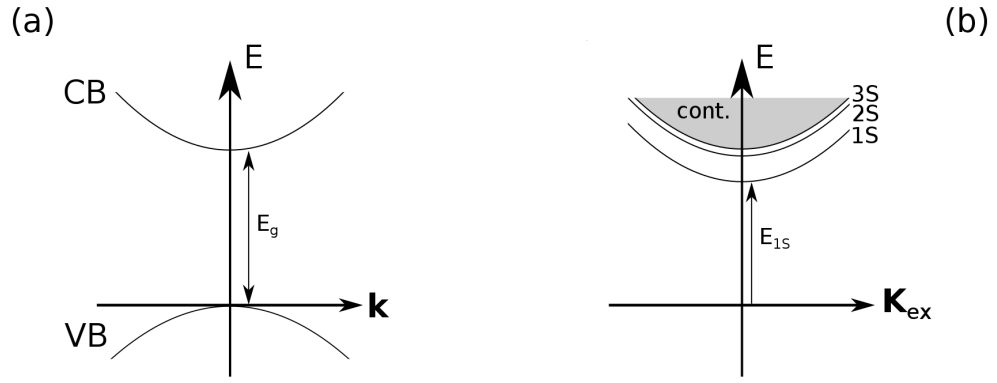

Figure 2.1: (a): Highest valence band and lowest conduction band in a semiconductor in the one-particle picture. (b): Two-particle picture of discrete and continuum exciton states.

2.4 Exciton-polaritons

In the last section, the exciton was introduced as a two-particle crystal state that is created by absorption of a photon. However, this theoretical picture of the weak coupling regime between light and matter is not complete. The electron and hole of the exciton can recombine and emit a photon which can again excite an exciton and so on. Therefore, photon and exciton can no longer be regarded as separate particles, but as new mixed eigenstates of the semiconductor system. These states are called exciton-polaritons (or short: polaritons).

Originally introduced in the 1950s [27, 28], the concept of exciton-polaritons showed to be fruitful and was extensively studied. This section is written along the lines of Ref. [29] and Ref. [30, 70 ff.]. There, also an introduction and overview of polaritons can be found.

The frequency-dependent dielectric function $\epsilon(\omega)$ is the starting point for the discussion of polaritons,

$$\epsilon(\omega)=1+\frac{f}{E^2-(\hbar\omega)^2-i\gamma\hbar^2\omega}. \tag{2.19}$$

Wherein

$$f=\frac{\hbar^2e^2}{\epsilon_0 m_0 V} \tag{2.20}$$

is the oscillator strength per volume V of an resonance with energy E_{ex} and damping γ. In the quantum mechanical definition, the oscillator strength is connected to a transition from ground to final state of energy $\hbar\omega$ by:

$$f=\frac{2}{m_0\hbar\omega}|\langle f|\,\hat{\epsilon}\cdot\mathbf{p}\,|g\rangle\,|^2. \tag{2.21}$$

The transition operator is the scalar product of polarization along $\hat{e}$ and momentum.

In the case of a transition from the crystal vacuum to an exciton state of energy E_{ex}, the oscillator strength is given by:

$$f_{\mathrm{ex}} = g_{\mathrm{s}} \frac{2|\hat{\epsilon} \cdot \mathbf{p}_{\mathrm{cv}}|^2}{m_0 \hbar \omega} \Big| \int F(r_{\mathrm{e}},r_{\mathrm{h}}) \delta(r_{\mathrm{e}} - r_{\mathrm{h}}) dr_{\mathrm{e}} dr_{\mathrm{h}} \Big|^2 \tag{2.22}$$

$$= g_{\mathrm{s}} f_0 \Big| \int F(r = 0,R) dR \Big|^2. \tag{2.23}$$

Equations (2.22) and (2.23) show the exciton oscillator strength for electron-hole and for relative and centre-of-mass coordinates, respectively. The function F is the exciton envelope-function with either set of coordinates. The prefactor g_{s} accounts for spin-orbit coupling. It can be shown that the exciton oscillator strength is inversely proportional to n^3 (whereas the binding energy behaves as: $E_{\mathrm{bind}} \propto n^{-2}$).

Another consequence of the polariton effect is the splitting of the optically active and inactive exciton spin states by Δ, as well as, a splitting of the longitudinal and transversal exciton components by ΔE_{LT}. These occur due to electron-hole exchange interaction and are shown in Fig. 2.2. The LT-splitting is proportional to the exciton oscillator strength, i.e. $\Delta E_{\mathrm{LT}} \propto f_{\mathrm{ex}}$.

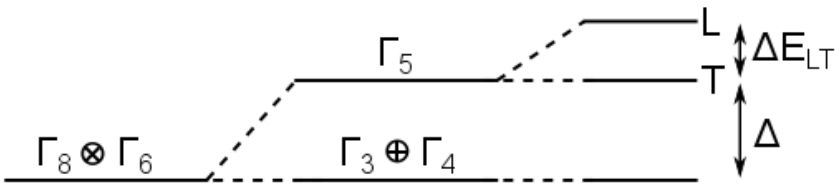

Figure 2.2: Symmetries of the 1S exciton in T_d crystal symmetry and energy splitting Δ due to analytical and ΔE_{LT} by non-analytical exchange-interaction [29].

The dielectric function, Eq. (2.19), is connected to matter by Eqs. (2.5) and (2.1):

$$\nabla \cdot \mathbf{D} = \nabla(\epsilon_0 \mathbf{E} + \mathbf{P}) = \epsilon_0(1+\chi) \nabla \cdot \mathbf{E} = \epsilon_0 \epsilon(\omega) \nabla \cdot \mathbf{E} = 0 \tag{2.24}$$

In the case of a real system, often resonances are present at higher energies than the one which is considered. Therefore, "1" in Eq. (2.24) is replaced by a background oscillator ϵ_{b} to account for these. Equation (2.24) has the solutions

$$\epsilon(\omega) = \frac{c^2 \mathbf{k}^2}{\omega^2} \quad \Leftrightarrow \quad \mathbf{k}^2 = \frac{\omega^2}{c^2 \tilde{n}^2(\omega)} \quad \text{and} \quad \epsilon(\omega) = 0. \tag{2.25}$$

With the light k-vector $\mathbf{k}$ and c, the speed of light. The first equality emphasizes the link between the dielectric function and the (complex) index of refraction, $\tilde{n}$. By comparison of the expressions for the dielectric function in Eqs. (2.19) and (2.25) the exciton-polariton equation,

$$\frac{c^2 k^2}{\omega^2} = \epsilon(\omega) = \epsilon_{\mathrm{b}} + \frac{f}{E_{\mathrm{ex}}^2 - (\hbar\omega)^2 - i\gamma\hbar^2\omega}, \tag{2.26}$$

is obtained. This implicit form of the polariton-dispersion can be transformed into an explicit form, $\omega(\mathrm{k})$, or $E(k)$.

In Fig. 2.3, an example of a polariton-dispersion is plotted. The uncoupled dispersions of exciton and photon (dashed lines) cross each other. The photon dispersion is simply $E = \hbar ck/n$, whereas the exciton-dispersion is given by Eq. (2.17). In the strong

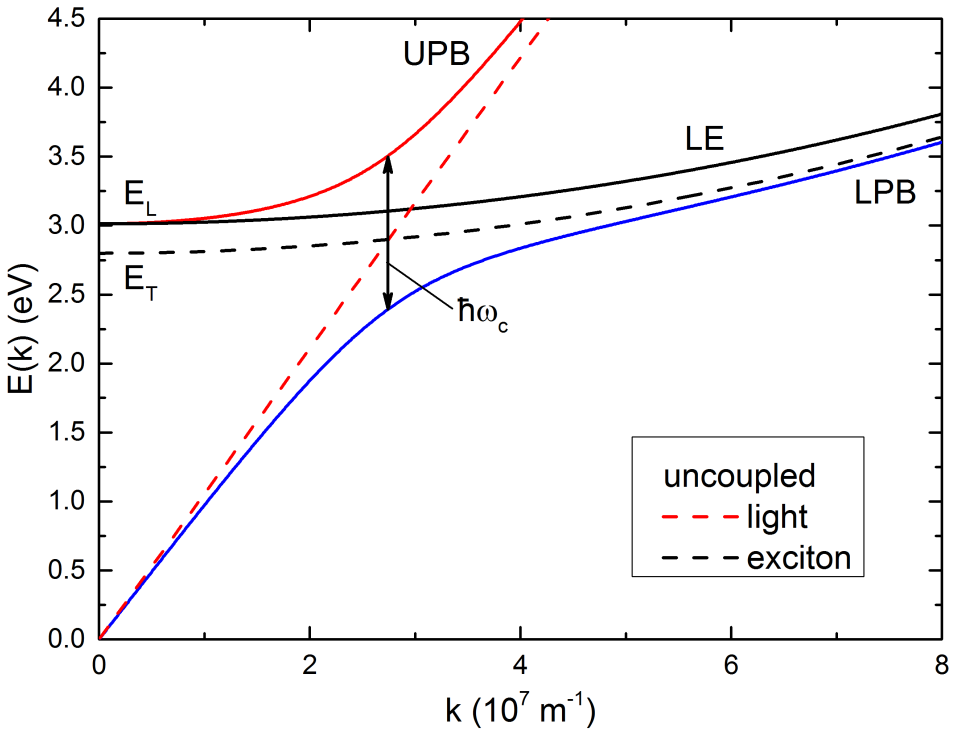

Figure 2.3: Exemplary exciton-polariton dispersion from Eq. (2.26). Shown are the upper (UPB, solid red line) and lower polariton-branch (LPB, solid blue line) and the longitudinal exciton (LE, solid black line). The uncoupled light and exciton dispersion are indicated by red and black dashed lines, respectively. The arrow indicates the Rabi-energy.

coupling regime, depending on the crystal structure, light direction and polarization, the dispersion is split into an upper and lower polariton branch (UPB and LPB) and a longitudinal one (LE). As shown in Fig. 2.3, UPB and LE coincidence in energy at $\mathbf{k} = 0$ and are shifted to higher energy E_L with respect to the $\mathbf{k} = 0$ value of the LPB, E_T, by the LT-splitting. For increasing $\mathbf{k}$, the spatial dispersion of the exciton is notable. For energies close to the original exciton resonance, the branches are called exciton like and far off-resonant photon like. The splitting of the branches at the point of the same incline is called the rabi-energy, $\hbar\omega_\mathrm{c} \propto \sqrt{f}$, which describes the point where the polariton is half exciton, half photon like.

The same result is obtained by a quantum mechanical approach. The exciton of

energy E_{ex}, see Eq. (2.17), and photon of energy E_γ are coupled with the strength $1/2\hbar\Omega_{\mathrm{R}}$. Mathematically, this coupling can be described in matrix form, in the same way as the coupling of two oscillators. The corresponding Hamiltonian H_{pol} is

$$H_{\mathrm{pol}} = \begin{pmatrix} E_{\mathrm{ex}} & \frac{1}{2}\hbar\Omega_{\mathrm{R}} \\ \frac{1}{2}\hbar\Omega_{\mathrm{R}} & E_\gamma \end{pmatrix}. \tag{2.27}$$

Diagonalization of H_{pol} reveals again the upper and lower polariton branch:

$$E_{\mathrm{U/L}} = \frac{E_{\mathrm{ex}} + E_\gamma}{2} \pm \sqrt{\left(\frac{E_{\mathrm{ex}} + E_\gamma}{2}\right)^2 + \left(\frac{\hbar\Omega_{\mathrm{R}}}{2}\right)^2}, \tag{2.28}$$

as shown in Fig. 2.3.

2.5 Second and third harmonic generation

The process of SHG was already mentioned in Sec. 2.1 and will be explained in more detail here. It is noteworthy that SHG and THG are coherent processes. Therefore, the full energy and k-vector of the incoming photons is transferred to the exciton which in turn emits one photon of the same energy and momentum. In contrast, during a photoluminescence measurement, excited electrons and holes scatter prior to emission and change thereby energy and momentum. An advantage of SHG and THG at exciton resonances is that the crystal is almost transparent for the fundamental incoming light. Due to low absorption, light can penetrate through the whole crystal probing its properties far below the surface. On the other hand, SHG and THG might arise only from a thin layer of the crystal, because of different indices of refraction for fundamental and second or third harmonic light. Therefore, harmonic light from the first part of a crystal interferes destructively with harmonic light from deeper layers.

In order to excite a crystal state, e.g. an exciton, two photons of half the transition energy are necessary at the same time and place. The excitation, however, is still a two step process [Eq. (2.10)] where the first photon induces a virtual transition to an intermediate state $|\nu\rangle$. The second photon excites the final state resonantly. This intermediate state can originate from a higher conduction band, a lower valence band, or another exciton state of the same band and has to be one-photon allowed. Due to the large energy-offset between photon and state, a (virtual) transition to it is allowed for short time only. The transition element is accordingly small as the denominator is large, see Eq. (2.10).

In Fig. 2.4(a–c), the classical description of SHG and THG by the susceptibility tensor as a material parameter and the quantum mechanical picture with the two-(three-)step excitation and one photon emission are summarized.

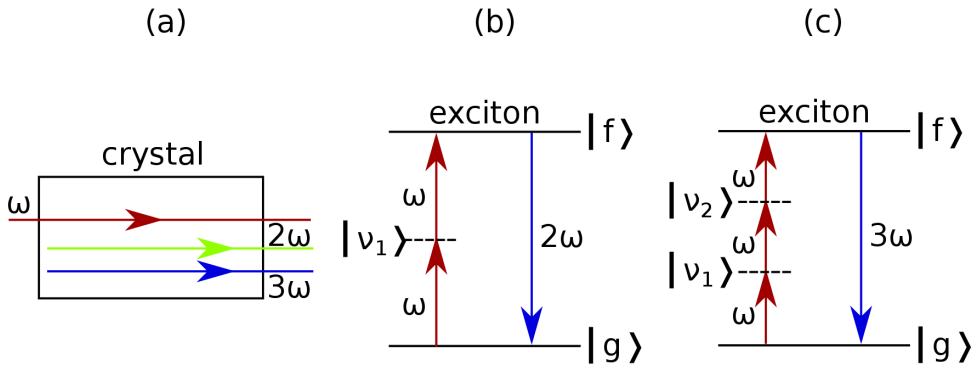

Figure 2.4: SHG and THG in the classical (a) and quantum mechanical description (b) and (c). The frequencies of the fundamental and generated photons are denoted by ω, 2ω and 3ω, respectively. $|g\rangle$, $|\nu_1\rangle$, $|\nu_2\rangle$ and $|f\rangle$ are the empty crystal ground state, virtually excited intermediate states and final exciton state.

2.6 Group theory

The formalism of group theory is a powerful tool to exploit symmetry properties of photons, excitons and perturbations in order to predict and analyse state transitions. In this section, the fundamental idea of symmetry calculations is presented. It will be extended step by step throughout the following chapters, whenever results are analyzed. Group theory at different levels is the topic of several textbooks, see Refs. [24, 30–32].

The first step, to be able to apply group theory to a crystal system, is to determine its point group. That is, the set of symmetry operations (rotations, reflexions, etc.) under which the crystal structure is invariant. The groups are characterised in Schoenflies (Hermann-Mauguin) notation. Most common are cubic structures with groups O_h ($m\bar{3}m$), T_d ($\bar{4}3m$) and hexagonal crystals denoted by C_{6v} (6mm), but many other exist. Once the group is identified, its members, the irreducible representations, denoted by Γ_i's, are said to transform as basis functions. These, in turn, are associated with the functions of photons, excitons and perturbations.

In Sec. 2.2, the dipole and quadrupole operators and the corresponding transition matrix elements of a photon were derived. The dipole operator $\mathbf{p}$, for instance, transforms like a three dimensional vector in x, y and z direction. These basis functions are represented by Γ_4^- in point group O_h, and Γ_5 in T_d [33]. The next higher order operator $V_{\mathrm{EQ/MD}}$, see Eq. (2.16), is the tensor product of the three-dimensional wave vectors $\mathbf{k}$ and $\mathbf{p}$. In both point groups, O_h and T_d, these functions are represented by $\Gamma_1^{(+)} \oplus \Gamma_3^{(+)} \oplus \Gamma_4^{(+)} \oplus \Gamma_5^{(+)}$.

The symmetries of excitons comprise the function of the hole in the valence band, the electron in the conduction band and the envelope function,

$$\Gamma_{\mathrm{exc}} = \Gamma_{\mathrm{VB}} \otimes \Gamma_{\mathrm{CB}} \otimes \Gamma_{\mathrm{env}}. \tag{2.29}$$

Whereas the functions for electron and hole are derived from the atomic orbitals which form the bands, the envelope function depends on the relative movement of electron and hole. An S-exciton has Γ_1 symmetry in all point groups, as it is a sphere and therefore, the neutral element of the groups.

To decide whether a transition is potentially allowed for one- or two-photon excitation in dipole, or quadrupole order, the tensor product of initial and final state and the photon operator have to be considered. Note, that a symmetry allowed transition can still be forbidden, e.g. due to spin restrictions, or be very weak due to low oscillator strength. From symmetry reasons, a transition is one-photon dipole allowed if the tensor product of ground state and photon operator equals the final state. Or, likewise, the matrix element does not vanish,

$$\langle f | V_\mathrm{D} | g \rangle = \left\langle \Gamma_\mathrm{exc} \middle| \Gamma_\mathrm{pho} \otimes \Gamma_1 \right\rangle \neq 0. \tag{2.30}$$

The same procedure holds for a two-photon dipole transition,

$$\langle f | V_\mathrm{D} V_\mathrm{D} | g \rangle = \left\langle \Gamma_\mathrm{exc} \middle| \Gamma_\mathrm{pho} \otimes \Gamma_\mathrm{pho} \otimes \Gamma_1 \right\rangle \neq 0. \tag{2.31}$$

To evaluate the tensor products and, as previously done, assign representations to symmetries the tables of Koster *et al.* [33] are most valuable.

If a state f_2 is only excitable by two photons and a state f_1 only one-photon allowed, no SHG is observed. However, it might be induced by application of an external perturbation, e.g. a magnetic field. Thus, f_1 and f_2 become mixed by the field and can contribute to the SHG process [Fig. 2.5]. Note, that the effect of the magnetic field is not to change the excitation, but to admix a one-photon allowed state to the original final state.

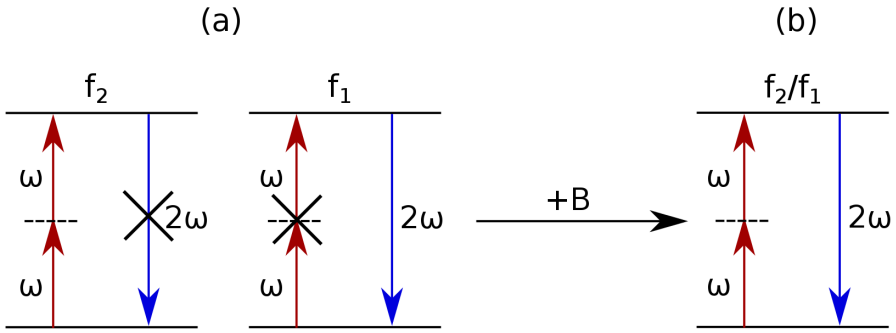

Figure 2.5: Mixing of states f_2 and f_1 in the case of an applied magnetic field. (a) Each state is two-, or one-photon allowed only. (b) Mixed state f_2/f_1 is two- and one-photon allowed and contributes to SHG.

Parts of these calculations are performed during the upcoming chapters. A thorough elaboration is given in the Appendix B.

3 Experimental Setup

In this chapter, the LC-Setup (named after the companies name: Light Conversion) with its multiple possibilities is introduced. The laser system, polarizing optics, monochromator and camera are connected to a personnel computer and operated electronically. Different measurement techniques and their protocols are elucidated. Known issues and occurring problems of the laser system and during measurements are treated in the Appendix A.

In Fig. 3.1, the components of the setup are shown. The Pharos pump-laser provides the fundamental light for the femto- and picosecond optical parametric amplifier (OPA) by which the wavelength of the light can be tuned in the ranges given. Therefore, SHG femtosecond measurements are possible in the emission range of $315-1300$ nm, THG in the range $210-860$ nm. Picosecond measurements are feasible at shorter wavelengths in the emission range. SHG in principle down to 160 nm and THG down to 105 nm. Main optics of the setup are polarizer (GT1: Glan Thompson linear polarizer and a half-wave plate) and analyzer (half-wave plate and GT2) to set the light polarization, as well as lenses to focus the light to the sample and into the monochromator. In the magnet cryostat, the sample can be cooled down to superfluid helium temperature and magnetcic fields of up to 10 T are applied. Two detection channels of different resolution are available. Each of these consists of a monochromator (MC) and charge coupled device (CCD) camera. A close-up of the polarizer/analyzer section with direction and angle definitions is given in Fig. 3.2.

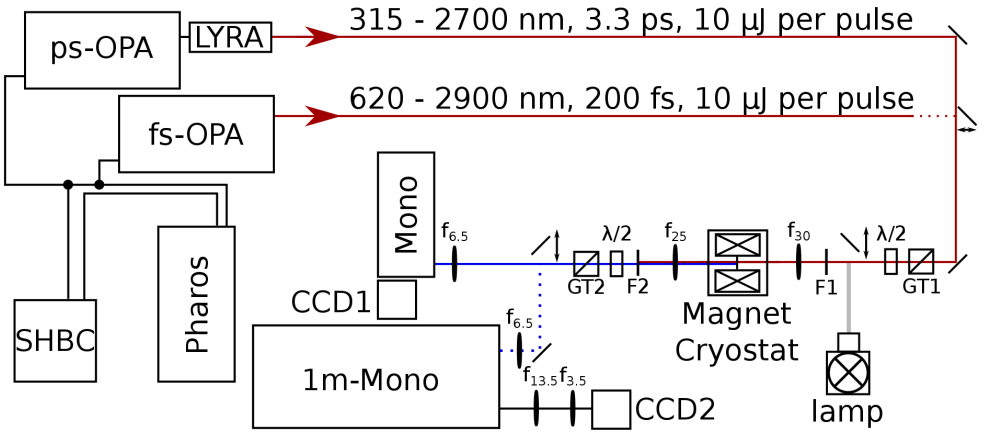

Figure 3.1: Layout of the current LC-Setup. The parts are: CCD, charge coupled device camera; F, colour filter; f_{xy}, lense with xy-cm focal length; GT, Glan Thompson linear polarizer; $\lambda/2$, half-wave plate; LYRA, harmonic generator; Mono, monochromator; OPA, optical parametric amplifier; Pharos, pump laser; SHBC, Second Harmonic Bandwidth Compressor.

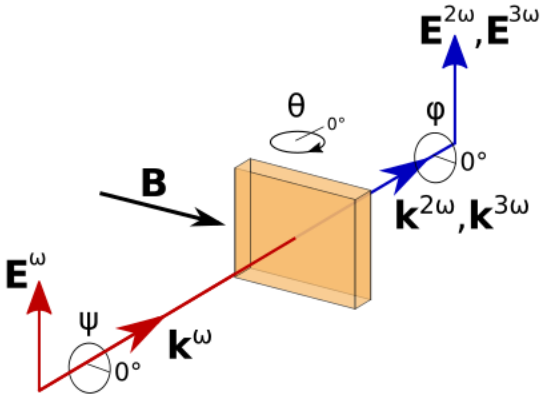

Figure 3.2: Close-up of the polarizer/analyzer section. The polarization angle of the incoming fundamental light $\mathbf{E}^{\omega}$ is ψ with respect to the horizontal axis. Its $\mathbf{k}^{\omega}$-vector is parallel to $\mathbf{k}^{2\omega}$ ($\mathbf{k}^{3\omega}$) of the outgoing light $\mathbf{E}^{2\omega}$ ($\mathbf{E}^{3\omega}$). The analyzer angle with respect to the horizontal axis is φ.

3.1 Laser system

A detailed description of the laser system is given in the manuals. Here, the basic properties and concepts are summarized. The layout of the system is shown in Fig. 3.3.

3.1.1 Pharos pump laser

The pump laser (PUMP1) contains an oscillator with an ytterbium-doped potassium gadolinium tungstate (Yb:KGW) crystal as active medium pumped by arrays of laser diodes. Femtosecond pulses are induced by Kerr-lense modelocking. Radiation of the oscillator is amplified in the regenerative amplifier (RA) by chirped pulse amplification [34]. Therefore, the pulses are stretched and injected into the RA that is pumped by continuous wave laser diodes. Following the RA, a part of the radiation is compressed, while the other part is emitted without compression. By leaving the laser, the pulse repetition rate can be controlled by a pockels cell (pulse picker) between 1 Hz and 30 kHz. Emitted pulses have a duration of 290 fs and wavelength of 1030 nm. Average power is 9.0 W for the uncompressed and 3.6 W for the compressed beam.

3.1.2 Second-harmonic bandwidth compressor

The second harmonic bandwidth compressor (SHBC) is driven by the uncompressed pump laser output. In this unit, picosecond laser radiation of 515 nm with minimal spectral width is generated. Therefore, the input beam is split and the parts are chirped inversely to each other. They are overlapped in time and space in a nonlinear crystal to achieve short and spectrally narrow pulses.

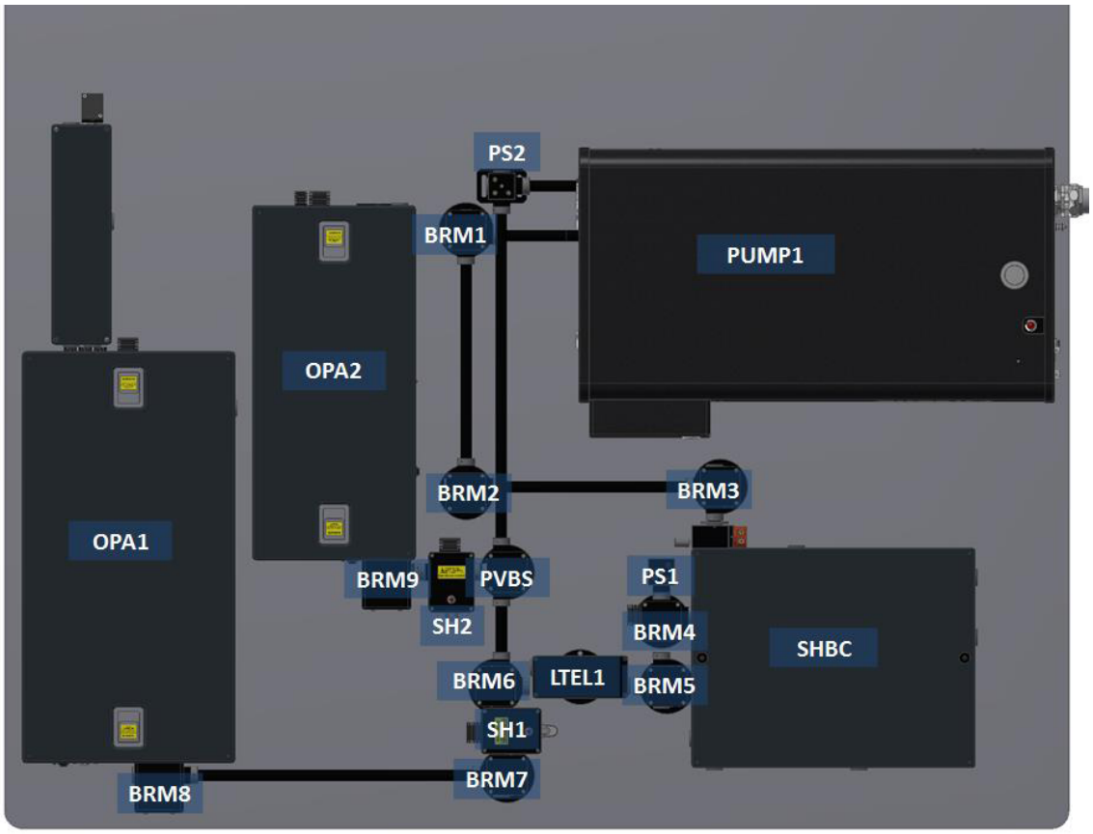

Figure 3.3: Laser system layout of main components: Pharos pump laser (PUMP1), Second-harmonic bandwidth compressor (SHBC), fs-OPA (OPA2) and ps-OPA (OPA1).

3.1.3 Orpheus femtosecond OPA

The femtosecond OPA is pumped by the compressed pump laser output. The purpose of this unit is to generate laser pulses of 200 fs duration in the wavelength range of $630 - 2600$ nm. Maximum average emission power is 500 mW with a pulse power of 16 μJ, see Fig. 3.5(b). Inside the OPA, this beam is split into two. One beam is routed to a sapphire crystal to produce a white light continuum. The other beam is converted into its second harmonic by a nonlinear crystal. Both beams are overlapped in a nonlinear crystal three times. The tilting angle of the crystal determines the phase matching condition in the crystal and therefore the wavelengths of the generated signal and idler photons. In the first step, both beams pass collinearly the nonlinear crystal by which certain wavelengths of the white light continuum are amplified. This spectrum is dispersed by a grating and passes again the crystal to amplify an even smaller bandwidth. In the third transition through the crystal, the light is amplified once more. Finally, light of two wavelengths is emitted by the OPA. Care should be taken that the emission from the OPA might differ from the programme input by several nm.

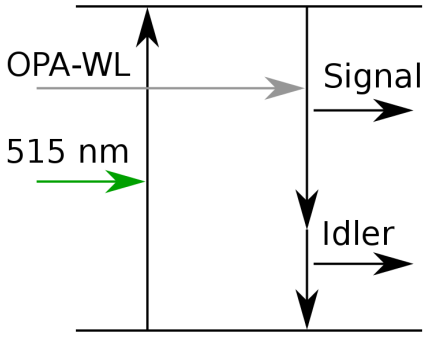

Figure 3.4: Scheme of optical parametric amplification. After the system is excited by a photon of 515 nm, emission is stimulated by photons of the white light continuum. Exact wavelengths of signal and idler beam are determined by phase matching conditions in the medium.

3.1.4 Orpheus picosecond OPA and Lyra

The picosecond OPA works in a similar way as the previously described femtosecond OPA. The difference is that here both, the compressed pump laser output for white light generation and the output from the SHBC are injected. Therefore, no 515 nm generation is necessary here. After the three amplification stages, laser pulses of 3.3 ps duration and wavelength of 630 – 1030 nm (signal) and 1031 – 2600 nm (idler) are emitted. Maximum average power is 700 mW, corresponding to 23 μJ per pulse, see Fig. 3.5(a). A broader wavelength range is feasible by the LYRA following the output of the OPA. It applies an additional nonlinear crystal to the beam path allowing for generation of wavelengths as short as 315 nm. Care should be taken that the emission from the OPA might differ ($\leqslant$ 1 nm) from the programme input.

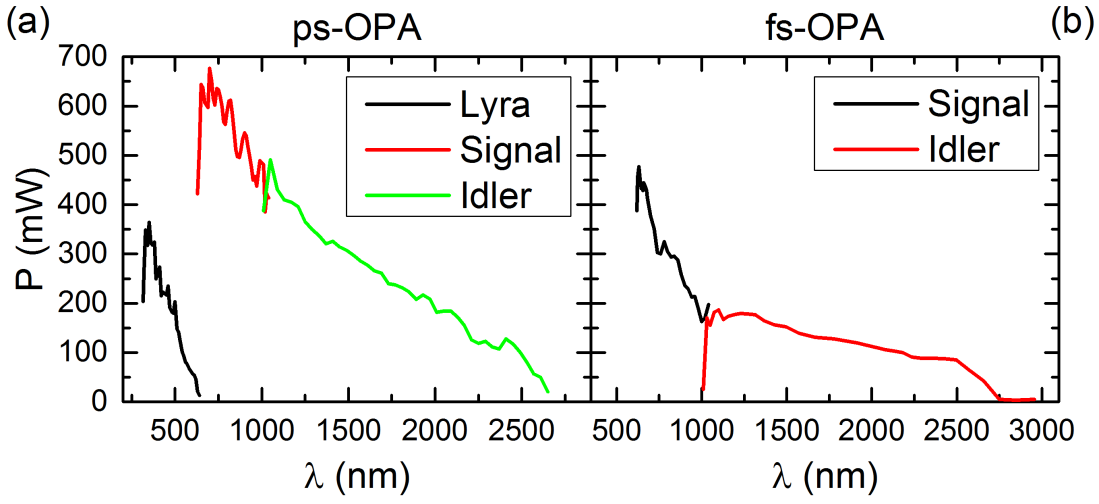

Figure 3.5: Spectral dependencies of (a) ps-OPA and (b) fs-OPA output power.

3.2 Cryostat

The samples in all experiments are installed in a helium bath cryostat (Oxford superconducting split coil cryostat) for cooling and application of magnetic fields. The temperature in the sample chamber (VTI: Variable Temperature Inset) can be set to $4.2 - 300$ K. Cooling is achieved by liquid helium from a 20 l reservoir. To reduce helium losses from the reservoir by evaporation, it is surrounded by a vacuum (10^{-6} mbar) chamber followed by a liquid nitrogen shield and a second vacuum volume. By reducing the pressure in the VTI, the helium becomes superfluid and decreases the sample temperature further to about 1.4 K. Magnetic fields of up to 10 T are achieved by a pair of superconducting coils of Nb-Ti in a copper matrix. They are located in the lower part of the cryostat, next to the samples, inside the liquid helium reservoir to provide superconductivity. Four windows at sample height allow to shine laser light parallel or perpendicular to the magnetic field to the sample.

3.3 Monochromator

The purpose of the (Czerny-Turner-) monochromator is to disperse the signal light spatially. Therefore, the light is focussed to the entrance slit of the monochromator, whereupon it is sent to a concave mirror. This reflects a parallel beam to the grating. Here, depending on the tilting angle of the grating, a particular wavelength range of the spectrum is reflected in first order to a second focussing mirror which directs the light to the exit slit.

Important specifications of a monochromator are its focal length and the grating properties: width and grooves per mm. A compromise has to be found between resolution and signal intensity. In general: the better the signal is resolved, the lower the signal intensity becomes because it is spread over a larger spatial range. To optimize the configuration, it is necessary to illuminate the complete grating, that is, the signal beam diameter fits the grating width and height. If the light spot at the grating is too small, not all grooves are used and the resolution decreases. If the light spot is larger than the grating, light intensity is lost. Setting the correct spot size is possible by knowing the beam diameter s in front of the monochromator, its focal length f_m and the grating width g. The correct focal length f_l of the lense in front of the monochromator is thus given by:

$$f_\mathrm{l} = \frac{s}{g} \cdot f_\mathrm{m} \tag{3.1}$$

The resolution r of a monochromator at a certain wavelength λ is defined by:

$$r = g \cdot gr \cdot n = \frac{\lambda}{\Delta\lambda}, \tag{3.2}$$

with gr: groves per mm and n: order of diffraction. In Table 3.1, the parameters for both monochromators used in the experiments are summarized. The experimental resolution is determined for the combinations of Acton and camera CCD1, as well as,

Table 3.1: Parameters of monochromators: f_l, focal length; r, resolution in theory and experiment.

name	f_l (mm)	Grating (gr/mm)	r_{theo}	r_{theo} (μeV)	r_{exp}	r_{exp} (μeV)
Acton	500	1800	90000	20	18000	100
Spex	1000	1200	120000	10	40000	30

Spex and camera CCD2. See the next section for specifications of the cameras. The total resolution of the setup with installed Spex monochromator would be considerably restricted by the CCD camera. Therefore, the output beam diameter is enlarged by a factor of four by a telescope in between exit slit and camera. Thus, different wavelengths are spread further spatially and can be distinguished by the camera pixels. The overall resolution of a monochromator depends on the entrance-slit opening, too. A linear dependence was found for the Acton monochromator, starting at 20 μm opening,

$$\text{FWHM}=49\ \mu\text{eV} + 2.4\ \frac{\mu\text{eV}}{\mu\text{m}} \cdot \text{slit}(\mu\text{m}). \tag{3.3}$$

When the monochromator needs to be calibrated, e.g. a new material with a different energy range of interest than before is applied, care has to be taken whether the wavelengths of spectral lamps are given in vacuum or air. Tables for most of the common spectral lamp elements are available at the website of NIST [35]. It is most convenient to use wavelengths in vacuum for calibration. Then, energy is calculated by:

$$E = 1239.842\ \text{nm eV}/\lambda_{\text{vac}}. \tag{3.4}$$

Otherwise, when the monochromator is calibrated to wavelengths in air, the refractive index of air, $n_{\text{air}} = 1.000292$ which is slightly dependent on wavelength, pressure, temperature, etc. [36], has to be considered:

$$E = 1239.842\ \text{nm eV}/\left(n_{\text{air}}\lambda_{\text{air}}\right) = 1239.480\ \text{nm eV}/\lambda_{\text{air}}. \tag{3.5}$$

3.4 CCD camera

The CCD camera is installed at the exit slit of the monochromator. The chip is cooled by liquid nitrogen to a temperature of 150 K to reduce noise. Average readout noise values are about 140 counts per pixel column. The quantum efficiency of the CCD chip at 25°C is plotted in Fig. 3.6. Two different cameras are used with the monochromators introduced in the last chapter. CCD1 provides a 1340 × 400 pixel array with pixel size of 20 × 20 μm installed directly to the Acton monochromator. The Spex monochromator is combined with CCD2 of 2048 × 512 pixels of 13.5 × 13.5 μm size. Between monochromator and camera a telescope is set up to increase the separation between the dispersed wavelength which could otherwise not be resolved by the CCD due to too large pixel size.

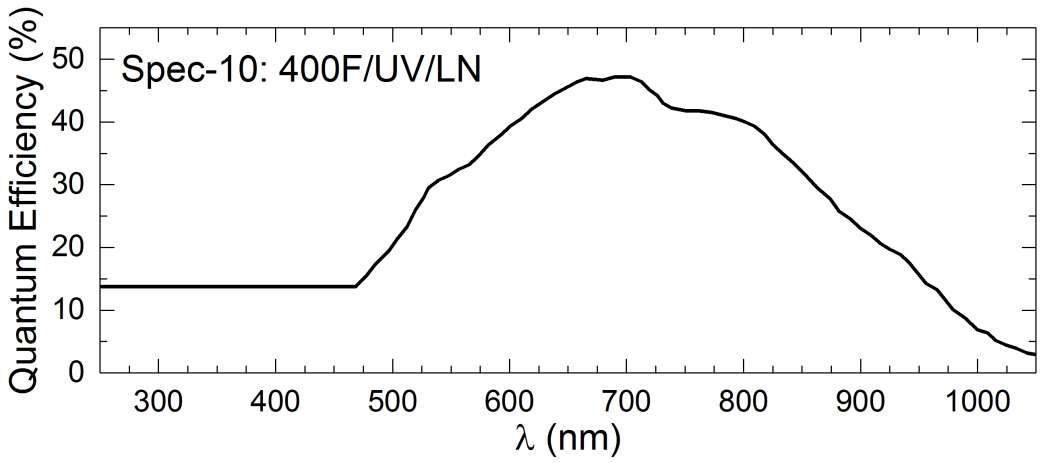

Figure 3.6: Wavelength dependent quantum efficiency of the CCD camera [37].

3.5 Other components

The remaining parts of the setup, such as polarization optics, colour filters and lenses are discussed in this section.

The linear polarization of the laser light is set by the combination of a Glan-Thompson polarizer and a half-wave plate in front of the cryostat. It is named polarizer. To select a polarization from the signal, its light passes a second set of half-wave plate and Glan-Thompson polarizer, the analyzer. By turning the plate, one linear polarization is chosen which can pass the prism whereas all other polarizations are blocked. Thus, any combination of polarizations of $\mathbf{E}^{\omega}$ and $\mathbf{E}^{2\omega}$ can be measured. Usually, the SHG signal is detected for either parallel ($\mathbf{E}^{\omega} \parallel \mathbf{E}^{2\omega}$) or crossed ($\mathbf{E}^{\omega} \perp \mathbf{E}^{2\omega}$) linear polarizations of the laser and the SHG.

Colour filters, or long/short pass filters are necessary to get reliable signals. One filter is placed between the polarizer and cryostat to suppress harmonics of the laser light and other short wavelength light generated in the polarizing optics. The laser itself is a source of multiple wavelengths, such as its pump wavelength (515 nm) and several combinations of signal and idler energies that need to be blocked. Care has to be taken in choosing a colour filter that does not produce light by photoluminescence itself. A second filter is located between cryostat and analyzer. Its task is to block the fundamental laser light. This light might damage the CCD chip and could induce again undesired wavelengths in the polarizing optics. In Table 3.2, filters used for measurements in this thesis are given.

Lenses are used on both sides of the cryostat to focus the laser light to the sample and parallelize it again. Focal length for focussing is 25 cm and 30 cm for parallelization. The laser spot size at the sample is estimated to be 100 μm in diameter.

Table 3.2: List of colour filters used in experiments. Filters before (front) and after (behind) light passes the sample. "pass" gives the range where the filter transmits light and "block" the range for absorption.

material	front	pass (nm)	block (nm)	behind	pass (nm)	block (nm)
Cu_2O, ZnSe	RG 715	715 – 1500	200 – 620	BG 39	350 – 580	680 – 1500
ZnO	RG 601	610 – 1500	200 – 580	yϕC1 UG 1	250 – 390 300 – 390	450 – 650 430 – 670

3.6 Measurement types

At the LC-setup, several different measurement techniques can be carried out in order to obtain linear and nonlinear spectra of the samples. This section focusses on the procedures, physics and (dis-)advantages of the different measurement types used.

3.6.1 Harmonic generation

The main measurement technique for exciton spectroscopy used in this thesis is second (third) harmonic generation. For that purpose, the laser photon energy is set to one half (third) of the expected exciton energy. By scanning the laser photon energy and accordingly adjusting the monochromator to double (triple) energy, a spectrum is measured. Exciton states show up as increased signal intensity at their specific energies. Properties of exciton states can be investigated by either recording spectra at different applied magnetic (electric) fields, temperatures, or by measuring rotational diagrams. Such a diagram, called an anisotropy, reveals information about the exciton symmetry, as well as mixing mechanisms.

An anisotropy is measured by fixing the excitation energy and monochromator position at an exciton resonance. Signal intensity is detected for a set of polarizations of ingoing and outgoing photons. Two measurement protocols are especially used. Firstly, polarizer and analyzer are turned parallel to each other in steps of 5° from 0° to 360° (in principle a maximum angle of 180° is sufficient, but a full rotation gives higher reliability). Secondly, the polarizer starts at 0° while the analyzer is set to 90°. With this constant offset, both are turned again till the polarizer reaches 360°.

Harmonic generation is a coherent process, as described in Sec. 2.5 in the theory. This implies that there is no relaxation present between excitation of a state by two (three) photons and emission of one photon.

An advantage of harmonic generation is that the sample is transparent to the exciting wavelength at half (one third of) the band gap energy. Thus, harmonic generation is, in principle, possible along the whole beam path inside the crystal. Still, signal generated in the first place might be reabsorbed in deeper crystal layers. Therefore, the signal represents only harmonics from the last few layers of the crystal. Favourable of nonlinear optics is increased information from measurements. Each state that is observ-

able is expected to be two-(three-) photon and one-photon allowed. All in all, harmonic generation is very sensitive to symmetries and their breaking [38]. The compensation for this information are processes of rather low intensity as compared to linear optics. The susceptibility tensors components decrease by a factor of $1.94 \cdot 10^{-12}$ $\frac{\mathrm{m}}{\mathrm{V}}$ for every order [2, p. 3].

3.6.2 White light absorption

A white light absorption experiment is performed by replacing the laser system with a broad band light source (e.g. a light bulb). Its light passes the sample and is sent into the monochromator which is set to the energy range under inspection. A crystal state which is one-photon allowed absorbs light and corresponds therefore to a dip in the spectrum. The incoherent white light can be polarized by appropriate optics, e.g. to measure circular absorption in applied magnetic field.

Despite the simple implementation of the experiment, linear absorption is not always suited to obtain information about one-photon transitions. If the absorption of a resonance is too high, or the sample too thick, absorption dips might saturate in the spectrum and no reliable linewidth can be deduced. The other way around, resonances of low oscillator strength are better observable in thicker samples.

Closely connected to absorption/transmission is (white light) reflection. Mathematically, one is calculated from the other by use of the Kramers-Kronig relations. Reflection measurements also deliver one-photon information for thick samples. Nevertheless, they are sensitive to surface properties.

3.6.3 Photoluminescence

Photoluminescence (PL) measurements reveal one-photon information of low lying resonances. Electrons are excited by a laser to energies higher than the material's band gap, called hot electrons. These electrons lose energy by relaxation processes and eventually recombine from energetically low states. Therefore, neither the **k**-vector, nor the energy of the exciting photons are preserved in photoluminescence. As already stated, only low energy states are visible in PL in general. Thus, the 1S exciton might be seen, or lower lying exciton states bound to impurities.

3.6.4 Two-photon absorption

A two-photon absorption (TPA) experiment resembles white light, or one-photon absorption. The difference is that states are excited by two photons. Thus, states of contrary selection rules to one-photon experiments can be probed. However, a laser system of very stable output power and a sensitive detection are needed to detect the small loss of laser power by absorption in the sample.

3.6.5 Photoluminescence excitation

Photoluminescence excitation (PLE) delivers information on excitation processes of states. They are easier to perform than absorption measurements as no small power deviation has to be detected. A prerequisite for this measurement type is a PL line energetically below the (exciton) states under investigation, to which the excited state can relax and eventually emit. The monochromator is set to the PL line and the laser photon energy is scanned in the range of the states of interest. Whenever an electron is excited by the laser photons into some state, it relaxes by scattering. Finally, the electron recombines at the state responsible for the PL line. Thus, a maximum in PL intensity indicates that there is a state at the energy of one, two, or three laser photons, depending on excitation wavelength. Information on symmetries of a state are obtained by fixing the laser photon energy and turning the polarization of the incoming light.

3.6.6 Two-beam measurements

Instead of using two or three photons of the same laser beam, an experiment with more than one laser source is conceivable. In that case, the light **k**-direction of each of the involved photons, e.g. in SHG, can be chosen independently. Also their energies and polarizations can be set separately inducing more degrees of freedom.

Two beams of different wavelength with the sum energy of an exciton resonance could be tuned to investigate the influence of the intermediate state(s) in the SHG (THG) process. Furthermore, the beams might not be collinear. The relative angle between them can be changed, e.g. their **k**-vectors are set independently, allowing for k-space spectroscopy [39].

By introducing a time delay for one of the beams, SHG pump-probe experiments, such as two-photon excitation stimulated-emission, are feasible to obtain lifetimes of the excitations [40].

4 Spectroscopic Techniques

In this chapter, a new method of optical nonlinear spectroscopy with spectrally broad femtosecond laser pulses is presented. The previously used method of scanning the wavelength of nanosecond laser pulses is described as well. Advantages and drawbacks of both types of measurement protocols are elaborated and compared. An introduction to femtosecond pulse lasers and an overview of applications can be found in textbooks [41, 42].

To observe optical nonlinear effects, intense light fields are necessary. Therefore, appropriate lasers need to be pulsed, in order to reach high enough field intensities of the order of GW/cm^2 for short times.

Two fundamental properties of laser pulses are their duration Δt and spectral width $\Delta\nu$. They correlate with each other by Fourier transformation, i.e. the longer the pulse, the narrower its spectrum and vice versa. This behaviour is described by [41, S. 31]

$$\Delta t \cdot \Delta\nu \geqslant \frac{1}{2}, \tag{4.1}$$

and can be transformed into

$$\Delta E \geqslant 2.063 \text{ eV} \cdot \frac{1}{\Delta t} \cdot 10^{-15} \text{ s}. \tag{4.2}$$

Note, that equality in Eqs. (4.1 and 4.2) is only valid for Gaussian-shaped pulses. Real pulses might show either longer duration or broader spectrum. A good approximation to Eq. (4.2) is that a pulse duration of 1 fs corresponds to a spectral width of 2 eV.

The emission spectra of the picosecond and femtosecond OPAs at 1.551 eV (800 nm) are detected directly by the CCD chip and are shown as black curves in Fig. 4.1(a) and (b). In order to get an impression of the excited spectral range in an SHG experiment, the fundamental energy is doubled by a beta barium borate (BBO) crystal, shown by the red lines in Fig. 4.1. Comparison of the full width at half maximum (FWHM) of the harmonic signals to the fundamental spectra reveals that the second harmonic spectra are broader than the fundamental linewidth. The factors are 1.9 for the ps-pulses and 1.2 for fs-pulses. Theoretically, the change in width of the fundamental spectrum to the second harmonic one can be calculated. Firstly, the photons add up in energy which gives twice the energy spread in second harmonic. Secondly, the intensity squares, giving a $\sqrt{2}$ reduced FWHM for Gaussian-shaped pulses. The product of both effects results in a $\sqrt{2}$ broader second harmonic spectrum.

The intensity I of a laser pulse is calculated by

$$I = P_\mathrm{m}/(F \cdot \tau \cdot f), \tag{4.3}$$

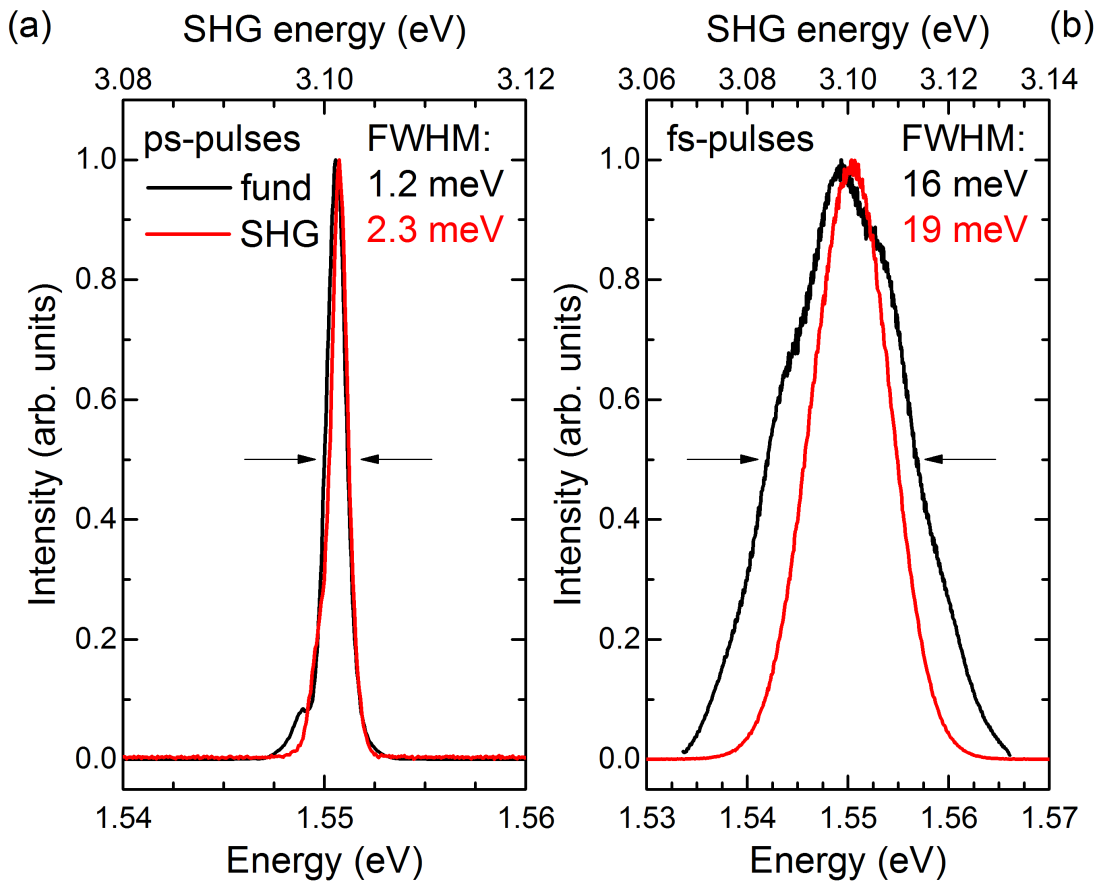

Figure 4.1: Fundamental pulse spectrum of (a) the ps-OPA and (b) the fs-OPA at 1.55 eV (800 nm), black lines. These are compared to the second harmonic spectrum by a BBO crystal, red lines. The fundamental spectra correspond to the lower energy axis and the SHG signal to the upper one.

where P_{m} is the average power of the laser beam, measured by a powermeter in Watts, F is the focus area which is estimated to have 100 μm in diameter. τ fs is the FWHM pulse duration and f=30 kHz the repetition rate of the laser pulses. This amounts for the fs-OPA (τ=140 fs), for the ps-OPA (τ = 3.3 ps) and for the previous used ns-laser system (τ=7 ns and f=10 Hz) to intensities per pulse:

$$I_{\mathrm{fs}}{=}20\ \frac{\mathrm{GW}}{\mathrm{cm}^2}, \qquad I_{\mathrm{ps}}{=}0.81\ \frac{\mathrm{GW}}{\mathrm{cm}^2}, \qquad I_{\mathrm{ns}}{=}1.3\ \frac{\mathrm{GW}}{\mathrm{cm}^2} \tag{4.4}$$

Not considered in Eq. (4.3) is the spectral width of the pulses. If an exciton is only excited by the narrow part of the exciting spectrum which corresponds to half the resonance energy, most of the spectral intensity would not contribute to the excitation. In this case, the gain in intensity due to temporal short pulses is cancelled out by

their broader spectrum. Experience shows that femto- and picosecond pulses induce comparable intense SHG signal, e.g. at the 1S exciton in Cu_2O.

4.1 Scanning method with ns/ps pulses

Before lasers providing femtosecond pulses were installed at the harmonics setup, the scanning method, Fig. 4.2(a), was the standard measurement protocol to acquire nonlinear spectra [13, 14]. These were measured by scanning the wavelength of nanosecond laser pulses in the range of half the energy of the exciton resonances and simultaneously setting the monochromator to the harmonic wavelength. The whole CCD chip is read out and displayed in the programme. There, the pixel values of the signal spot area are integrated to get the overall harmonic intensity for every applied wavelength. As the width of the signal spot at the CCD camera corresponds to spectral width, the resolution of the scanning measurement is determined by the spectral width of the laser. The achieved resolution with this protocol is $0.2 - 1.0$ meV [16] and could be improved by seeding the nanosecond pulses.

An advantage of this measurement type is that the peak intensities in a spectrum can be compared to each other if the laser output power for every wavelength is known. However, the nanosecond laser system provided a repetition rate of 10 Hz which gave a rather low signal-to-noise ratio.

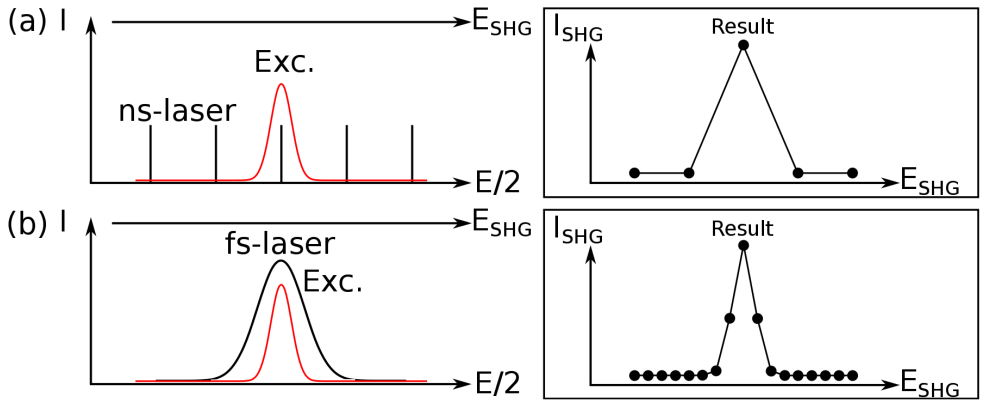

Figure 4.2: Measurement protocol for (a) scanning with ns/ps-excitation and (b) integration with fs-excitation.

4.2 Integration method with fs pulses

When first measurements with femtosecond pulses were run, expectations were not too high. The former nanosecond pulse scanning method in mind, observation of narrow exciton resonances in several semiconductor materials by using femtosecond pulses was surprising. The measurement protocol differs from the nanosecond one, Fig. 4.2(b).

For a SHG measurement, the fs-laser wavelength is set to half the resonance energy. Due to their broad spectral range, the femtosecond pulses do not have to be scanned in wavelength to cover the whole resonance. To display the SHG signal, the columns of the CCD chip are summed up and presented as a spectrum. In this manner, even several close lying resonances in the range of the femtosecond pulse spectrum are detected at once [Fig. 5.3]. In contrast to the ns-scans, the resolution depends on the monochromator and CCD camera instead on the laser. To improve the resolution, a monochromator with higher resolution, e.g. with a grating with more grooves and a CCD camera with smaller pixel size is necessary. This detection technique is particularly suited to measure rotational anisotropies of a group of states by recording a spectrum for each configuration of polarizer and analyzer. Therefore, measurements by fs-pulses consume much less time than by scanning the range of interest with ns-pulses. A spectrum, as shown in Fig. 5.3, takes five minutes with fs-pulses and about 1.5 hours with ns-pulses. However, care has to be taken that while measuring a group of resonances, each resonance is located at a different position in the fs-pulse spectrum and receives a different spectral intensity. To attain correct relative peak intensities, the spectrum has to be normalized to the pulse intensity spectrum.

4.3 Conclusions

The new technique of femtosecond harmonic spectroscopy provides the possibility to measure close lying resonances in short times. The spectral resolution depends on the monochromator and CCD camera. Still, the spectra have to be normalized to the fs-pulse spectral intensity to get correct relative peak intensities.

Despite good measurement results, several questions concerning the usage of femtosecond pulses remain.

(i) How can the excitation by photons at the femtosecond timescale be described? First of all, it should be noted that each photon contains the whole spectrum of the fs-pulse. It would be wrong to assume photons of different energy in the fs-spectrum with the maximum number at the central pulse energy. The spectrum of the fs-pulse is a superposition of modes which are emitted in phase. During excitation within femtoseconds, the exciton resonances are might not as sharp as in long time observation, but are broadened by energy-time uncertainty. Therefore, the resonances might not "pick" the fitting wavelength from the fs-spectrum, but can absorb the whole spectral intensity.

(ii) Can sum-frequency generation (SFG) play a role in fs-SHG experiments? This question is closely connected to (i). It seems possible that the SHG signal of a resonance is not solely induced by the central wavelength of the fs-pulse at half the resonance energy. Additional contributions could arise from two photons which are absorbed due to a frequency part at $E_{\text{resonance}}/2 + \Delta E$ and $E_{\text{resonance}}/2 - \Delta E$. However, simulations indicate that an existing SFG contribution could not be distinguished from "pure" SHG signal.

(iii) Why are resonances not narrow in all semiconductor materials? Measure-

ments and tests with femtosecond pulses so far delivered resonances of at most natural linewidth for the materials Cu_2O, ZnSe, ZnSe quantum wells, Cr_2O_3 and perovskites. Only broad signal structures, instead of distinct lines, were observed with fs-pulses in ZnO, ZnO quantum wells and $KNiF_3$, while they are narrow when measuring with ps-pulses. The reason for these findings are not clear up to now.

Some of these questions could be addressed by using a pulse-shaper which can modify the intensity spectrum and phases of the fs-pulses, e.g. remove the central part of the spectrum to check for SFG contributions in SHG measurements.

In principle, lasers with even shorter pulse duration and broader emission spectra might be favourable in order to further accelerate nonlinear measurements. Nowadays, lasers with pulse durations of tens of attoseconds are available [43] that provide spectral ranges of 60 eV. However, their emission wavelength is located in the extreme UV of only several tens of nm. Therefore, a trade-off between possible wavelength and spectral width is necessary. A suitable configuration could be pulses of 5 fs length that correspond to a width of 400 meV, Eq. (4.2), whereas the maximum wavelength ($\lambda = c/f$) for such a pulse duration is 1500 nm. This is a sufficient wavelength for most SHG and THG measurements of current materials under investigation. Still, the excitation spectrum should not expand beyond the band gap of the sample in second harmonic. Otherwise, two-photon absorption in the exciton continuum could induce photoluminescence. This would overlap with possible harmonic signals at the exciton resonances.

5 Cuprous Oxide

Cu_2O with its illustrative exciton series of large binding energy is well suited for studying fundamental properties of excitons. Being the first semiconductor to show Wannier-Mott excitons [44], Cu_2O attracts continuing interest and excitons of increasing principal quantum number were observed. Matsumoto *et al.* [45] detected S-excitons up to $n = 7$ and P-excitons up to $n = 12$. Recently, Kazimierczuk *et al.* [46] succeeded to observe P-excitons up to $n = 25$. So far, Shen *et al.* [47] found the 1S exciton to be present in SHG spectra. These findings raised the question whether excitons of higher principal quantum number can be observed by the technique of SHG.

The crystal structure of cuprous oxide (Cu_2O) is formed by two sublattices, copper atoms (FCC lattice) and oxygen atoms (BCC lattice), shifted by one quarter of the diagonal of the unit cell. This structure is described in group theory terms by the point group O_h ($m\bar{3}m$). It is the group of highest symmetry and is centrosymmetric. Therefore, the crystal is invariant under inversion of space and, which is equivalent to this statement, parity is strictly a good quantum number. The topmost valence

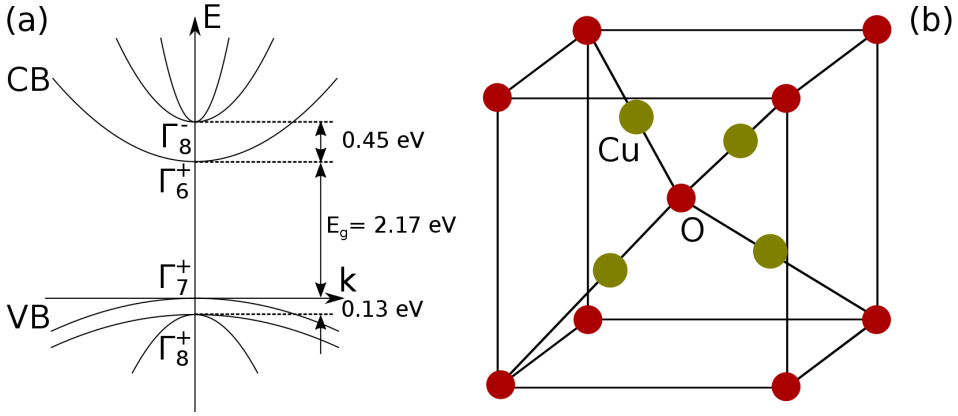

Figure 5.1: (a) Band structure and symmetries of Cu_2O at the Γ-point. (b) Cu_2O unit cell.

bands and lowest conduction bands of the band structure of Cu_2O close to the Γ-point are shown in Fig. 5.1. As their maximum and minimum are at the same k-point, Cu_2O is a direct semiconductor. In contrast to many other semiconductor materials, the valence and conduction bands in Cu_2O originate from orbitals of the same atom species, namely from copper 4S and 3D orbitals, respectively. Bands are labelled with Γ_i^x, with x referring to the band's parity and i giving the irreducible representation in terms of group theory, Sec. 2.6. Four band gaps with energies between $2.17 - 2.75$ eV are defined, each of which is associated with an exciton series. The focus of this section

is put to excitons of the yellow series. Starting by investigation of the 1S exciton state of the yellow series, the measurement technique with femtosecond pulses, as described in Sec. 4.2, is presented. In a second step, excitons of higher principal quantum number n are studied. The effects of internal local strain on the 1S resonance and of external magnetic fields on the higher n states are examined for a set of samples. Insight into mechanisms leading to SHG on the resonances is gained by application of group theory.

5.1 1S exciton

The yellow exciton series' 1S state needs special treatment, as it exhibits a radius of only 10 Å which is only about twice the unit cell size of 4 Å [48]. Therefore, central cell corrections to the 1S binding energy become necessary [49]. Instead of a Rydberg energy of 92 meV [46] as implied by the higher n states, the 1S binding energy, i.e. the difference between band gap energy and 1S resonance, is about 150 meV [50].

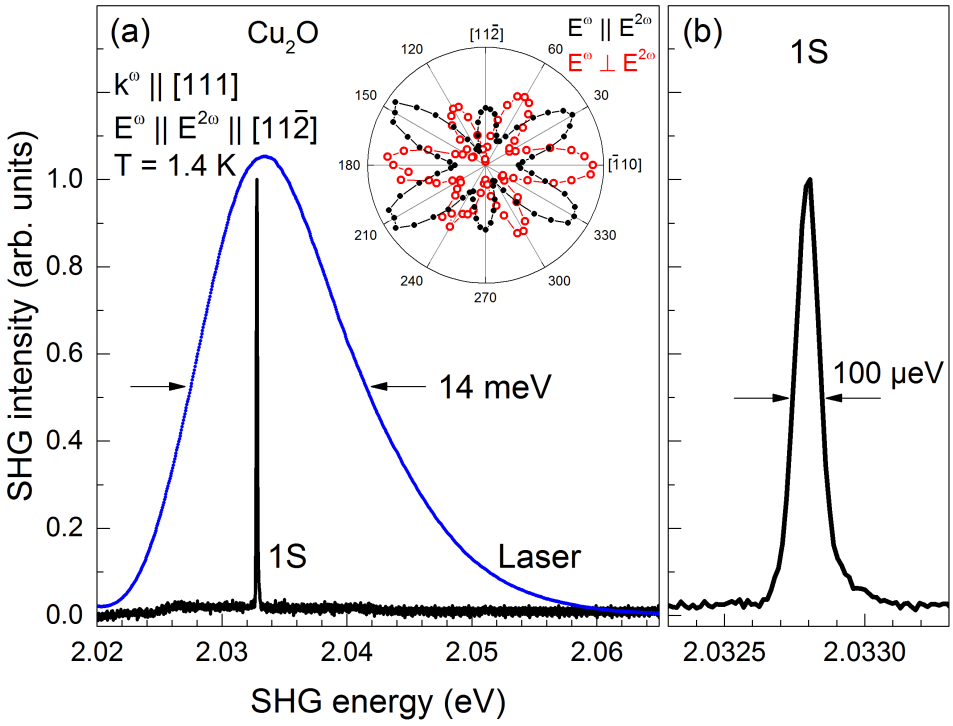

Figure 5.2: (a) SHG spectrum of the 1S exciton at 2.0328 eV for $\mathbf{k}^{\omega} \parallel [111]$ shown by the black line and (b) its close-up. The inset in (a) depicts the SHG rotational anisotropy of the 1S resonance. Filled black and open red dots mark polarization dependences for the geometries $\mathbf{E}^{\omega} \parallel \mathbf{E}^{2\omega}$ and $\mathbf{E}^{\omega} \perp \mathbf{E}^{2\omega}$. The frequency doubled laser spectrum is shown by the blue line.

Another implication of this relatively small radius is that the 1S exciton is spread in k-space over half the Brillouin zone of Cu_2O. This might leads to symmetry deviations from the original exciton symmetry and could allow for new SHG contributions.

In Fig. 5.2(a), the SHG signal upon fs-exciation on the 1S resonance in sample #2A for light **k**-vector along the crystal [111] direction and polarization parallel to $[11\bar{2}]$ is shown (black line). It appears at $E_{1S} = 2.0328$ eV which is in accordance with literature values. To emphasize the remarkably small 1S linewidth despite the broad band femtosecond laser excitation, the laser spectrum, after doubling its frequency by a BBO crystal, is shown (blue line). By detecting the SHG signal with the Acton monochromator (see TABLE 3.1) and the 20 μm-pixel CCD camera, a FWHM of 100 μeV of the 1S resonance is achieved [Fig. 5.2(b)]. An enhancement of resolution is possible by choosing a monochromator of higher resolution and a CCD of smaller pixel size. The 1S line was previously measured with a linewidth of 1 μeV [51]. The inset in Fig. 5.2(a) shows the rotational anisotropy of the 1S resonance for parallel (filled black dots) and crossed (open red dots) configuration. The angle dependence will be analysed in detail in Sec. 5.3.

5.2 Higher n exciton states

Exciton states of increasing principal quantum number n exhibit a decreasing binding energy and are therefore located closer to the band gap energy of Cu_2O (2.17 eV) [46]. For two-photon excitation of the exciton states the femtosecond laser photon energy is set to $E^{\omega} = 1.082$ eV (1146 nm). The experimental result for Cu_2O (sample H24) with the light **k**-vector parallel to [111] crystal direction is shown in Fig. 5.3. In panel (a), the SHG spectrum for $2.13 - 2.18$ eV is plotted in red and compared to a whitelight transmission spectrum in black. Panel (b) is a close-up of the energy range of $2.160 - 2.173$ eV. The SHG spectrum was measured within 5 min by the newly introduced method of femtosecond spectroscopy. By scanning with nanosecond pulses, the detection of such a spectrum would have taken more than an hour. Comparison of peak energies with [46, 49] allows to assign exciton states up to $n = 9$. Although being aware of the fact that S- and D-excitons are mixed states by the H_d term [50], resonances are labelled solely by S or D, depending on the main contribution of either S- or D-wave function.

White light transmission and SHG show complementary results. In white light transmission, one-photon dipole allowed odd-parity P-excitons are resolved, while in SHG two-photon dipole allowed even-parity S- and D-excitons are the most intense resonances. Still, there are indications of some of the P-excitons, e.g. the 2P, present. As will be discussed in the next section, the SHG processes for even- and odd-parity excitons contain one quadrupole transition each. From this point of view, they should feature similar intensities. However, the ratio of the susceptibility tensors for the n-th S- and P-excitons are expected to be proportional to the P-exciton binding energy to

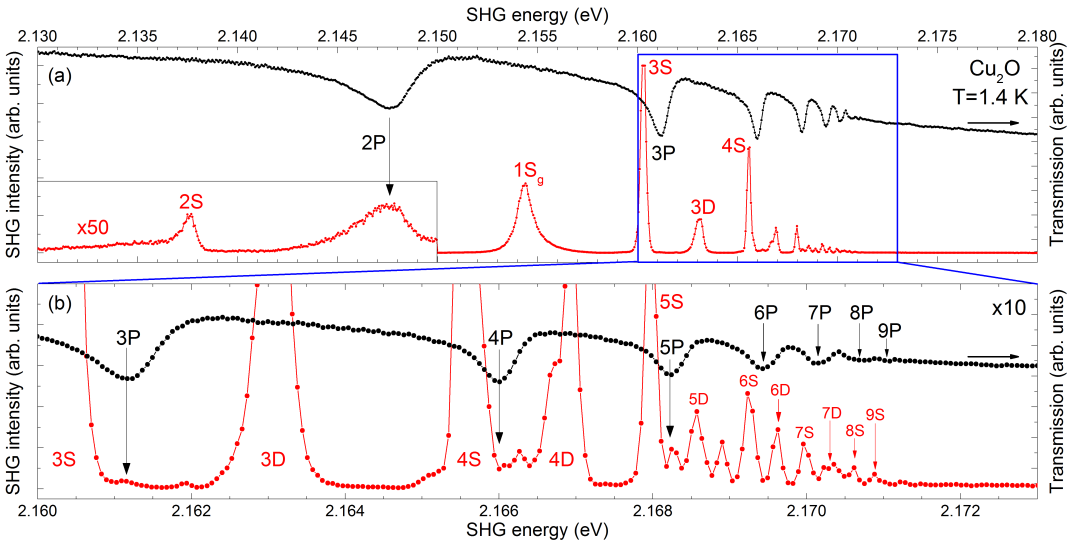

Figure 5.3: SHG spectrum (red) of Cu_2O (sample #24) measured in the $\mathbf{E}^{\omega} \parallel \mathbf{E}^{2\omega} \parallel [11\bar{2}]$ configuration with the photon energy of the fundamental laser set to 1.082 eV and resonant white light transmission spectrum (black), both for $\mathbf{k}^{\omega} \parallel [111]$. (a) Energy range from the $n = 2$ exciton up to more than the band gap of 2.17208 eV [46]. Left inset shows the $2S$ and $2P$ resonances, enlarged by a factor of 50. (b) Close-up of the SHG spectrum with an enlargement factor of 10.

the Cu_2O band gap energy [52], i.e.:

$$\frac{\chi^{nP}}{\chi^{nS}} \propto \frac{E_{nP}^{\text{bind}}}{E_{\text{g}}^{\text{Cu}_2\text{O}}}. \tag{5.1}$$

As this ratio is proportional, it can only be proved by comparing the intensities of S- and P-excitons of different n. To do so, more pronounced SHG P-exciton resonances would be necessary than in Fig. 5.3.

Examples of rotational anisotropies for the 2P and 3S resonances are plotted in Fig. 5.4. Both show mainly sixfold shapes for $\mathbf{E}^{\omega} \parallel \mathbf{E}^{2\omega}$ and $\mathbf{E}^{\omega} \perp \mathbf{E}^{2\omega}$. These results are simulated by a group theory approach in the next section. Selection rules are derived and calculations discussed.

5.3 Exciton symmetry selection rules

Selection rules are derived by a group theory ansatz. The irreducible representations, Γ_i, assigned to excitons and calculations performed on them can be found in the tables in Koster *et al.* [33]. A thorough calculation with explanations, starting from the very beginning with electron quantum numbers, is given in the Appendix B.

The symmetries of different excitons, labelled by their envelopes, are deduced by Eq. (2.29). As shown in Fig. 5.1(a), the conduction band and valence band of the

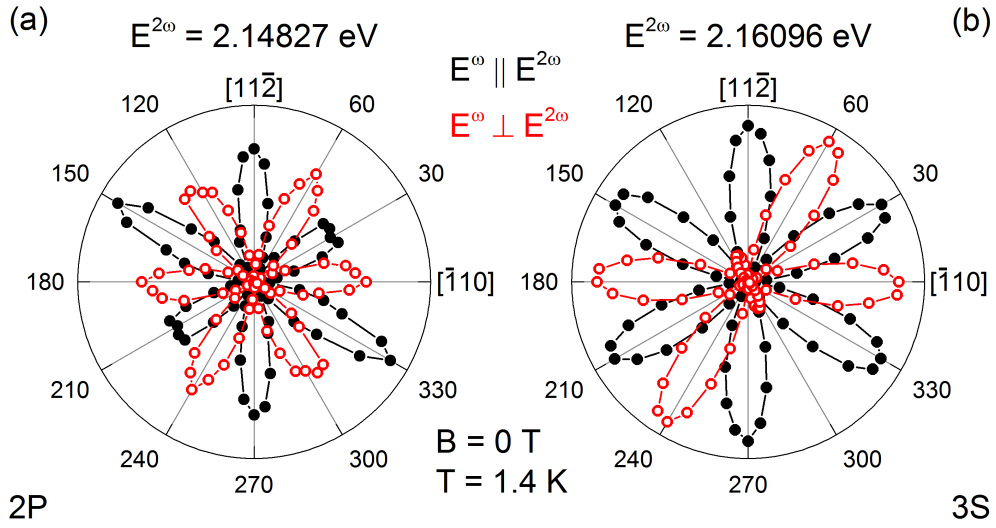

Figure 5.4: SHG rotational anisotropies in sample #2 of (a) 2P exciton resonance and (b) 3S exciton resonance. Solid (black) and open (red) circles represent data for the $\mathbf{E}^{\omega} \parallel \mathbf{E}^{2\omega}$ and $\mathbf{E}^{\omega} \perp \mathbf{E}^{2\omega}$ configurations, respectively.

yellow exciton series posses Γ_6^+ and Γ_7^+ symmetry, respectively. The envelope of an S-exciton is represented by Γ_1^+ symmetry, that of a P-exciton by Γ_4^-. Therefore, the exciton symmetries are:

$$\Gamma_{\mathrm{S}} = \Gamma_6^+ \otimes \Gamma_7^+ \otimes \Gamma_1^+ = \Gamma_2^+ \oplus \Gamma_5^+, \tag{5.2}$$

$$\Gamma_{\mathrm{P}} = \Gamma_6^+ \otimes \Gamma_7^+ \otimes \Gamma_4^- = \Gamma_5^- \oplus \left(\Gamma_2^- \oplus \Gamma_3^- \oplus \Gamma_4^- \oplus \Gamma_5^-\right). \tag{5.3}$$

Those symmetries printed in red correspond to para-excitons which are entirely triplet states and are spin forbidden to all orders. They are not considered here. In the Appendix B, the derivation of the spin of states is presented.

One- and two-photon operators in dipole and quadrupole order in the point group O_h are represented by:

$$\text{one photon, dipole} \quad : \quad \Gamma_4^-, \tag{5.4}$$

$$\text{one photon, quadrupole} \quad : \quad \Gamma_3^+ \oplus \Gamma_5^+, \tag{5.5}$$

$$\text{two photons, dipole-dipole} \quad : \quad \Gamma_1^+ \oplus \Gamma_3^+ \oplus \Gamma_4^+ \oplus \Gamma_5^+, \tag{5.6}$$

$$\text{two photons, dipole-quadrupole} \quad : \quad \Gamma_2^- \oplus \Gamma_3^- \oplus \Gamma_4^- \oplus \Gamma_5^-. \tag{5.7}$$

Possible transitions are obtained strait forwardly by comparing the symmetries of photon operators and exciton states. An even parity S-exciton state of Γ_5^+ symmetry is two-photon dipole allowed. To observe SHG, one photon of the same symmetry as the exciton has to be emitted, too. Therefore, as Shen *et al.* [47] showed, only emission of one photon in quadrupole order is allowed. Here, also P-excitons are present in

the SHG spectrum. Their appearance is explained by group theory by a change in the mechanism. Due to their odd envelope parity, P-excitons have odd parity in total. Two-photon excitation of a Γ_4^- symmetry exciton is still possible if one photon is considered to be in quadrupole order (see Eq. 5.7). In contrast to S-excitons, one photon in dipole order can be emitted. Both mechanisms are compared in Fig. 5.5. After all, symmetry is only a necessary condition to observe a resonance and does not tell anything about exciton energies.

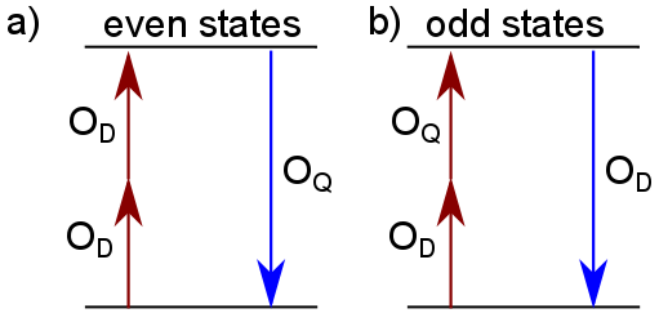

Figure 5.5: Sketch of resonant SHG processes for (a) the even- and (b) odd-parity exciton states in Cu_2O of the point group O_h.

To gain further insight into the symmetries of the states and to simulate the rotational anisotropies, it is necessary to calculate the components of the irreducible representations. With the use of the tables of Koster *et al.* [33], the polarization dependence of the SHG signals for linearly polarized light is determined. Relevant definitions of directions and angles, as shown in Fig. 3.2, are given below.

The ingoing photons are described by their wave vector $\mathbf{k}^{\omega}$ and polarization $\mathbf{E}^{\omega}$. The polarization components u, v and w depend on the incoming polarization angle ψ. Emitted photons have wave vector $\mathbf{k}^{2\omega}$ with components k_x, k_y and k_z and polarization $\mathbf{E}^{2\omega}$. The polarization components m, n and o depend on the outgoing polarization angle φ.

$$\mathbf{E}^{\omega} = \begin{pmatrix} u(\psi) \\ v(\psi) \\ w(\psi) \end{pmatrix}, \quad \mathbf{E}^{2\omega} = \begin{pmatrix} m(\varphi) \\ n(\varphi) \\ o(\varphi) \end{pmatrix}, \quad \mathbf{k}^{2\omega} = \begin{pmatrix} k_x \\ k_y \\ k_z \end{pmatrix}. \tag{5.8}$$

Note, that $\mathbf{k}^{\omega}$ and $\mathbf{k}^{2\omega}$ are parallel and $\mathbf{k}^{2\omega}$ is twice as large as $\mathbf{k}^{\omega}$. The absolute length of the $\mathbf{k}^{i\omega}$ can be neglected in the calculations. Therefore, the k_i are unit direction vector components.

An S-exciton can be excited by two photons in dipole order. The operator O_{TPDD} resulting from $\mathbf{E}^{\omega}(\psi) \otimes \mathbf{E}^{\omega}(\psi) = \Gamma_4^- \otimes \Gamma_4^- \rightarrow \Gamma_5^+$ is given explicitly by:

$$O_{\mathrm{TPDD}}(\mathbf{E}^{\omega}) = \sqrt{2} \begin{pmatrix} v(\psi)w(\psi) \\ u(\psi)w(\psi) \\ u(\psi)v(\psi) \end{pmatrix}. \tag{5.9}$$

The operator O_{Q} for the emitted photon in quadrupole order ($\mathbf{k}^{\omega} \otimes \mathbf{E}^{\omega}(\psi) = \Gamma_4^- \otimes \Gamma_4^- \rightarrow \Gamma_5^+$) forms to:

$$O_{\mathrm{Q}}(\mathbf{k}^{2\omega},\, \mathbf{E}^{2\omega}) = \frac{1}{\sqrt{2}} \begin{pmatrix} k_{\mathrm{y}} o(\varphi) & + & k_{\mathrm{z}} n(\varphi) \\ k_{\mathrm{z}} m(\varphi) & + & k_{\mathrm{x}} o(\varphi) \\ k_{\mathrm{x}} n(\varphi) & + & k_{\mathrm{y}} m(\varphi) \end{pmatrix} = \mathbf{q}^{\omega}. \tag{5.10}$$

SHG signal is only present if both processes, the two-photon absorption and the one-photon emission, address the same exciton component for the same polarization angles ψ and φ. The intensity of the SHG signal from even-parity excitons, $I^{2\omega}_{\mathrm{even}}$, is proportional to the square of the product of the operators O_{TPDD} and O_{Q}:

$$I^{2\omega}_{\mathrm{even}} \propto |O_{\mathrm{TPDD}} \cdot O_{\mathrm{Q}}|^2. \tag{5.11}$$

In case odd-parity states are considered, the operators needed are O_{TPDQ} for two-photon exciation by dipole and quadrupole and O_{D} for emission of one dipole:

$$O_{\mathrm{TPDQ}}(\mathbf{E}^{\omega},\, \mathbf{q}^{\omega}) = \frac{1}{\sqrt{2}} \begin{pmatrix} v(\psi) q_{\mathrm{z}}(\psi) + w(\psi) q_{\mathrm{y}}(\psi) \\ w(\psi) q_{\mathrm{x}}(\psi) + u(\psi) q_{\mathrm{z}}(\psi) \\ u(\psi) q_{\mathrm{y}}(\psi) + v(\psi) q_{\mathrm{x}}(\psi) \end{pmatrix}, \tag{5.12}$$

$$O_{\mathrm{D}}(\mathbf{E}^{2\omega}) = \begin{pmatrix} m(\varphi) \\ n(\varphi) \\ o(\varphi) \end{pmatrix}. \tag{5.13}$$

The intensity of the SHG signal from odd-parity excitons, $I^{2\omega}_{\mathrm{odd}}$, is proportional to the square of the product of the operators O_{TPDQ} and O_{D}:

$$I^{2\omega}_{\mathrm{odd}} \propto |O_{\mathrm{TPDQ}} \cdot O_{\mathrm{D}}|^2. \tag{5.14}$$

The two configurations $\mathbf{E}^{\omega} \parallel \mathbf{E}^{2\omega}$ and $\mathbf{E}^{\omega} \perp \mathbf{E}^{2\omega}$ can be realized by setting $\psi = \varphi$ and introduce an offset $\varphi = \psi + 90°$, respectively.

In the next step, the rotational anisotropy for light vector $\mathbf{k}$ along the crystal [111]-direction is calculated. The components of $\mathbf{E}^{\omega}$, $\mathbf{E}^{2\omega}$ and $\mathbf{k}$ in Eq. (5.8) are:

$$\mathbf{E}^{\omega}(\varphi) = \mathbf{E}^{2\omega}(\varphi) = \frac{1}{\sqrt{6}} \begin{pmatrix} \cos(\varphi) - \sqrt{3}\sin(\varphi) \\ \cos(\varphi) + \sqrt{3}\sin(\varphi) \\ -2\cos(\varphi) \end{pmatrix}, \qquad \mathbf{k}^{\omega} = \frac{1}{\sqrt{3}} \begin{pmatrix} 1 \\ 1 \\ 1 \end{pmatrix}. \tag{5.15}$$

The resulting polarization angle dependent intensities for the configurations $\mathbf{E}^{\omega} \parallel \mathbf{E}^{2\omega}$ and $\mathbf{E}^{\omega} \perp \mathbf{E}^{2\omega}$are:

$$I^{2\omega}_{\parallel} \propto \cos^2(3\varphi), \tag{5.16}$$

$$I^{2\omega}_{\perp} \propto \sin^2(3\varphi). \tag{5.17}$$

There is no difference in the angle dependence between even- and odd-parity states for $I^{2\omega}_{\parallel}$ and $I^{2\omega}_{\perp}$ in absence of external fields.

5.4 Circular polarization

Usually, SHG spectra, in the absence of magnetic fields, are measured with linearly polarized light for excitation and emission. Those measurements are extended by spectra with circularly polarized photons for excitation and detection with light **k**-vector parallel to [111]. Therefore, the half-wave plates in the setup, Fig. 3.1, are replaced with quarter-wave plates.

In Fig. 5.6, spectra are shown for linear polarization (as before) and for all combinations of circular polarization for incoming and outgoing photons. The spectra are

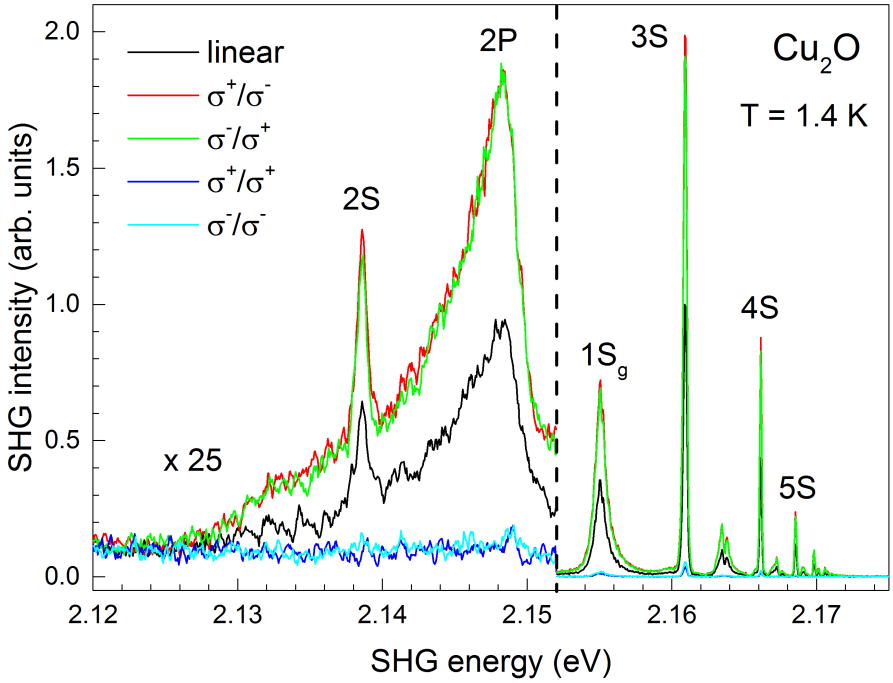

Figure 5.6: Polarization dependence of SHG spectra in Cu_2O (sample #2) for $\mathbf{k}^{\omega} \parallel [111]$. The linear polarization setting is $\mathbf{E}^{\omega} \parallel \mathbf{E}^{2\omega} \parallel [11\bar{2}]$. For the low energy side the central laser energy is set to 1.073 eV and for the high energy side to 1.082 eV. The spectra are normalized to the maximum SHG intensity in linear polarization (at $2P$ for left side and at $3S$ for right side). Note the multiplication factor of 25 for the weaker signals on the left side.

divided at 2.152 eV (dashed vertical line) and the weaker signals on the left side multiplied by a factor of 25. Whereas there is no signal for exciation and detection of the co-circular polarization, signal is higher than with linear polarized light for crossed alignment of excitation and detection polarization.

For circular polarized light the same formulas can be applied as for linear polarized light, Eqs. (5.9 - 5.13). It is necessary to introduce for any arbitrary **k** direction two

orthogonal vectors $\mathbf{d}(x,y,z)$ and $\mathbf{e}(x,y,z)$ as basis vectors for the complex polarization vectors $\sigma^+(x,y,z)$ and $\sigma^-(x,y,z)$ [53]. The result is:

$$\mathbf{k} = \begin{pmatrix} k_x \\ k_y \\ k_z \end{pmatrix}, \quad \mathbf{d} = \begin{pmatrix} 1 - k_x^2/(1+k_z) \\ -k_x k_y/(1+k_z) \\ -k_x \end{pmatrix}, \quad \mathbf{e} = \begin{pmatrix} -k_x k_y/(1+k_z) \\ 1 - k_y^2/(1+k_z) \\ -k_y \end{pmatrix}. \tag{5.18}$$

From these orthogonal polarization vectors the circular polarization vectors are defined as:

$$\sigma^+ = \frac{\mathbf{d} - i \cdot \mathbf{e}}{\sqrt{2}} \quad \text{and} \quad \sigma^- = \frac{\mathbf{d} + i \cdot \mathbf{e}}{\sqrt{2}}. \tag{5.19}$$

The SHG signals for the different polarization combinations of ingoing and outgoing photons are thus given by:

$$I^{2\omega}_{\mathrm{RR,\ even}} \propto |O_{\mathrm{TPDD}}(\sigma^+) \cdot O_{\mathrm{Q}}(\sigma^+)|^2, \tag{5.20}$$

$$I^{2\omega}_{\mathrm{RL,\ even}} \propto |O_{\mathrm{TPDD}}(\sigma^+) \cdot O_{\mathrm{Q}}(\sigma^-)|^2, \tag{5.21}$$

$$I^{2\omega}_{\mathrm{RR,\ odd}} \propto |O_{\mathrm{TPDQ}}(\sigma^+) \cdot O_{\mathrm{D}}(\sigma^+)|^2, \tag{5.22}$$

$$I^{2\omega}_{\mathrm{RL,\ odd}} \propto |O_{\mathrm{TPDQ}}(\sigma^+) \cdot O_{\mathrm{D}}(\sigma^-)|^2. \tag{5.23}$$

The results for $\mathbf{k}^\omega \parallel [111]$ are summarized in Table 5.1 Four configurations of circularly

Table 5.1: Relative intensities for linearly and circularly polarized SHG signals in Cu_2O for $\mathbf{k}^\omega \parallel [111]$.

in/out	lin/lin	σ^+/σ^+	σ^-/σ^-	σ^+/σ^-	σ^-/σ^+
O_h even	1/18	0	0	1/9	1/9
O_h odd	2/9	0	0	4/9	4/9

polarized light, labelled by the polarization of "in/out", can be examined. Obviously, SHG is forbidden for the co-circular polarization configurations σ^+/σ^+ and σ^-/σ^-, but allowed for the crossed-circular polarizations σ^+/σ^- and σ^-/σ^+. For the allowed configurations the intensity of the circularly polarized SHG is by a factor of 2 larger than for linearly polarized light. This is valid for both, even and odd parity exciton states. These calculations fit perfectly the measurement results and are a direct consequence of the crystal structure and $\mathbf{k}$-direction. For $\mathbf{k}^\omega \parallel [111]$ the symmetry operations of the point group C_{3v} leave the $\mathbf{k}$-vector invariant. Therefore, the magnetic quantum number of the photons is conserved under modulo 3, i.e. $\pm 2 = \mp 1$. The sum of two photons of ± 1 can excite a state of ∓ 1 which finally emits a photon of corresponding polarization.

5.5 SHG on the 1S exciton in symmetry forbidden crystal directions

Measurements in the last section were focussed on the $\mathbf{k}^\omega \parallel [111]$ direction and excitons with principal quantum number $n \geqslant 2$. This section deals exclusively with the 1S

ortho exciton and the experimental finding of SHG signals on this resonance for light incident along forbidden crystal directions (e.g. $\mathbf{k}^{\omega} \parallel [\bar{1}10]$ and [001]). These directions are called forbidden because, according to Eqs. (5.9 - 5.11), no signal is expected by symmetry considerations. Furthermore, in SHG allowed crystal directions (e.g. $[11\bar{2}]$ and [111]) the rotational anisotropies show deviations from the calculated results.

In a previous experiment on time-resolved two-photon emission [54] a similar observation was made. After resonant quadrupole excitation of a 1S component, a delayed signal from an orthogonal 1S component was detected. These findings were explained by relaxation processes between exciton components. By measuring SHG the situation is different. The exciton-polariton is excited resonantly by two photons through dipole transitions at smaller wave vector (due to smaller refractive index at half the photon energy) and lower energy (due to spatial dispersion) than the previous resonant excitation by a one-photon quadrupole transition.

In the experiments, Cu_2O samples of different orientation and thickness are used whose parameters are given in Table 5.2.

Table 5.2: List of studied Cu_2O crystals and their parameters.

sample	$\mathbf{k}^{\omega} \parallel$ [...]	thickness (μm)
#34	[001]	264
#33	[001]	45
#13	$[\bar{1}10]$	252
#29	$[11\bar{2}]$	95
#2A	[111]	3874
#2B	$[11\bar{2}]$	5103

5.5.1 Experimental results

In Fig. 5.7, the spectral range of the yellow exciton series, $2.032 - 2.175$ eV, is shown with a break from 2.034 to 2.148 eV. Exciton resonances are marked with their principal quantum number and main orbital angular momentum contribution to the envelope [46]. The resonance at 2.155 eV, labelled as $1S_g$, is the 1S exciton of the green series, following the assignment of [49]. Spectra and SHG polarization dependences for an allowed orientation ((a) $\mathbf{k}^{\omega} \parallel [11\bar{2}]$) and a forbidden orientation ((b) $\mathbf{k}^{\omega} \parallel [001]$) are presented. For $\mathbf{k}^{\omega} \parallel [11\bar{2}]$ SHG is allowed and, just as in Sec. 5.2, resonances of S- and D-excitons of the yellow series appear. The polarization dependences for the 1S and 3S excitons, however, show clear differences, which gives already evidence for different SHG mechanisms for the 1S and the higher resonances. For the forbidden orientation $\mathbf{k}^{\omega} \parallel [001]$ only the 1S resonance of the yellow series is present in the SHG spectrum, while the resonances with higher n are absent in accordance with symmetry analysis.

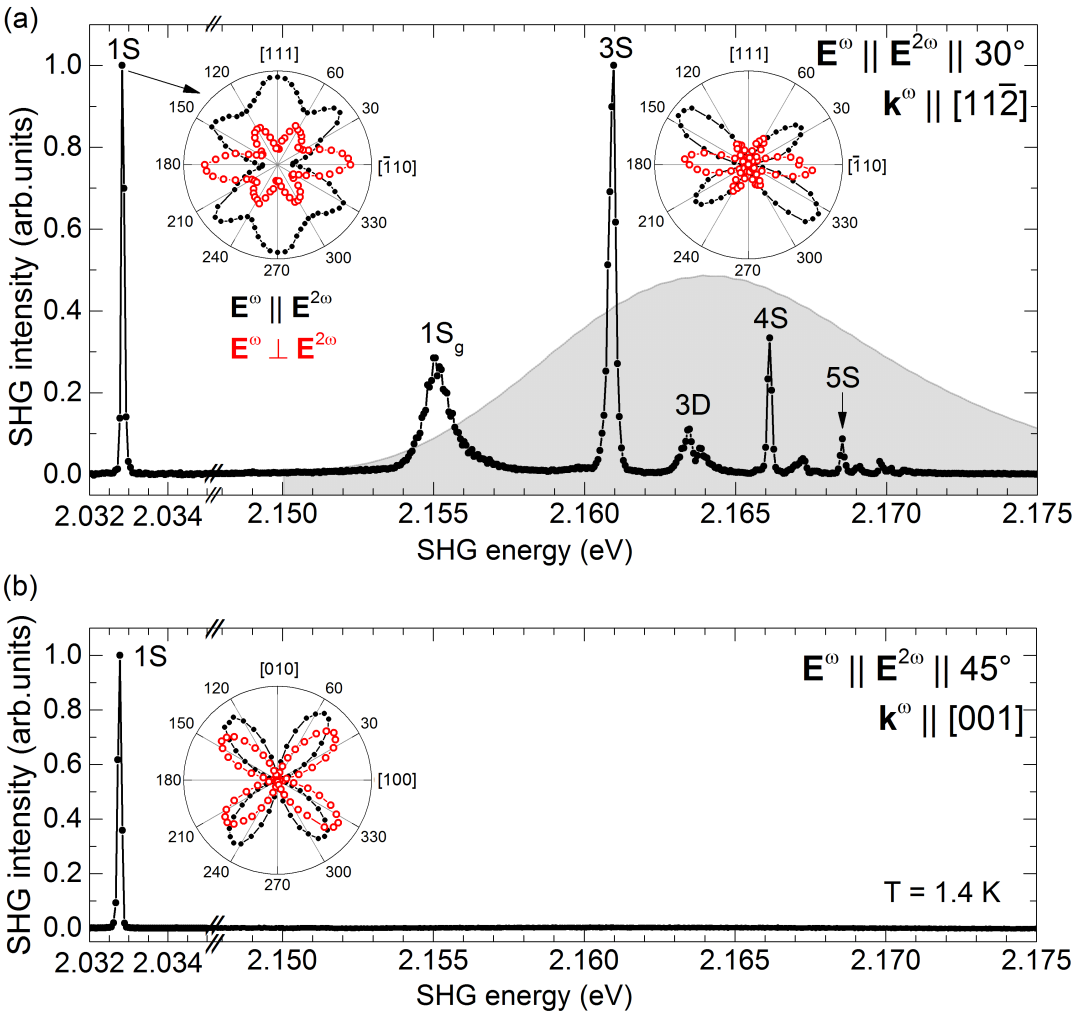

Figure 5.7: SHG spectra of Cu_2O for (a) sample #29 with $\mathbf{k}^{\omega} \parallel [11\bar{2}]$ and (b) sample #34 with $\mathbf{k}^{\omega} \parallel [001]$. The laser photon energy is set to 1.016 eV for the 1S resonance and to 1.082 eV for the higher exciton resonances. Note the different low and high energy scales divided by break lines. The energy range around the 2S exciton is not shown here. Exciton line intensities in the higher energy range are enlarged by a factor of 10 to meet the intensity of the 1S line ((a), (b)). The SHG peak intensities are not normalized to the laser spectrum (indicated by the grey shaded area). Insets in panel (a) show SHG rotational anisotropies of the 1S and 3S excitons and in panel (b) for the 1S exciton. The other high n excitons show the same rotational anisotropies as the 3S exciton. Filled black and open red circles represent data for the $\mathbf{E}^{\omega} \parallel \mathbf{E}^{2\omega}$ and $\mathbf{E}^{\omega} \perp \mathbf{E}^{2\omega}$ configurations, respectively.

In Fig. 5.7(a), the linewidth of the yellow 1S resonance has a full width at half maximum (FWHM) of 100 μeV being limited by the setup spectral resolution. Two-photon absorption experiments determined in similar Cu_2O samples a 1S linewidth of about 1 μeV [51]. All other exciton resonances have larger linewidths not limited by the setup, e.g. the 3S resonance has a FWHM of 290 μeV.

In Fig. 5.8, the rotational anisotropies of the 1S exciton for two allowed and two forbidden crystal directions are shown. SHG signal intensities in forbidden and allowed directions are of the same order of magnitude, but angular dependencies are quite different.

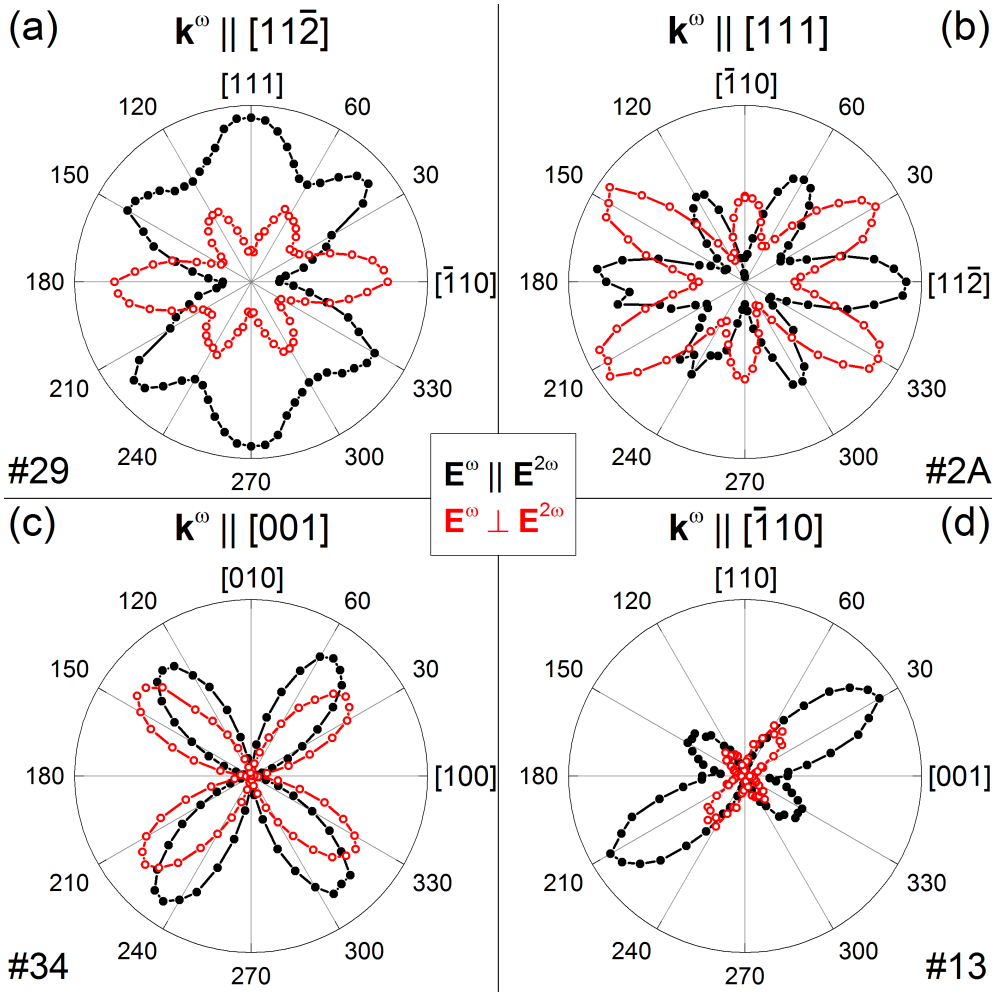

Figure 5.8: SHG rotational diagrams of 1S exciton at 2.0328 eV in four crystal directions: (a) and (b) refer to results in allowed directions, whereas (c) and (d) refer to forbidden directions. Filled black and open red dots refer to parallel respectively perpendicular polarizations of in- and outgoing photons. Sample numbers are given by #number.

From linear spectroscopy it is well known for Cu_2O that strain-induced effects play a crucial role and were reported in Refs. [51, 55]. Strain parameters were investigated experimentally in Ref. [56] and theoretically in Ref. [57]. As the samples are mounted strain-freely, as described in detail in Ref. [51], internal local strain [58] is suggested to be the reason of symmetry breaking and the observation of unexpected SHG signals.

To test this hypothesis, spatially-resolved SHG of the yellow 1S resonance at 2.0328 eV is measured. In order to illustrate the local dependence of the SHG signals on sample position, a 7× magnifying telescope instead of the focusing lens of the laser on the sample is used. Thus a large part of the sample is illuminated. The cross section of the sample is mapped to the CCD chip by opening the monochromator slit to 3 mm and setting its grating to zero order. Therefore, all light is reflected without dispersion by the grating to the CCD camera.

SHG signal of the whole sample area 3×3 mm^2 (sample #13 with $\mathbf{k} \parallel [\bar{1}10]$) is shown in Fig. 5.9. The colormap corresponds to SHG intensity. Two SHG spots on the sample, denoted by a and b, are chosen and their rotational anisotropies are plotted in Fig. 5.10. As it will be shown by model analysis in Sec. 5.5.4, the appearance of SHG signal for $\mathbf{k}^{\omega} \parallel [\bar{1}10]$, and the differences in polarization dependences at various spots are induced due to local strains of different amplitude and orientation.

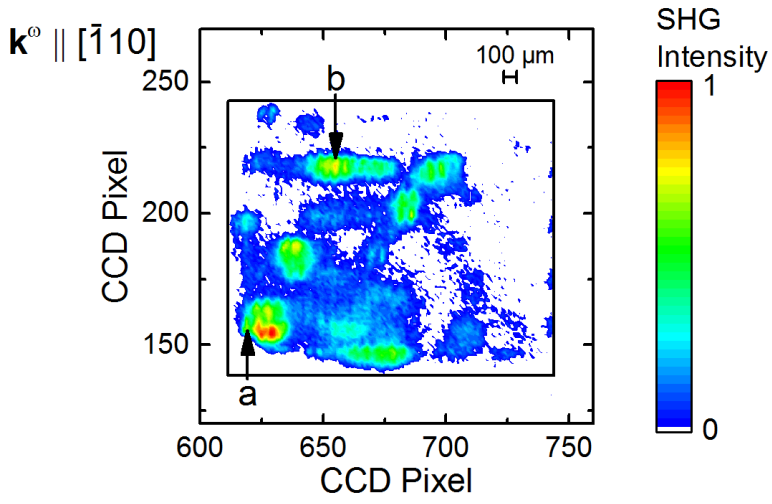

Figure 5.9: Spatially resolved 1S SHG image of the sample #13 in a forbidden orientation ($\mathbf{k}^{\omega} \parallel [\bar{1}10]$) at 2.0328 eV. Observed SHG signals are induced by local strains. The area shown corresponds to 3×3 mm^2. At spots a and b rotational anisotropies are measured for comparison and shown in Fig. 5.10.

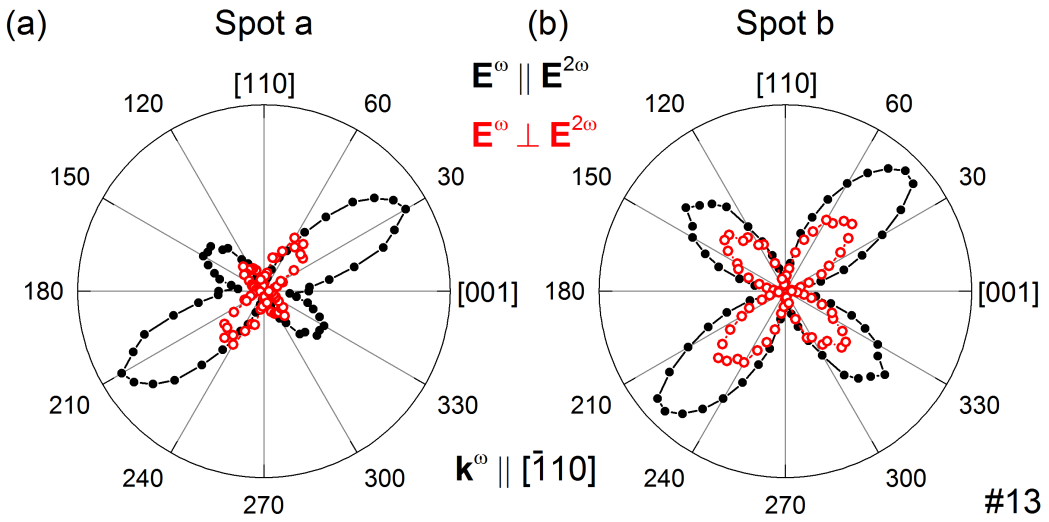

Figure 5.10: SHG rotational anisotropies of the yellow 1S exciton at 2.0328 eV of spots a and b of the sample #13 with $\mathbf{k}^\omega \parallel [\bar{1}10]$ as marked in Fig. 5.9. Filled black and open red dots mark data points of parallel and crossed configurations, respectively.

To prove the assumption of local strain as SHG origin and gain insight into the strain parameters, such as the strain tensor components, the experimental rotational anisotropies are simulated in the successive sections. The model and fitting procedure are described below.

5.5.2 Theory of SHG in forbidden crystal directions

In this section, the derivation of polarization dependences, as outlined in Sec. 5.3, is extended, to include strain induced perturbations and also band structure higher order effects. It explains the experimental findings of unexpected SHG by the presence of residual strain in the Cu_2O samples.

More specifically, the formalism includes the **k**-dependent splitting of the 1S longitudinal and transversal components, which is explained as an effect of the band structure in Ref. [58]. It also considers the mixing of these components by local strain. First, the main concepts are presented in four steps that are needed for the simulation of experimental results in Sec. 5.5.3.

Photon operators For the analysis of SHG signals on exciton resonances the definitions in Eqs. (5.8 – 5.11) are used for the polarizations of the incoming and outgoing photons. As a result, the intensity of the SHG signal is given by:

$$I^{2\omega} \propto |(O_{\mathrm{TPDD}} \cdot O_{\mathrm{Q}})|^2. \tag{5.24}$$

If Eq. (5.24) is calculated for laser light with $\mathbf{k}^\omega$ along different crystal directions, SHG is expected only for low symmetry crystal directions as e.g. [111] and $[11\bar{2}]$, while it is

forbidden for $\mathbf{k}^{\omega} \parallel [001]$ and $[\bar{1}10]$. Therefore, modification of Eq. (5.24) is necessary to explain the experimental results for the 1S exciton in both, the allowed and forbidden directions.

k^2-dependent splitting of the 1S exciton The 1S orthoexciton is known for a small wave vector dependent splitting of its longitudinal and transversal components showing up in high resolution transmission measurements [51]. This splitting is explained by a coupling between the Γ_7^+ and Γ_8^+ valence band leading to an anisotropic exciton mass of the three exciton states [58]. It was shown in Ref. [51] that the splitting for one-photon excitation can be consistently described by two parameters Δ_3=-1.3 μeV and Δ_5=2 μeV. Calculations by Schweiner *et al.* [58] yield the slightly different values Δ_3=-1.45 μeV and Δ_5=1.96 μeV.

For two-photon excitation, however, $2\mathbf{k}^{\omega} < \mathbf{k}_0$ (wave number at one-photon resonance). From the polariton dispersion $\Delta_{3,(5)}\left(\mathbf{k}^{2\omega}\right) \sim 0.8\Delta_{3,(5)}\left(\mathbf{k}_0\right)$ is estimated, which are the values used in the following calculations. The k^2 matrices J_3 and J_5 are given in Refs. [51, 58]:

$$J_3 = \Delta_3 \begin{pmatrix} 3k_x^2 - k^2 & 0 & 0 \\ 0 & 3k_y^2 - k^2 & 0 \\ 0 & 0 & 3k_z^2 - k^2 \end{pmatrix} \tag{5.25}$$

and

$$J_5 = \Delta_5 \begin{pmatrix} 0 & k_x k_y & k_x k_z \\ k_x k_y & 0 & k_y k_z \\ k_x k_z & k_y k_z & 0 \end{pmatrix}. \tag{5.26}$$

From these matrices one can, on the one hand, determine the modification of the exciton states by the $\boldsymbol{k}^2$ term and, on the other hand, also the impact on the photon operators determining the SHG. From the structure of the matrices, it is obvious that J_3 shifts the exciton components in energy, leading to a splitting, but does not induce state mixing. Consequently, also the components of the photon operators remain unconnected when J_3 acts on them.

Mixing can be achieved through J_5 which depends, however, strongly on the direction in k-space. Along the SHG-forbidden direction [001] it is suppressed, whereas along $[\bar{1}10]$, the transverse components of the photon operators along x and y remain disconnected from the longitudinal component along z. The consequences for SHG will be discussed below. Along the directions of even lower symmetry, for which SHG is allowed anyway, J_5 modifies the mixing of the photon operator components involved in the process.

Strain tensors The strain is described by matrices M_3 and M_5 of the same structure as J_3 and J_5 in Eqs. (5.25) and (5.26). The uniaxial strain that can lift the degeneracy

of states without mixing them is given by M_3,

$$M_3 = \delta_3 \begin{pmatrix} \epsilon_x & 0 & 0 \\ 0 & \epsilon_y & 0 \\ 0 & 0 & \epsilon_z \end{pmatrix} \tag{5.27}$$

with $\epsilon_i = 3\epsilon_{ii}^2 - \frac{1}{3}(\epsilon_{xx}^2 + \epsilon_{yy}^2 + \epsilon_{zz}^2)$.

Matrix M_5 represents the shear strain which can mix exciton components,

$$M_5 = \delta_5 \begin{pmatrix} 0 & \epsilon_{xy} & \epsilon_{xz} \\ \epsilon_{xy} & 0 & \epsilon_{yz} \\ \epsilon_{xz} & \epsilon_{yz} & 0 \end{pmatrix}. \tag{5.28}$$

ϵ_{ij}'s are the strain tensor components. For the deformation potentials δ_i, values given in Ref. [59] are used for the uniaxial strain $\delta_3 = -0.29$ eV and shear strain $\delta_5 = 0.18$ eV.

Summarizing these additional factors, a splitting of the exciton components can be induced by the strain and the k^2 term, as schematically shown in Fig. 5.11(b). It is, however, a priori not possible to estimate whether one effect dominates the other or one effect can be treated as a small perturbation compared to the other. Therefore, the sum matrix S, Eq. (5.29), of both needs to be diagonalized

$$S = J_3 + J_5 + M_3 + M_5. \tag{5.29}$$

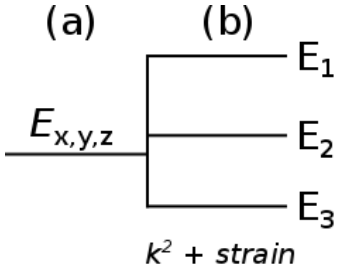

Figure 5.11: General splitting of the exciton components. (a) Unperturbed exciton states $E_{\mathrm{x,y,z}}$. (b) New exciton eigenstates $E_{1,2,3}$, split in energy and mixed by the k^2 and strain terms.

Turning to the impact on SHG, generally, S can couple the components x, y and z of the two-photon excitation operator O_{TPDD}, Eq. (5.9). This coupling results in new components x', y' and z' of O'_{TPDD} allowing for new SHG contributions,

$$O'_{\mathrm{TPDD}} = S \cdot O_{\mathrm{TPDD}}. \tag{5.30}$$

Calculation of strain induced SHG Considered are only the three 1S orthoexciton components of Γ_5^+ symmetry. The first requirement for strain induced SHG is the two-photon excitation of components mixed by the strain. In a second step, emission by one photon in quadrupole order has to be allowed to observe SHG signal. Therefore, in Eq. (5.31), SHG including both strain and band effects is calculated by

$$I^{2\omega}_{\mathrm{perturb}} \propto |O'_{\mathrm{TPDD}} \cdot O_{\mathrm{Q}}|^2. \tag{5.31}$$

The scalar product in Eq. (5.31) with the components of O'_{TPDD}, d_i and those of O_{Q}, q_j, needs further investigation to work out the theoretical concept. It is given by

$$\begin{pmatrix} d_1 \\ d_2 \\ d_3 \end{pmatrix} \cdot \begin{pmatrix} q_1 \\ q_2 \\ q_3 \end{pmatrix} = d_1 q_1 + d_2 q_2 + d_3 q_3 := a_1 + a_2 + a_3. \tag{5.32}$$

Thus, the SHG intensity, i.e. the square of Eq. (5.32), can be divided into two parts,

$$(a_1 + a_2 + a_3)^2 = \underbrace{(a_1^2 + a_2^2 + a_3^2)}_{I^{2\omega}_{\mathrm{add}}} + \underbrace{2(a_1 a_2 + a_2 a_3 + a_1 a_3)}_{I^{2\omega}_{\mathrm{int}}}. \tag{5.33}$$

The first three terms are insensitive to the relative phases as each component is squared by itself. The second part depends on the relative phases of the three components and their interferences. In general, all components will contribute to SHG. However, if the exciton level splittings induced by the k^2 and strain tensor components exceed the exciton linewidths, the interference term vanishes.

The total (normalized) SHG signal can thus be decomposed in the following way using the scaling parameters a and b, with $a + b = 1$:

$$I^{2\omega}_{\mathrm{SHG}} = a\ I^{2\omega}_{\mathrm{add}} + b\ I^{2\omega}_{\mathrm{int}}. \tag{5.34}$$

The fitting result for the scaling parameters a and b allows to determine the ratios of both contributions.

5.5.3 Modeling

In this section, the results of the simulations for the four crystal directions studied experimentally on the yellow 1S exciton resonance are presented, considering first the directions along which SHG is nominally forbidden before turning to the SHG-allowed cases.

SHG for $\mathbf{k}^{\omega} \parallel$ [001] The first crystal direction, which is of highest symmetry of the four directions investigated here, is $\mathbf{k}^{\omega} \parallel [001]$. For this crystal orientation the exciton components are oriented along

$$\mathbf{z} = \begin{pmatrix} 0 \\ 0 \\ 1 \end{pmatrix}\ ,\ \mathbf{x} = \begin{pmatrix} 1 \\ 0 \\ 0 \end{pmatrix}\ ,\ \mathbf{y} = \begin{pmatrix} 0 \\ 1 \\ 0 \end{pmatrix}. \tag{5.35}$$

The polarization of the ingoing photons is as follows:

$$\mathbf{E}^{\omega} = \begin{pmatrix} \cos\psi \\ \sin\psi \\ 0 \end{pmatrix}. \tag{5.36}$$

The two-photon operator according to Ref. [33] is given by

$$O_{\mathrm{TPDD}}(\mathbf{E}^{\omega}) = \frac{1}{\sqrt{2}} \begin{pmatrix} 0 \\ 0 \\ \sin(2\psi) \end{pmatrix}. \tag{5.37}$$

Subsequent emission by the quadrupole operator $\mathrm{O_Q}$, Eq. (5.38), is only possible from the $\mathbf{x}$ and $\mathbf{y}$ components of the exciton.

$$O_{\mathrm{Q}}(\mathbf{k}^{2\omega},\mathbf{E}^{2\omega}) = \frac{1}{\sqrt{2}} \begin{pmatrix} \sin\varphi \\ \cos\varphi \\ 0 \end{pmatrix}. \tag{5.38}$$

Because both operators [Eqs. (5.37) and (5.38)] address different exciton components, no SHG is expected along this high symmetry direction according to Eq. (5.24) in the unstrained crystal.

If only the k^2 terms [Eqs. (5.25) and (5.26)] are considered, the J_3 matrix partially lifts the exciton degeneracy. The two transverse exciton components remain degenerate and are split from the longitudinal component [51, 58]. The J_5 matrix vanishes for the $\mathbf{k}^{\omega} \parallel [001]$ orientation so that it does not lead to state mixing required for SHG.

Finally, it is accounted for the influence of strain. Applying the matrix S [Eq. (5.29)] to the excitation operator O_{TPDD}, it is transformed into O'_{TPDD} [Eq. (5.30)] with the components,

$$\begin{aligned} x' &= \delta_5 \epsilon_{xz} \cdot z, \\ y' &= \delta_5 \epsilon_{yz} \cdot z, \\ z' &= (2\Delta_3 + \delta_3 \epsilon_z) \cdot z. \end{aligned} \tag{5.39}$$

Now, SHG becomes obviously allowed as the only component z that can be excited by two photons is coupled by strain to the components x' and y' from which quadrupole emission is possible. Through measuring the SHG, one may assess the shear strain components ϵ_{xz} and ϵ_{yz}, while other strain components remain unknown.

In Fig. 5.12, measurements on two samples (#34 and #33) with $\mathbf{k}^{\omega} \parallel [001]$ and corresponding fits with Eq. (5.34) to the data are presented. The anisotropy diagram of sample #34 [Fig. 5.12(a)] reveals a fourfold symmetric signal. The fit is performed with the parameter values given in Table 5.3. Despite the same orientation of sample #33, shown in Fig. 5.12(b), the rotational diagram has a different shape as compared to #34 [Fig. 5.12(a)].

The fits indicate that the exciton states have a large splitting compared to their linewidths so that the interference terms are weak as $a \gg b$. The shear strain, which is the origin of this SHG, is much larger for sample #34 than for #33, despite its higher symmetry pattern.

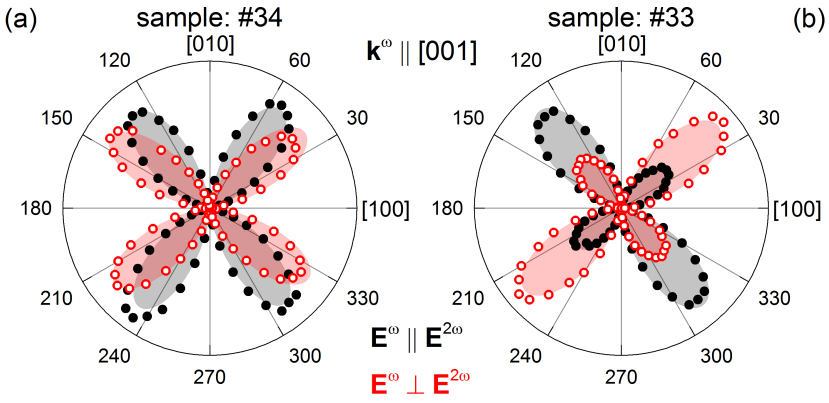

Figure 5.12: Experimental data and simulation of the anisotropies for the 1S exciton ($\mathbf{k}^\omega \parallel [001]$) of (a) sample #34 and (b) sample #33. Filled black and open red dots mark data points of polarization dependences for the geometries $\mathbf{E}^\omega \parallel \mathbf{E}^{2\omega}$ and $\mathbf{E}^\omega \perp \mathbf{E}^{2\omega}$. Grey and red shaded areas show the results of fits to the data.

Table 5.3: Simulation fit parameters (ϵ_i and ϵ_{ij} given in units of $[10^{-6}]$) for samples #34 and #33, according to Eq. (5.34). Entries (-) indicate that this parameter can not be obtained in this $\mathbf{k}^\omega$ direction.

sample	a	b	ϵ_x	ϵ_y	ϵ_z	ϵ_{xy}	ϵ_{xz}	ϵ_{yz}
#34	0.98	0.02	-	-	-	-	23	10
#33	0.73	0.27	-	-	-	-	-2.4	-2.4

SHG for $k^\omega \parallel [\bar{1}10]$ For $\mathbf{k}^\omega \parallel [\bar{1}10]$ the corresponding crystal directions are as follows:

$$\mathbf{z} = \frac{1}{\sqrt{2}}\begin{pmatrix}-1\\1\\0\end{pmatrix}, \quad \mathbf{x} = \begin{pmatrix}0\\0\\1\end{pmatrix}, \quad \mathbf{y} = \frac{1}{\sqrt{2}}\begin{pmatrix}1\\1\\0\end{pmatrix}. \tag{5.40}$$

The polarization of the photons is given by

$$\mathbf{E}^\omega = \frac{1}{\sqrt{2}}\begin{pmatrix}\sin\psi\\ \sin\psi\\ \sqrt{2}\cos\psi\end{pmatrix}. \tag{5.41}$$

Therefore, the operators for excitation and emission are given by

$$O_{\mathrm{TPDD}}(\mathbf{E}^\omega) = \begin{pmatrix}\cos\psi\sin\psi\\ \cos\psi\sin\psi\\ \frac{1}{\sqrt{2}}\sin^2\psi\end{pmatrix}, \tag{5.42}$$

and

$$O_{\mathrm{Q}}(\mathbf{k}^{2\omega},\mathbf{E}^{2\omega}) = \frac{1}{2}\begin{pmatrix} \cos\varphi \\ -\cos\varphi \\ 0 \end{pmatrix}. \tag{5.43}$$

For this $\mathbf{k}^{\omega}$ direction the combined action of the J_3 and J_5 matrices completely lifts the degeneracy of the exciton components. Still, SHG remains impossible without strain as the longitudinal and transversal components remain independent. SHG is induced also here by shear strain resulting in the required mixing. Since emission is not possible through the z' component in which ϵ_z exclusively appears, this strain parameter cannot be evaluated in this geometry. However, the reduced symmetry compared to the previous case gives access to all other strain components.

In Fig. 5.13, measurements on sample #13 with $\mathbf{k}^{\omega} \parallel [\bar{1}10]$ and corresponding fitting with Eq. (5.34) to the experimental data are shown.

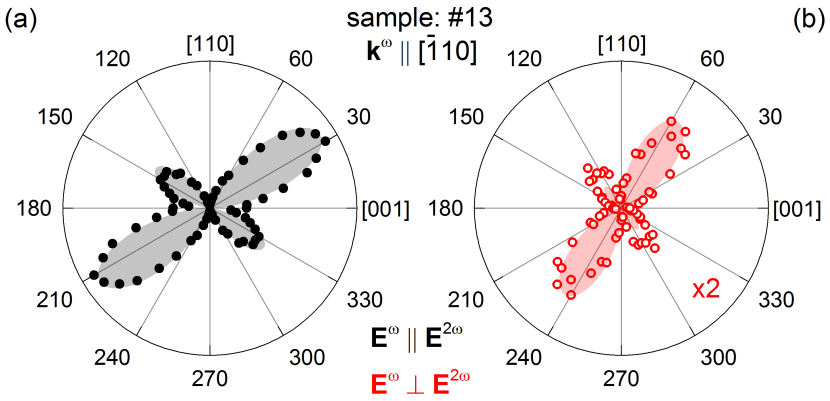

Figure 5.13: Simulation and data of the anisotropies for the 1S exciton ($\mathbf{k}^{\omega} \parallel [\bar{1}10]$) in sample #13. Filled black and open red dots give data points of polarization dependences for (a) the geometry $\mathbf{E}^{\omega} \parallel \mathbf{E}^{2\omega}$ and (b) $\mathbf{E}^{\omega} \perp \mathbf{E}^{2\omega}$. Grey and red shaded areas show the result of the fits to the data.

The results from the fitting procedure for the parameters are summarized in Table 5.4. Remarkably, a and b are of the same order of magnitude so that the interference term $I^{2\omega}_{\mathrm{int}}$ is as important as the one from the individual components $I^{2\omega}_{\mathrm{add}}$. The uniaxial and shear strain parameters are of comparable magnitude, ranging from a few to more than ten 10^{-6}.

Table 5.4: Simulation fit parameters (ϵ_i and ϵ_{ij} given in units of $[10^{-6}]$) for sample #13, according to Eq. (5.34). Entries (-) indicate that this parameter can not be obtained in this $\mathbf{k}^{\omega}$ direction.

sample	a	b	ϵ_x	ϵ_y	ϵ_z	ϵ_{xy}	ϵ_{xz}	ϵ_{yz}
#13	0.46	0.54	-5.9	-1.9	-	14	4.9	2.7

SHG for $\mathbf{k}^\omega \parallel [11\bar{2}]$ For $\mathbf{k}^\omega \parallel [11\bar{2}]$ the corresponding crystal directions are as follows:

$$\mathbf{z} = \frac{1}{\sqrt{6}}\begin{pmatrix}1\\1\\-2\end{pmatrix},\ \mathbf{x} = \frac{1}{\sqrt{2}}\begin{pmatrix}-1\\1\\0\end{pmatrix},\ \mathbf{y} = \frac{1}{\sqrt{3}}\begin{pmatrix}1\\1\\1\end{pmatrix}. \tag{5.44}$$

This direction differs from the previous ones because here SHG is allowed already without strain. Therefore, $I^{2\omega}$ in Eq. (5.24) does not vanish. Still, the orthoexciton states are mixed and shifted by k^2 terms and strain leading to a modified SHG signal. This is adequately described by $I^{2\omega}_{\mathrm{add}}$ and $I^{2\omega}_{\mathrm{int}}$.

The polarization of the photons is given by

$$\mathbf{E}^\omega = \frac{1}{\sqrt{3}}\begin{pmatrix}-\sqrt{\frac{3}{2}}\cos\psi + \sin\psi\\ \sqrt{\frac{3}{2}}\cos\psi + \sin\psi\\ \sin\psi\end{pmatrix}. \tag{5.45}$$

The operators for excitation and emission are as follows:

$$O_{\mathrm{TPDD}}(\mathbf{E}^\omega) = \frac{1}{3}\begin{pmatrix}\sin\psi(\sqrt{3}\cos\psi + \sqrt{2}\sin\psi)\\ \sin\psi(-\sqrt{3}\cos\psi + \sqrt{2}\sin\psi)\\ -(1+5\cos(2\psi))/2\sqrt{2}\end{pmatrix}, \tag{5.46}$$

and

$$O_{\mathrm{Q}}(\mathbf{k}^{2\omega},\mathbf{E}^{2\omega}) = \frac{1}{6}\begin{pmatrix}-\sqrt{6}\cos\varphi - \sin\varphi\\ \sqrt{6}\cos\varphi - \sin\varphi\\ 2\sin\varphi\end{pmatrix}. \tag{5.47}$$

Along this low symmetry direction, both the k^2 and the strain contributions to S mix all three exciton components and modify the SHG. As a consequence, the rotational anisotropy patterns should give insight into all components of the strain tensor. The measured data and the corresponding fits are shown in Fig. 5.14 and compared to the simulation of the expected anisotropies in the absence of local strain. The parameters from the fits are given in Table 5.5.

Table 5.5: Simulation fit parameters (ϵ_i and ϵ_{ij} given in units of $\left[10^{-6}\right]$) for sample #29, according to Eq. (5.34).

sample	a	b	ϵ_x	ϵ_y	ϵ_z	ϵ_{xy}	ϵ_{xz}	ϵ_{yz}
#29	0.87	0.13	2.1	2.0	-1.4	-1.3	0.14	-0.24

For the studied sample, interference effects are of minor relevance due to a rather large exciton level splitting. The strain components are of comparable magnitude with a few parts per 10^{-6}. The comparison to the case of strain-free SHG shows particularly pronounced deviations, namely, six lobes instead of four lobes in the geometry $\mathbf{E}^\omega \parallel \mathbf{E}^{2\omega}$.

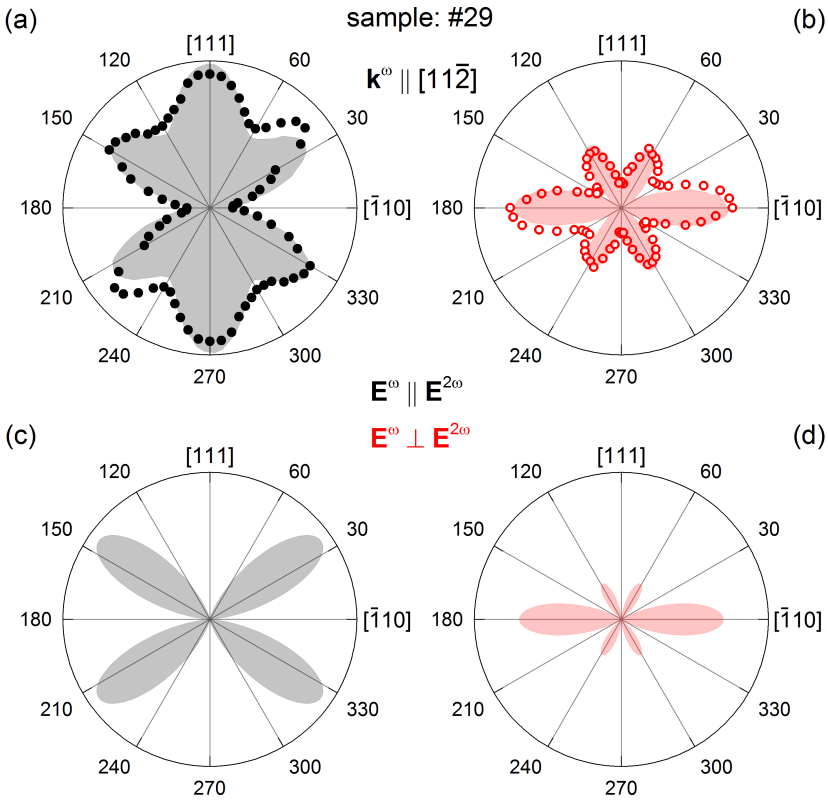

Figure 5.14: Simulation and data of the anisotropies for the 1S exciton in sample #29 ($\mathbf{k}^{\omega} \parallel [11\bar{2}]$). Filled black and open red dots give data points of polarization dependences for (a) the geometry $\mathbf{E}^{\omega} \parallel \mathbf{E}^{2\omega}$ and (b) $\mathbf{E}^{\omega} \perp \mathbf{E}^{2\omega}$. Grey and red shaded areas show the result of the fits to the data. In (c) and (d), the parallel and perpendicular geometries, respectively, are simulated in the absence of local strain, according to Eq. (5.24).

SHG for $\mathbf{k}^{\omega} \parallel [111]$ This k-direction is similar to $\mathbf{k}^{\omega} \parallel [11\bar{2}]$ since all three terms of Eq. (5.34) are allowed. For $\mathbf{k}^{\omega} \parallel [111]$, the corresponding crystal directions are as follows:

$$\mathbf{z} = \frac{1}{\sqrt{3}} \begin{pmatrix} 1 \\ 1 \\ 1 \end{pmatrix}, \quad \mathbf{x} = \frac{1}{\sqrt{6}} \begin{pmatrix} 1 \\ 1 \\ -2 \end{pmatrix}, \quad \mathbf{y} = \frac{1}{\sqrt{2}} \begin{pmatrix} -1 \\ 1 \\ 0 \end{pmatrix}. \tag{5.48}$$

The polarization of the photons is given by

$$\mathbf{E}^{\omega} = \frac{1}{\sqrt{2}} \begin{pmatrix} \frac{1}{\sqrt{3}} \cos\psi - \sin\psi \\ \frac{1}{\sqrt{3}} \cos\psi + \sin\psi \\ -\frac{2}{\sqrt{3}} \cos\psi \end{pmatrix}. \tag{5.49}$$

Therefore, the operators for excitation and emission are as follows:

$$O_{\mathrm{TPDD}}(\mathbf{E}^{\omega}) = \frac{\sqrt{2}}{3}\begin{pmatrix} \cos\psi\left(-\cos\psi - \sqrt{3}\sin\psi\right) \\ \cos\psi\left(-\cos\psi + \sqrt{3}\sin\psi\right) \\ -(1+2\cos(2\psi))/2 \end{pmatrix}, \tag{5.50}$$

and

$$O_{\mathrm{Q}}(\mathbf{k}^{2\omega},\mathbf{E}^{2\omega}) = \frac{1}{6}\begin{pmatrix} -\cos\varphi + \sqrt{3}\sin\varphi \\ -\cos\varphi - \sqrt{3}\sin\varphi \\ 2\cos\varphi \end{pmatrix}. \tag{5.51}$$

Measured data and best fits for a sample #2A with $\mathbf{k}^{\omega} \parallel [111]$ are depicted in Fig. 5.15. In addition, simulated anisotropies in the absence of local strain are shown. Parameters from the fit are listed in Table 5.6. As in sample #29 with $\mathbf{k}^{\omega} \parallel [11\bar{2}]$, the contribution a dominates due to rather large energy-level splitting. The interference is of minor importance. In contrast to the previous case, the local strain does not lead to fundamental changes in the SHG pattern appearance, but influences mostly the intensity values along the different directions.

Table 5.6: Simulation fit parameters (ϵ_i and ϵ_{ij} given in units of $[10^{-6}]$) for sample #2A, according to Eq. (5.34).

sample	a	b	ϵ_x	ϵ_y	ϵ_z	ϵ_{xy}	ϵ_{xz}	ϵ_{yz}
#2A	0.79	0.21	-5.0	-2.0	-1.4	0.02	0.28	0.37

5.5.4 Discussion

After analyzing and fitting the SHG signal in two forbidden and two allowed crystal directions, some details and implications are discussed. By the fitting, the strain tensor components ϵ_i and ϵ_{ij} have been determined. However, along the two high symmetry directions the parameter set is incomplete, whereas for the low symmetry directions all parameters are known. For the case of $\mathbf{k}^{\omega}$ along [111], the full matrix S in Eq. (5.29) can be diagonalized. Its eigenvalues E_i give the energy shifts, induced by the k^2 terms and the strain, relative to the idealized situation with a degenerate orthoexciton state. The new eigenvectors $\boldsymbol{v}_i$ indicate the mixing strength of the original states. The eigenvalues and eigenvectors for every sample are summarized in Table 5.7. From these data, one can, in particular, reassess the importance of the interference term based on the magnitude of the exciton level splitting compared to the 1S linewidth, which, so far, was concluded indirectly only through the relative magnitude of a and b but now can be quantified directly.

Despite the incomplete parameters' set, the case $\mathbf{k}^{\omega} \parallel [001]$ for samples #34 and #33 is considered for illustration, even though for these two samples the unknown strain components might influence the energy splitting and level mixing. As discussed, $\boldsymbol{v}_1$ and

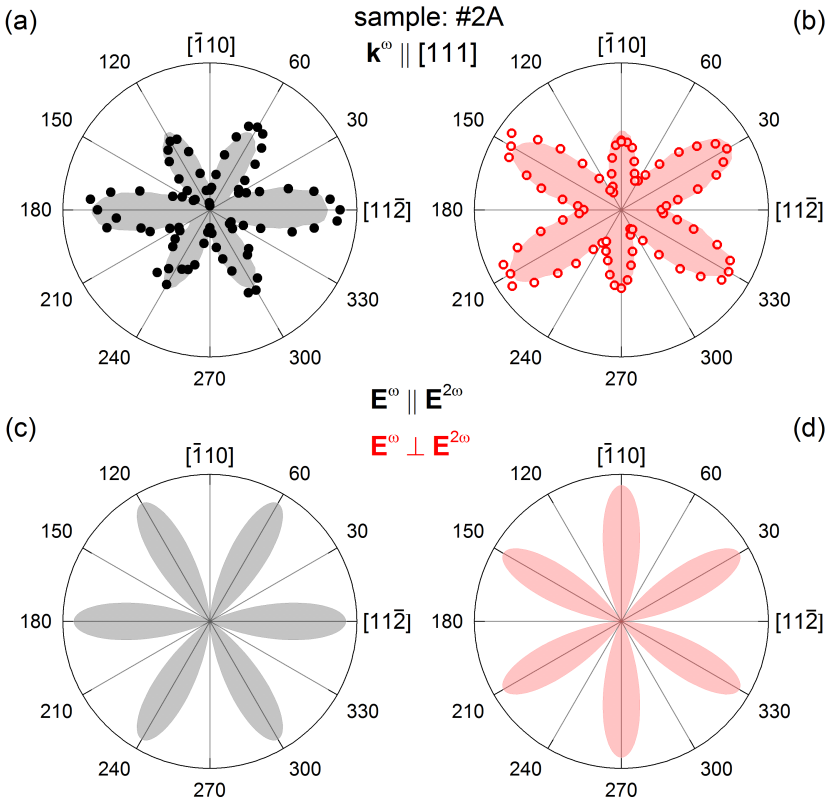

Figure 5.15: Simulation and data of the anisotropies for the 1S exciton in sample #2A ($\mathbf{k}^{\omega} \parallel [111]$). Filled black and open red dots indicate data points of polarization dependences for (a) the geometry $\mathbf{E}^{\omega} \parallel \mathbf{E}^{2\omega}$ and (b) $\mathbf{E}^{\omega} \perp \mathbf{E}^{2\omega}$. Grey and red shaded areas show the result of the fits to the data. In (c) and (d), the parallel and perpendicular geometries, respectively, are simulated in the absence of local strain, according to Eq. (5.24).

$\boldsymbol{v}_2$ with their admixture of $\mathbf{z}$ are excited by two photons through this component and emit by their components $\mathbf{x}$ and $\mathbf{y}$. Eigenvector $\boldsymbol{v}_3$ is not involved in the SHG generation. The energy splitting between $\boldsymbol{v}_1$ and $\boldsymbol{v}_2$ is of importance regarding their degree of interference. According to the eigenvalues E_1 and E_2 for sample #34 (Table 5.7), the splitting is 10 μeV. With the 1S linewidth of 1 μeV [51], it is obvious that both states are sufficiently split in energy to neglect interference. This is supported by the fitting result $a = 0.98$, showing the large contribution of $I^{2\omega}_{\mathrm{add}}$. In the case of sample #33, the degree of mixing between $\mathbf{z}$ and the other two components is smaller, but still $\boldsymbol{v}_1$ and $\boldsymbol{v}_2$ contain an admixture of $\mathbf{z}$. The splitting of these two eigenstates E_1 and E_2, is 4.5 μeV so that interference may still play some role. The ratio of a and b suggests that one quarter of the SHG signal originates from $I^{2\omega}_{\mathrm{int}}$.

For $\mathbf{k}^{\omega} \parallel [\bar{1}10]$, sample #13, the new eigenvectors $\boldsymbol{v}_1$ and $\boldsymbol{v}_3$ have an admixture of $\mathbf{z}$ that allows for quadrupole emission. According to the fit, these are split in energy by

Table 5.7: Eigenenergies E_i given in units of (μeV) and eigenvectors $\boldsymbol{v}_i$ deduced from the fitting for all samples under investigation.

$\mathbf{k}^\omega \parallel [...]$	[001]		$[\bar{1}10]$	$[11\bar{2}]$	[111]
sample	#34	#33	#13	#29	#2A
E_1	-5.8	-3.0	2.8	3.8	-7.3
E_2	4.4	1.5	-1.3	-3.1	2.1
E_3	1.5	1.5	0.72	2.0	-1.1
$\boldsymbol{v}_1$	$\begin{pmatrix}0.24\\0.04\\0.72\end{pmatrix}$	$\begin{pmatrix}0.01\\0.01\\0.98\end{pmatrix}$	$\begin{pmatrix}0.45\\0.20\\0.35\end{pmatrix}$	$\begin{pmatrix}0.51\\0.49\\0.00\end{pmatrix}$	$\begin{pmatrix}0.96\\0.03\\0.01\end{pmatrix}$
$\boldsymbol{v}_2$	$\begin{pmatrix}0.61\\0.11\\0.28\end{pmatrix}$	$\begin{pmatrix}0.50\\0.48\\0.02\end{pmatrix}$	$\begin{pmatrix}0.34\\0.66\\0.00\end{pmatrix}$	$\begin{pmatrix}0.01\\0.03\\0.96\end{pmatrix}$	$\begin{pmatrix}0.03\\0.49\\0.48\end{pmatrix}$
$\boldsymbol{v}_3$	$\begin{pmatrix}0.15\\0.85\\0.00\end{pmatrix}$	$\begin{pmatrix}0.49\\0.51\\0.00\end{pmatrix}$	$\begin{pmatrix}0.21\\0.14\\0.65\end{pmatrix}$	$\begin{pmatrix}0.48\\0.48\\0.04\end{pmatrix}$	$\begin{pmatrix}0.01\\0.48\\0.51\end{pmatrix}$

2.1 μeV only so that the SHG signal shows almost equal contributions from $I^{2\omega}_{\text{add}}$ and $I^{2\omega}_{\text{int}}$.

For the SHG allowed $\mathbf{k}^\omega$ directions $[11\bar{2}]$ and [111], the situation is more intricate. The k^2 and strain terms lead to new eigenvectors all of which resemble admixtures of all three components. In both directions, therefore, all three exciton components can be excited by two photons and can emit by a quadrupole order photon. Therefore, the SHG contributions to $I^{2\omega}_{\text{add}}$ and $I^{2\omega}_{\text{int}}$ can not be identified as clearly as for the a priori SHG forbidden directions.

However, more insight can be achieved from the energy splittings. As an example, sample #2A is discussed with $\mathbf{k}^\omega \parallel [111]$ for which all strain tensor components ϵ_i and ϵ_{ij} are known from the fit to the rotational anisotropies so that the diagonalization of matrix S delivers the complete information. The relative splittings are about 9 μeV between the two states 1 and 2, and 6 μeV between states 1 and 3, so that the corresponding interferences can be neglected, whereas the one between state 2 and 3 (3.2 μeV) is of importance.

Knowing all contributions to the k^2 and strain terms in the matrix S in this case, one can also separate them by hand in order to understand their influence on the exciton level splitting. In Fig. 5.16, calculations for splitting by the k^2 term alone are shown, by the strain term alone and by including both factors. From this pattern, it becomes clear that for this sample the strain being of the order of 10^{-6} is dominating the k^2 terms which are of the order of a μeV. Deformation potential values propose that strain components have to be below 10^{-6} to lead to comparable or smaller energy-level shifts.

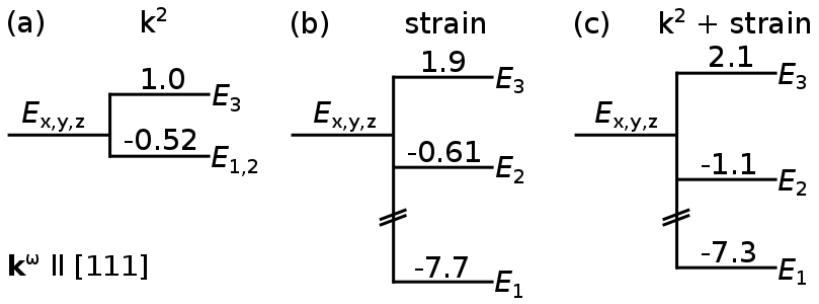

Figure 5.16: Energy splitting [μeV] of the three 1S orthoexciton components for $\mathbf{k}^{\omega} \parallel [111]$ by (a) the k^2 term, (b) the strain term and (c) both the k^2 and strain terms.

For this sample, the strain is a few 10^{-6} and thus is more important than the effect of the k^2 terms. One also sees that the k^2 and strain energy shifts do not simply add up because the total shifts are smaller in magnitude than those by strain alone.

For sample #29, the three exciton states are distributed over an energy range of about 7 μeV. It is slightly less than for sample #2A so that a similar situation concerning the interference of the contributions from the different states is expected. Adjacent states overlap leading to slightly more enhanced interference, whereas the two outermost states are almost independent.

After clarifying the unexpected SHG signals on the 1S resonance, the disappearance of SHG from the higher-lying excitons along the symmetry forbidden directions even though they are also exposed to strain is addressed. The difference between the 1S exciton and excitons of higher principal quantum number n is explained by the ratios of the energy splitting of the components and their lifetimes. A possibility to measure the exciton lifetime in magnetic field which does not depend on a high resolution will be presented in Sec. 5.6. By k^2 and strain, new two-photon dipole and one-photon quadrupole allowed eigenstates are induced. The crucial point is the phase relation between these states. In the moment of femtosecond excitation, no SHG can be observed due to interference of the new eigenstates. After time t, the phase relation between the new eigenstates at $E_i = \hbar\omega_i$ and $E_j = \hbar\omega_j$ has changed by $|\omega_j - \omega_i| \cdot t = \Delta\omega \cdot t$ and allows for detecting SHG. This change in phase is possible only if the lifetime τ of the involved states is much longer than $1/\Delta\omega$. Therefore, the inequality,

$$\tau \cdot \Delta\omega \gg 1 \tag{5.52}$$

applies. From the 1S exciton linewidth of less than 1 μeV [51], its lifetime is calculated to $\tau = 2.1$ ns. The k^2 and strain energy splitting $\Delta\omega$ from the fits are 10 μeV, 4.5 μeV, and 2.1 μeV for samples #34, #33, and #13, respectively. These values are underestimated as certain strain components are unknown for these $\mathbf{k}$ directions. Calculation of the product $\tau \cdot \Delta\omega$ gives: 32, 14 and 7 for the three samples where, at least, the first two can be considered much larger than 1. Excitons of higher n reveal a much broader linewidth. For the 3S resonance a width of 290 μeV [Fig. 5.7(a)] is obtained. This corresponds

to a lifetime of 4.6 ps and values of less than 0.1 for $\tau \cdot \Delta\omega$. Therefore, Eq. (5.52) is not fulfilled. An illustrative picture is that the three orthoexciton components of higher n states are broader than the splitting by k^2 and strain terms. In consequence, they overlap in energy and cannot gain a relative phase between each other. It is important to note that the 1S components need to be treated as overlapping because the spectral resolution of the monochromator is not sufficient. Excitons of higher n can not be resolved due to the fundamental restriction by their broader linewidth.

5.6 Determination of exciton lifetimes by magnetic fields

In the last section, SHG signals for light $\mathbf{k}^{\omega}$ along several crystal directions were observed on the 1S resonance due to local strain. However, this effect was absent on excitons of higher principal quantum number n. This difference was explained by the long lifetime of the 1S exciton in comparison with the states of higher n.

The lifetime of a state can, in general, be determined from its linewidth. If a linewidth is measured with sufficient accuracy, Eq. (4.2) can be used to calculate the lifetime of the state. The 1S exciton was measured in high resolution transmission spectroscopy to have a width below 1 μeV [60], which corresponds to a lifetime of 2.1 ns. A lifetime of about 3 ns is reported from Mysyrowicz *et al.* for phonon-assited excitation of the 1S exciton [61]. Shorter given lifetimes are 850 ps by time-resolved stimulated two-photon emission [62] and 340 ps for time-resolved luminescence [63].

At the current configuration of the LC setup, the maximum resolution of 15 μeV is not sufficient for measuring the natural 1S linewidth. Time-resolved mesurements are possible, but include usage of ps- and fs-OPA. Thus, the idea of lifetime measurement in magnetic field in Faraday-configuration was proposed [64] which will be presented in this section.

5.6.1 Theory

The 1S orthoexciton in Cu_2O is threefold degenerate. So far, the components were described in the linear basis in terms of one longitudinal and two transversal exciton states. If a magnetic field is applied, it is favourable to describe the states in the circular basis by assigning magnetic quantum numbers for the exciton states $M = (0, \pm 1)$. For the experiment, linear polarized femtosecond pulses are shone along the crystal [111]-direction. Therefore, the circular polarizations σ^+ and σ^- are defined as:

$$\sigma^+ = \frac{1}{\sqrt{2}}\left[\cos(\psi + \omega_1 \cdot t) - i\,\sin(\psi + \omega_1 \cdot t)\right], \tag{5.53}$$

$$\sigma^- = \frac{1}{\sqrt{2}}\left[\cos(\psi + \omega_2 \cdot t) + i\,\sin(\psi + \omega_2 \cdot t)\right], \tag{5.54}$$

with ψ, the angle of the polarization of the incoming light, ω_i, the frequencies of the states and time t. The real and imaginary part correspond to polarizations in $[11\bar{2}]$ and $[\bar{1}10]$ direction, respectively.

In magnetic field both circular states are split in energy in accordance with the Zeeman effect,

$$\Delta E_z = \hbar\Delta\omega = \mu_B g B, \tag{5.55}$$

with the Bohr magneton, μ_B and the exciton g-factor. Therefore, knowledge of the Zeeman splitting is a prerequisite for this type of lifetime measurement. The splitting for the 1S is $\Delta E_z(1S) = 48.1\ \mu$eV/T [65]. Still, both states can be excited by the spectrally broad fs-pulses. Upon excitation, i.e. $t = 0$, σ^+ and σ^- are purely polarized in $[11\bar{2}]$ direction, see Fig. 5.17(a). Then they start to precess around the magnetic field axis, Fig. 5.17(b). The different energies of σ^+ and σ^- correspond to different

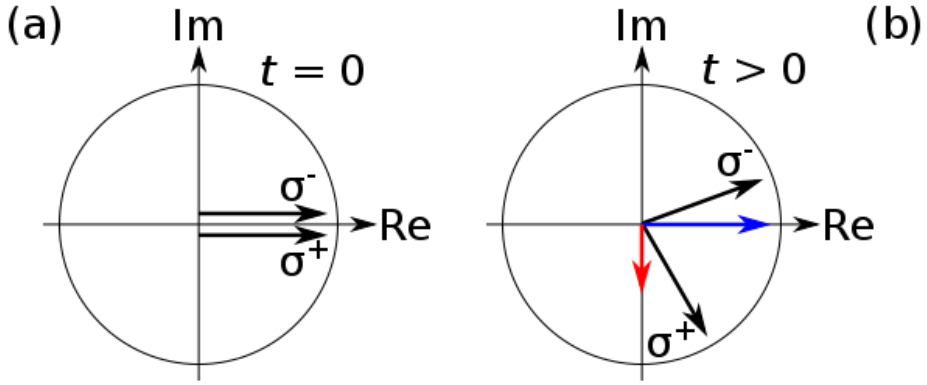

Figure 5.17: (a) At $t = 0$ both circular polarizations are completely real, i.e. polarized along $[11\bar{2}]$. (b) After some time t the circular states precessed according to their frequencies ω_i with different velocity. Blue and red arrows mark the linear polarizations along $[11\bar{2}]$ and $[\bar{1}10]$.

precession velocities. Therefore, a time-dependent phase difference $\Delta\varphi = \Delta\omega t$ builds up. This is responsible for a linear polarization which is turned with respect to the exciting polarization. The maximum phase difference is limited by the exciton lifetime τ and also the splitting by the magnetic field.

The exciton lifetime is obtained by measurement of the SHG signal intensity along $[11\bar{2}]$ and $[\bar{1}10]$ at different magnetic field strengths while the excitation polarization is kept along $[11\bar{2}]$. The intensities along the two directions are modulated in time by the frequency $\Delta\omega$ given by the Zeeman splitting. In addition, they decay exponentially. They are written as the integrals from zero to infinity time:

$$P_{[\bar{1}10]} = c\int \sin^2(\Delta\omega t)e^{-t/\tau}dt = \frac{1}{2}c\tau\frac{x^2}{1+x^2}, \tag{5.56}$$

$$P_{[11\bar{2}]} = c\int \cos^2(\Delta\omega t)e^{-t/\tau}dt = \frac{1}{2}c\tau\frac{2+x^2}{1+x^2}, \tag{5.57}$$

with c being a constant of proportionality, and $x = 2\Delta\omega\tau$. Calculation of the ratio of the intensity along $[\bar{1}10]$ to the sum of both contributions gives the function which can

be fitted to the data:

$$P_{[\bar{1}10]}/(P_{[\bar{1}10]} + P_{[11\bar{2}]}) = \frac{1}{2} \cdot \frac{x^2}{1+x^2}. \tag{5.58}$$

The function increases linear for a small splitting ($x \ll 1$) and has an asymptotic limit of 0.5 for a large Zeeman-Splitting ($x \gg 1$). By fitting Eq. (5.58) to the data, the exciton lifetime is deduced.

5.6.2 Measurements of exciton lifetimes

In Fig. 5.18, the SHG intensity ratios of the 1S, 3S and 4S exciton resonances (black dots) are plotted for magnetic fields in Faraday geometry. Equation (5.58) is fitted to the data (red line). A lifetime of 250 ps is determined for the 1S orthoexciton which is of the order of reported values in Refs. [62, 63]. Still, the signal deviates from the expected behaviour. Despite excitation with light polarized parallel to $[11\bar{2}]$, SHG signal is already present along $[\bar{1}10]$ without magnetic field. At about 0.4 T, the signal in $[\bar{1}10]$ direction is larger than the upper limit of 0.5 and drops at about 0.8 T to 0.45 before reaching the predicted saturation limit of 0.5.

The lifetimes of the 3S and 4S exciton are determined to about 5 ps. Nevertheless, the fits of Eq. (5.58) to the data are not in complete accordance. Although the ratio is zero in absence of magnetic field, it starts to drop below 0.5 for both excitons at 8 T.

In the following, a second approach is presented which accounts for several effects that were neglected so far. As already stated, the components of the 1S exciton are mixed by internal strain. Therefore, the polarization intensity along $[\bar{1}10]$ is not zero in absence of magnetic field. States of higher n are difficult to trace in high magnetic fields as they split and overlap with other emerging resonances. The σ^+ and σ^- states are constructed as

$$\sigma^+ = \frac{1}{\sqrt{2}} \left(\cos\left[(w + \frac{\Delta\omega}{2})t \right] - i \sin\left[(w + \frac{\Delta\omega}{2})t + \frac{s}{2} e^{-\Delta\omega/a} \right] \right), \tag{5.59}$$

$$\sigma^- = \frac{1}{\sqrt{2}} \left(\cos\left[(w - \frac{\Delta\omega}{2})t \right] + i \sin\left[(w - \frac{\Delta\omega}{2})t + \frac{s}{2} e^{-\Delta\omega/a} \right] \right). \tag{5.60}$$

Therein, ω is the frequency of the degenerate 1S exciton at $B = 0$ T and $\Delta\omega$ is the Zeeman splitting of σ^+ and σ^- states. s accounts for the $[\bar{1}10]$ polarization at zero magnetic field due to mixing by internal strain which is reduced and eventually quenched with increasing field. The pace of quenching is controlled by the parameter a. The fit-function is obtained by first calculating the intensities of both polarizations:

$$I_{[11\bar{2}]} = \frac{1}{2} \left[\mathrm{Re}\left(\sigma^+ + \sigma^- \right) \right]^2, \tag{5.61}$$

$$I_{[\bar{1}10]} = \frac{1}{2} \left[\mathrm{Im}\left(\sigma^+ - \sigma^- \right) \right]^2 \tag{5.62}$$

and second by integrating each intensity over $t = 0$ to $t \to \infty$:

$$P_{[11\bar{2}]} = c \int I_{[11\bar{2}]} e^{-t/\tau} dt, \tag{5.63}$$

$$P_{[\bar{1}10]} = c \int I_{[\bar{1}10]} e^{-t/\tau} dt, \tag{5.64}$$

with c, the constant of proportionality. The exact function,

$$P_{[\bar{1}10]}/(P_{[\bar{1}10]} + P_{[11\bar{2}]}), \tag{5.65}$$

is calculated by the software *Mathematica* [66] and fitted to the data, see Fig. 5.18.

Parameters, obtained from this second approach, for the 1S, 3S and 4S exciton are given in Table. 5.8. The parameter τ is not the lifetime of the exciton state, but gives

Table 5.8: Parameters for exciton lifetime determination.

line	ω [1/s]	s [rad]	a [1/s]	τ [s]
1S	0.34	4.85	2.66	9.73
3S	5.46	π	6.22	0.3
4S	5.88	π	2.35	0.16

a qualitative value from which it might be calculated. However, the ratios of the 1S lifetime to the 3S and 4S are in the range of those shown in Fig. 5.18.

Measurements on P-excitons revealed that the exciton lifetime increases with principal qunatum number since the linewidth decreases proportional to n^{-3} [46]. Therefore, the S-exciton lifetime is assumed to increase as well for higher n states.

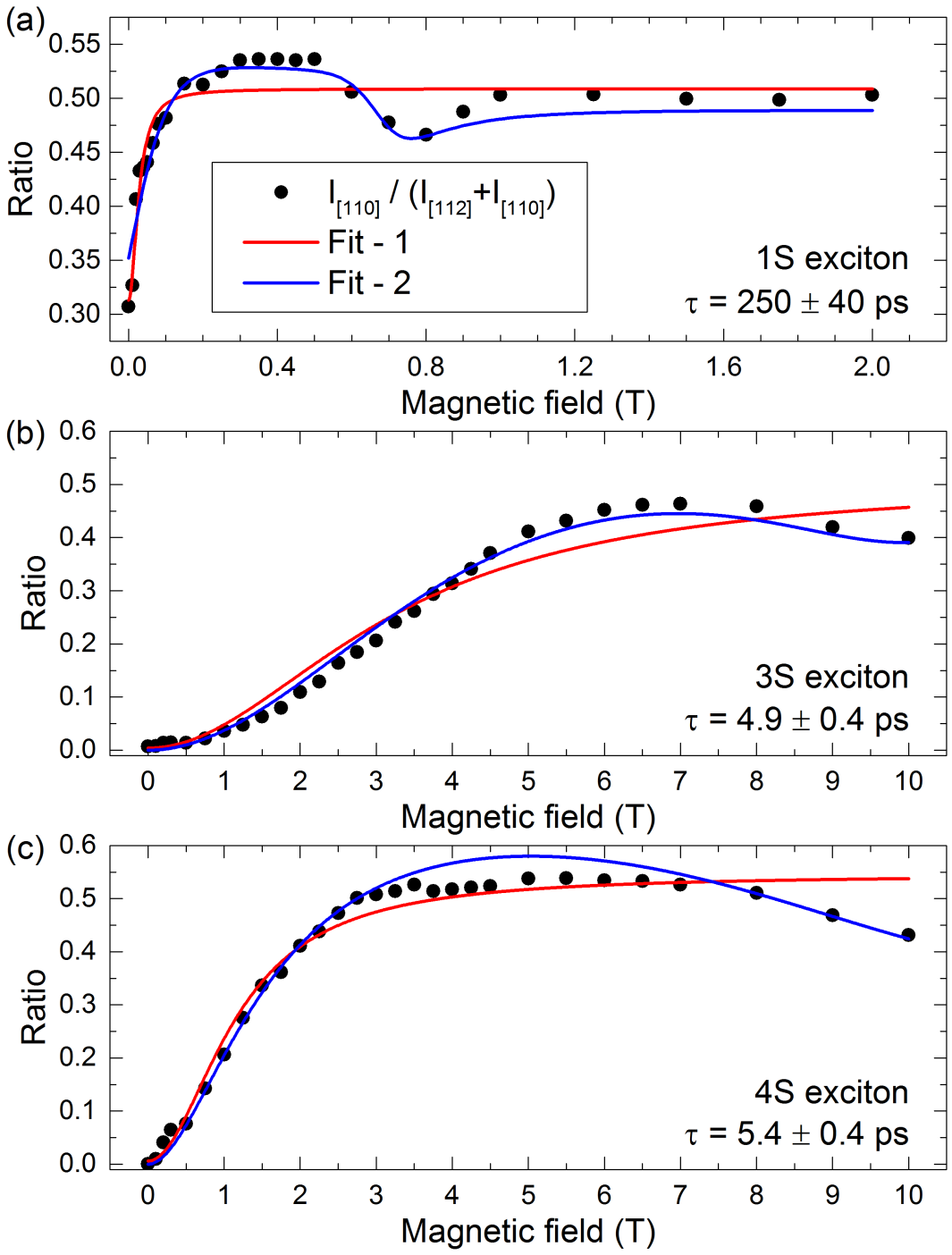

Figure 5.18: Ratios of the (a) 1S, (b) 3S and (c) 4S exciton SHG emission intensity polarized parallel to $[\bar{1}10]$ and the sum of SHG polarized along $[\bar{1}10]$ and $[11\bar{2}]$ (black dots). Best fits to the data of Eq. (5.58) (red line) and Eq. (5.65) (blue line) are shown. Obtained exciton lifetimes from Fit-1 are given.

5.7 Conclusions

One of the main issues of this chapter was to present the use of femtosecond laser pulses with high peak power as a new efficient method for second harmonic generation. Signal is generated across the whole spectral range of the pulses with a good signal-to-noise ratio. Only short integration times are needed in measurements. In contrast to SHG experiments where the ns-, or ps-wavelength is scanned, the resolution in fs-spectra depends on the monochromator and CCD-camera. These need to be further improved in order to obtain the natural linewidth of the 1S exciton resonance.

At higher photon energies, S- and D-excitons up to principal quantum number $n = 9$ are detected in SHG. Also indications of two-photon forbidden P-excitons are present. The analysis of the light-matter interaction mechanisms revealed that S-, as well as, P-excitons are allowed by symmetry due to a quadrupole transition in the emission, or excitation channel, respectively. Tests with the 1m-monochromator and a CCD of smaller pixel size, i.e. a better resolution, yielded no further resonances. A limiting effect might be the excitation of an electron-hole plasma [67] due to the broad spectrum of the fs-pulses. When the photon energy is set for detecting the higher n exciton resonances, the spectrum extends past the band gap and can excite free electrons and holes by two-photon absorption. These could prevent excitons from being generated. Measurements of THG revealed no signal. It might be for even S- and D-excitons that the three-photon excitation with one quadrupole included and quadrupole emission is too weak. Whereas P-excitons are not detectable due to the Γ_3^- phonon background [68] which can be excited with three photons in the P-exciton energy range.

Measurements with circularly polarized light confirmed the theoretical prediction of SHG signal for differently polarized photons for excitons of higher n.

Concerning the 1S line, it is surprising that no polariton shift is observed, despite the large exciton binding energy in Cu_2O. However, the initially expected high oscillator strength is drastically decreased by the quadrupole involved in the emission of the S-exciton. Studies in crystal directions, e.g. [001] and [$\bar{1}$10], which should be SHG forbidden due to symmetry arguments, revealed that the 1S resonance is always observable. Spatially resolved rotational anisotropies confirmed that the otherwise independent longitudinal and transversal components of the orthoexciton are mixed and shifted by internal strain in the samples. The mixing leads to new eigenstates that are two-photon dipole and one-photon quadrupole active at the same time, allowing for SHG. The value of the energy splitting itself is of importance. It determines whether the exciton components can be treated independently in the calculation, or if interferences have to be considered. The anisotropies proved to be particularly valuable. By simulation of their shapes, level splittings of only a few μeV and shear strain components as small as 10^{-6} are determined which is a difficult task in linear optic measurements, too [69]. Despite the strain-free mounting of the samples, residual strain might arise from sample preparation. Excitons of principal quantum number $n \geqslant 2$, behave as predicted by symmetry for the point group O_h. The explanation is that their lifetimes are much shorter than that of the 1S and therefore their linewidths broader. In the end, the ratio of linewidth to line energy splitting, or lifetime to beating frequency of the exciton

components is of importance. The connection between energy splitting and mixing of states is not restricted to local strain. It could be extended to targeted external strain application to the sample as a tool to tailor SHG, as well as other perturbations such as external magnetic and electric fields.

Determination of exciton lifetimes requires usually a pump-probe system, or a setup of high spectral resolution to deduce the lifetime from the linewidth. Here, a model was presented that allows to deduce the lifetime from measurements of linear polarization in magnetic field in Faraday configuration. A first approach delivers lifetimes of the order of previously published data, while it does not account for effects of internal strain at the 1S resonance, which could be quenched at a certain field strength, nor for effects in magnetic field for the higher n excitons. A second approach proposes corrections for these effects, but needs further modifications to extract the exciton lifetimes. However, this method is limited to states which live longer than a few picoseconds. For shorter lifetimes the linewidth becomes broader which would require much stronger magnetic fields to achieve a fast enough precession of the circular polarized states. The question can be asked whether it is the exciton lifetime that is measured here, or if it is the coherence time. To obtain a deeper insight into magnetic effects in SHG spectroscopy, measurements with $\mathbf{k}^{\omega} \parallel [001]$ and magnetic field $\mathbf{B} \parallel [\bar{1}10]$ are performed and analyzed in Ref. [70]. There, two effects, namely the mixing of components within one exciton (Zeeman effect) and mixing of different excitons, e.g. S and P, by the Magneto-Stark effect are presented.

More ideas to apply SHG and fs-, or ps-pulses, to Cu_2O are appearing one after another. To name a few: excitation of the 1S paraexciton by electric quadrupole and magnetic dipole photons; the Γ_3-valence band (as was done in CuCl [71]); investigation of the blue and violet exciton series. All of these ideas will make Cu_2O a truely never ending story.

6 Zinc Selenide

Since the 1960s, ZnSe was subject to comprehensive experiments. Linear reflectivity and absorption measurements were performed by Marple et al. [72, 73]. Further fundamental properties, such as the first observation of a 2P exciton fine structure [74], band masses and g-values [75] were obtained. In order to characterize strained samples, considerable investigations concentrated on deformation potentials and their influence on excitons [76]. Fröhlich et al. applied uniaxial stress to observe 1S exciton shifting and splitting addressed by two-photon absorption measurements [77]. In addition to stress, magnetic fields were used which allowed to investigate the complete set of the 24 states of the 2P exciton in ZnSe [78]. Most recent SHG measurements on ZnSe crystals in applied Voigt and Faraday magnetic fields can be found in Ref. [79]. These measurements are also the motivation for experiments in this thesis. The main finding is the energy difference of the 1S exciton resonance in ZnSe, observed between linear and nonlinear measurements.

ZnSe crystallizes, just like Cu_2O, in cubic symmetry. Still, the zinc blende structure, Fig. 6.1(b), lacks a centre of inversion which makes parity no longer a good quantum number in ZnSe. Thereby, its point group is reduced to T_d ($\bar{4}3m$). In Fig. 6.1(a), the scheme of highest valence bands and lowest conduction band, separated by a band gap of 2.8222 eV [80] is shown. The valence bands, originating from the 4P Se orbitals,

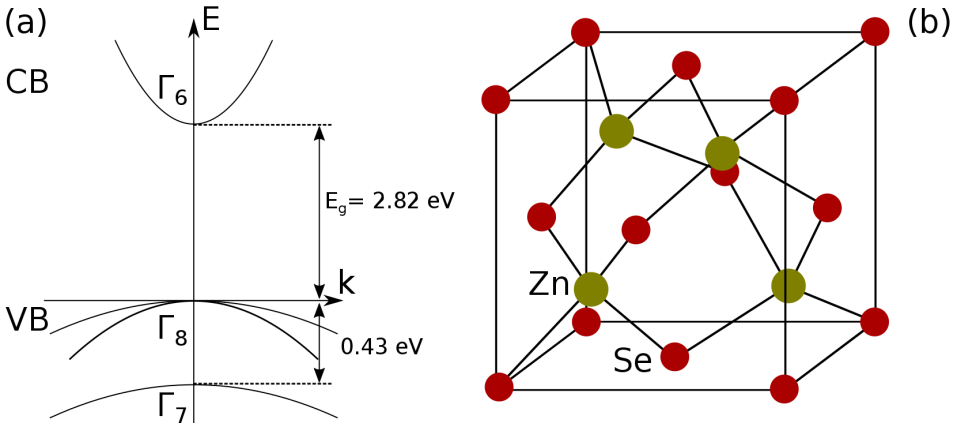

Figure 6.1: (a) Band structure of ZnSe at the Γ-point. (b) ZnSe unit cell.

comprise the fourfold Γ_8 and twofold Γ_7 band. Both are split by the spin-orbit interaction by about 400 meV [81], whereby the Γ_7 band can be neglected for further discussion. The Γ_6 conduction band arises from the 4S Zn orbitals. The 1S exciton binding energy is about 20 meV [82].

6.1 Measurements on the 1S exciton-polariton

In subsequent experiments to Ref. [79], white light reflection, as well as SHG and THG measurements at the 1S resonance were performed which are summarized in Fig. 6.2. The resonance at 2.8037 eV in the white light spectrum is in good agreement with

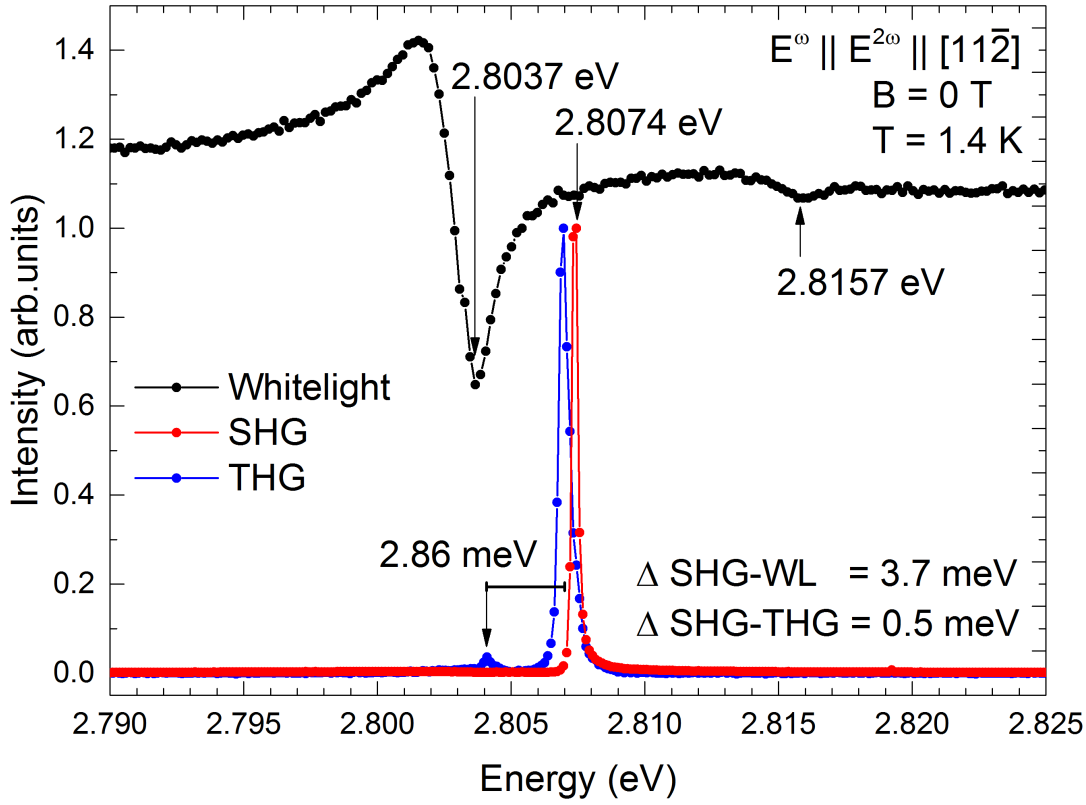

Figure 6.2: Comparison of white light reflection (black), SHG (red) and THG (blue) spectra. The fundamental laser wavelength was set to 1.404 eV (883 nm) and 0.936 eV (1324 nm) for SHG and THG measurement, respectively.

values reported for the 1S exciton [77, 83, 84]. In the SHG spectrum, the 1S resonance is shifted by 3.7 meV to higher energies as compared to the white light reflection. The resonance in the THG spectrum, however, appears 0.5 meV below the SHG peak. Furthermore, a second resonance is present in the THG spectrum 2.86 meV below the 1S resonance. Before the focus is set to the energy difference of the 1S resonance in the white light reflection and harmonic generation spectra, the rotational anisotropies of the 1S resonance in SHG and THG will be addressed.

6.2 1S rotational anisotropies

The SHG and THG rotational anisotropies of the 1S resonance are shown in Fig. 6.3. Whereas the SHG signal shows a sixfold pattern for both configurations, the THG signal is rather isotrop with a small fourfold modulation in the parallel setting and clear fourfold shape in the crossed one.

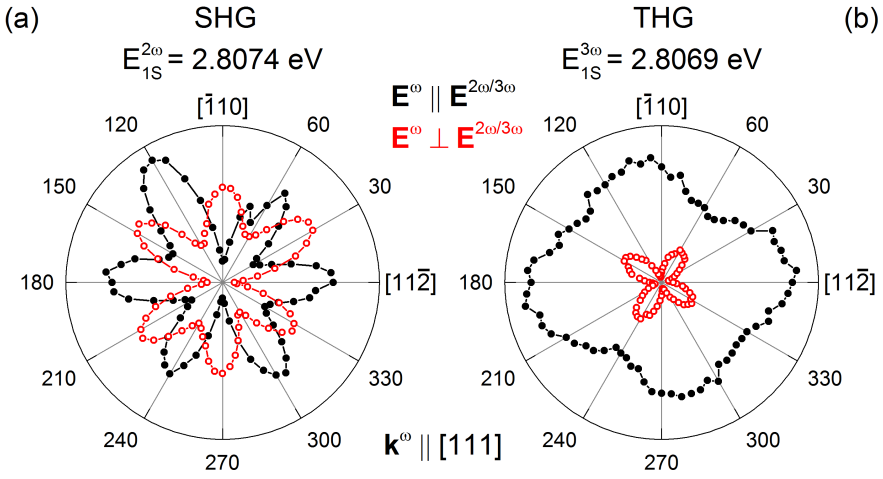

Figure 6.3: Experimental data of the rotational anisotropies for the 1S exciton ($\mathbf{k}^{\omega} \parallel [111]$) for (a) SHG and (b) THG spectroscopy. Filled black and open red dots mark data points of polarization dependences for the geometries $\mathbf{E}^{\omega} \parallel \mathbf{E}^{2\omega}$ and $\mathbf{E}^{\omega} \perp \mathbf{E}^{2\omega}$.

From symmetry analysis, the shapes of the anisotropies are calculated. As parity is not a good quantum number, as opposed to the case in Cu_2O, all Γ_i are given without indication of parity. As presented in Fig. 6.1(a), the S-exciton with a Γ_1 envelope function comprises the symmetries Γ_8 for the hole in the top most valence band and Γ_6 for the electron in the conduction band. According to Eq. (2.29), the total S-exciton symmetry is

$$\Gamma_S = \Gamma_6 \otimes \Gamma_8 \otimes \Gamma_1 = \Gamma_3 \otimes \Gamma_4 \otimes \Gamma_5, \tag{6.1}$$

where Γ_3 is a pure triplet state and cannot be excited optically. The symmetries of photons in dipole order are represented by:

$$\begin{aligned} \text{one photon} &: \Gamma_5, \\ \text{two photons} &: \Gamma_1 \otimes \Gamma_3 \otimes \Gamma_4 (= 0) \otimes \Gamma_5, \\ \text{three photons} &: \Gamma_1 \otimes \Gamma_3 \otimes 2\Gamma_4 \otimes 3\Gamma_5. \end{aligned} \tag{6.2}$$

Note, that, although two photons in dipole order can, in principle, excite a Γ_4 symmetry, calculation gives zero for all three Γ_4 components. Therefore, the symmetries arising from multiplying Γ_4 by the third photon are omitted. The product of polarization (Γ_5^{pol})

and k-vector symmetry (Γ_5^{k}) yield the photon symmetries of electric quadrupole (Γ_i^{eq}) and magnetic dipole order (Γ_i^{md}),

$$\Gamma_5^{\mathrm{pol}} \otimes \Gamma_5^{\mathrm{k}} = \Gamma_1 \otimes \Gamma_3^{\mathrm{eq}} \otimes \Gamma_4^{\mathrm{md}} \otimes \Gamma_5^{\mathrm{eq}}. \tag{6.3}$$

Therefore, the Γ_5 1S exciton is excitable by two and three photons and as well can emit one photon of Γ_5 symmetry in dipole and quadrupole order.

For the 1S exciton in SHG, the same sixfold pattern for parallel and crossed configuration is derived for dipole excitation and emission, as for Cu_2O in Fig. 5.15(c) and (d). Deviations from the sharp shape with zero signal inbetween the maxima might be due to strain in the sample (see Sec. 5.5).

The calculation of the polarization dependence of the THG signal is more intricate than in SHG. In principle, excitation of the 1S exciton is allowed for any combination of three photons in dipole, or quadrupole order. Likewise, one photon in dipole, or quadrupole order can be emitted. The variety of processes is reduced by assuming THG signal containing more than one photon in quadrupole order as negligibly weak. Furthermore, as shown in Fig. 6.4(c), two photons of Γ_5 symmetry in dipole order can excite Γ_1, Γ_3, and Γ_5 intermediate states. From these three states, the final 1S Γ_5 is then realized by applying a third photon of Γ_5 symmetry. Therefore, potentially three channels are present for the excitation process in total.

In the following, three possible schemes of THG shall be considered. Firstly, in a purely dipole process, the 1S exciton is excited by three photons of Γ_5 symmetry and emission is provided by one photon in dipole order. As shown in the lower part of Fig. 6.4(a), the theoretical treatment predicts a fully isotrop shape for the parallel configuration and vanishing intensity for crossed polarizer and analyzer. A much better matching between theory and experiment is reached by including the possibility of emission by photons in dipole and quadrupole order at the same time. Both emissions have to be treated non-interfering. This might indicates that the emission by dipole and quadrupole photons originates from different components of the 1S exciton. In the lower part of Fig. 6.4(b), the fourfold shape of the crossed configuration is reproduced and a modulation of the intensity in parallel setting achieved. Thirdly, the three, by two photons, virtually excited states could come into play in the excitation process, as shown in Fig. 6.4(c). For the simulation, only the quadrupole transition from the intermediate Γ_1 state and the dipole transitions from the intermediate Γ_3 and Γ_5 states were included. The fit result shows even better agreement to the data than in (b). It is noteworthy that the contributions of the different excitation channels are treated independently. The intensity of each channel is determined first, before they are added up. This implies that coherence is of no importance here and the excitations occur independently of each other. The single emitting exciton state is in contrast to the emission in Sec. 5.5 where two or three close lying, mixed states emit coherently.

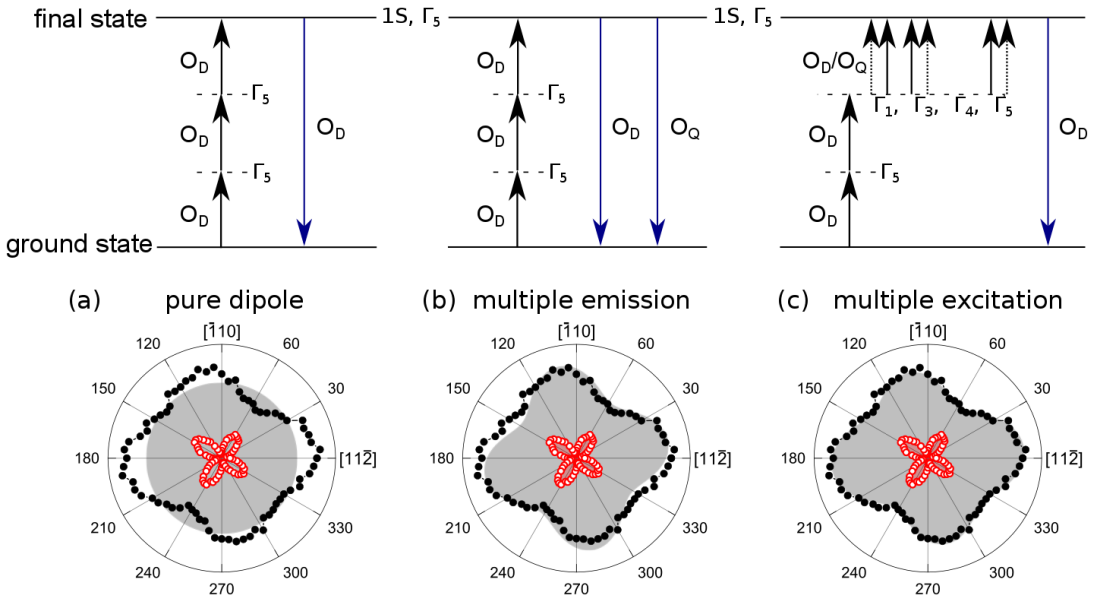

Figure 6.4: Processes (upper row) considered to simulate THG experimental data of the 1S exciton (lower row). (a) Excitation and emission by photons in Γ_5 dipole order symmetry intermediate states only. (b) Excitation by three photons in dipole order and emission by dipole and quadrupole photons. (c) Excitation via different intermediate states by at least two dipoles. Filled black and open red dots mark data points of polarization dependences for the geometries $\mathbf{E}^{\omega} \parallel \mathbf{E}^{2\omega}$ and $\mathbf{E}^{\omega} \perp \mathbf{E}^{2\omega}$. Grey and red shaded areas show the results of the fits to the data.

6.3 Effect of the exciton-polariton dispersion

In this section, a qualitative explanation of the observed differences in energy of the 1S exciton in white light reflection, in SHG and THG, as seen in Fig. 6.2, is given.

A calculation of the ZnSe exciton-polariton dispersion can be found in Ref. [77]. It is shown in Fig. 6.5 together with measured 1S energies from Fig. 6.2, indicated by filled black dots. Along with the polariton-dispersion, the light-dispersions for the fundamental light in SHG and THG measurements are presented. The absolute $\mathbf{k}$-values of the photons are deduced from their energy E by:

$$|\mathbf{k}(E)| = \frac{E[\mathrm{eV}]e \cdot n(E)}{c\hbar}, \tag{6.4}$$

with the index of refraction, $n(E)$, which depends on the photon energy. For the fundamental photon energies in SHG (THG) it is $n(E) = 2.48$ ($= 2.43$) at room temperature [85, 86]. The crossing points of light- and polariton- dispersion are in good agreement with the detected 1S resonances in the experiment. Therefore, the strong light-exciton coupling is responsible for the energetically shifted 1S resonances in SHG and THG spectra. Shifts were also observed in THG spectra in GaAs and CdTe [87]. The second

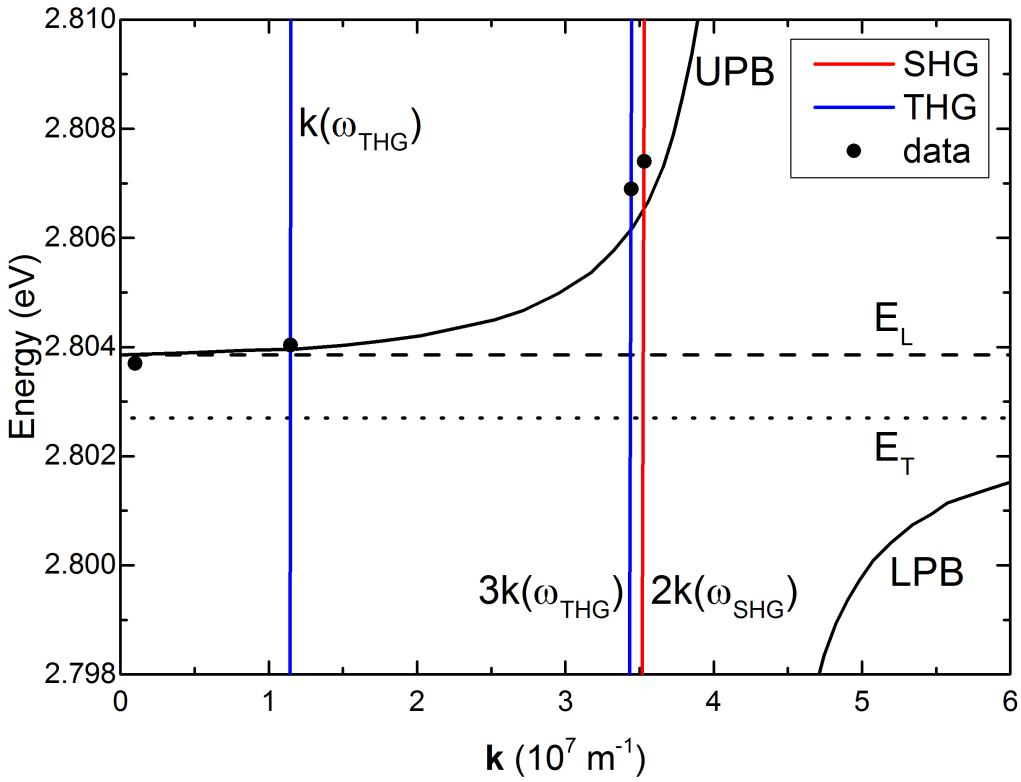

Figure 6.5: Exciton-polariton dispersion for the 1S exciton in ZnSe [77]. Shown are the upper (UPB) and lower polariton branch (LPB) (solid black lines), as well as the dispersion of the longitudinal exciton (LE) (dashed black line). The transversal exciton energy is indicated by the dotted black line. The almost vertical lines represent the dispersion for the fundamental light for SHG (1.4 eV (885.6 nm)) in red and for THG (0.93 eV (1328.9 nm)) in blue. Filled black dots give the 1S energies in Fig. 6.2.

peak at lower energy in the THG spectrum arises from backscattering of fundamental THG light at the rear side of the sample. Therefore, two photons in forward direction and one photon in backward direction excite an exciton at $\mathbf{k}(\omega_{\mathrm{THG}})$. The same is possible in SHG, but the sum **k**-vector is zero. Thus, no SHG emission from such an excitation can be observed. The energy of the 1S exciton dip in the white light reflection spectrum corresponds to the value of the longitudinal exciton where the imaginary part, i.e. absorption, of the dielectric function has a maximum.

Due to the four-fold Γ_8 valence band in ZnSe, additional polariton branches were measured Ref. [88]. There, besides the UPB and LPB, branches for the heavy and light hole exciton-polaritons are reported by two-photon resonant Raman scattering.

6.4 Effect of Voigt magnetic field

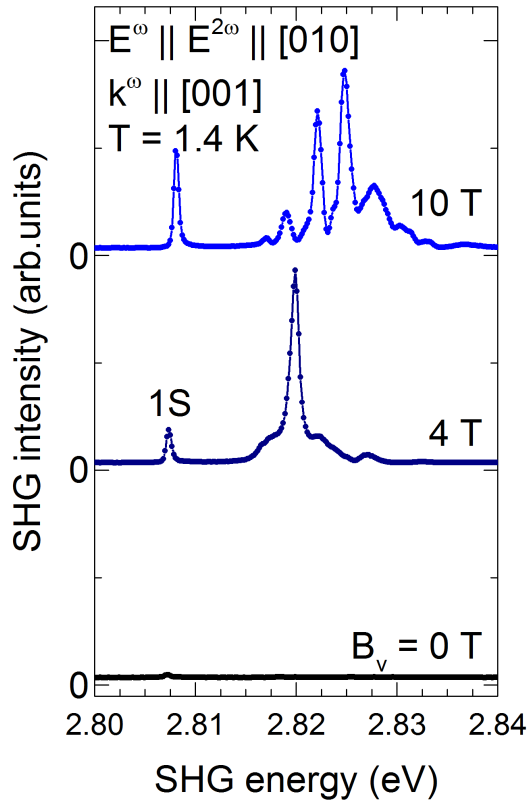

Figure 6.6: Induced SHG by an applied magnetic field in Voigt geometry in the otherwise forbidden $\mathbf{k}^{\omega} \parallel [001]$ crystal direction. Shown are spectra at 0, 4 and 10 T.

The influence of an applied magnetic field on the exciton resonances was studied in [79]. In Fig. 6.6, SHG is induced by the magnetic field in the otherwise symmetry forbidden $\mathbf{k}^{\omega} \parallel [001]$ direction. Exciton components get mixed by the field, just like in the case of strain induced SHG in Sec. 5.5. This particular crystal direction is shown here to emphasize the effect of the magnetic field which is used in the next section with the ZnSe/BeTe heterostructures to obtain SHG signal.

6.5 Conclusions

The observation of different resonance energies of the 1S exciton in whitelight reflection, SHG and THG spectra is explained by the exciton-polariton dispersion. In THG, a second peak at lower energy than the 1S resonance originates from the combination of one backscattered photon from the backside of the crystal and two photons in forward direction.

Rotational anisotropies of the 1S resonance in SHG and THG measurements are simulated and confirmed. Due to the lack of a centre of inversion, it is not necessary to mind the parity of exciton states. Still, the SHG process is expected to contain one quadrupole (probably in the excitation channel), as the THG signal is of comparable intensity, although being a higher order process.

In the case of THG, different intermediate states might contribute to the THG signal. Therefore, the use of independent laser beams could lead to additional information about these states by shifting the intermediate energy or the polarizations.

7 ZnSe/BeTe multiple quantum wells

Since the late 1990s, ZnSe/BeTe heterostructures are investigated by linear optical techniques, e.g. PL, PLE and reflectivity. One main feature of a ZnSe/BeTe-MQW is its type-II band alignment, Fig.7.1(a). It provides energy minima for electrons and holes in the ZnSe and BeTe layers, respectively. The electrons are confined by a conduction band energy offset, $E_{\mathrm{CBO}} = 2.2$ eV, whereas the valence band offset, E_{VBO}, amounts to 0.8 eV. In a 16 nm quantum well, an exciton binding energy of slightly more than 20 meV [82], comparable to bulk ZnSe, and strong oscillator strength were found [89]. Due to the type-II structure, spatially indirect transitions of 2 eV energy can occur in this system. Photoluminescence at this energy undergoes a blue shift at high excitation power [90]. Recombination kinetics in dependence of carrier densities were investigated as well [91]. The interfaces of the ZnSe and BeTe layers are of special interest. They determine the symmetry of the quantum wells and strongly influence the indirect transitions of electrons in the ZnSe and holes in the BeTe layer leading to anisotropic signals [92–94]. However, also direct transitions in the ZnSe layer at 2.8 eV were observed due to the formation of metastable hole states therein [95].

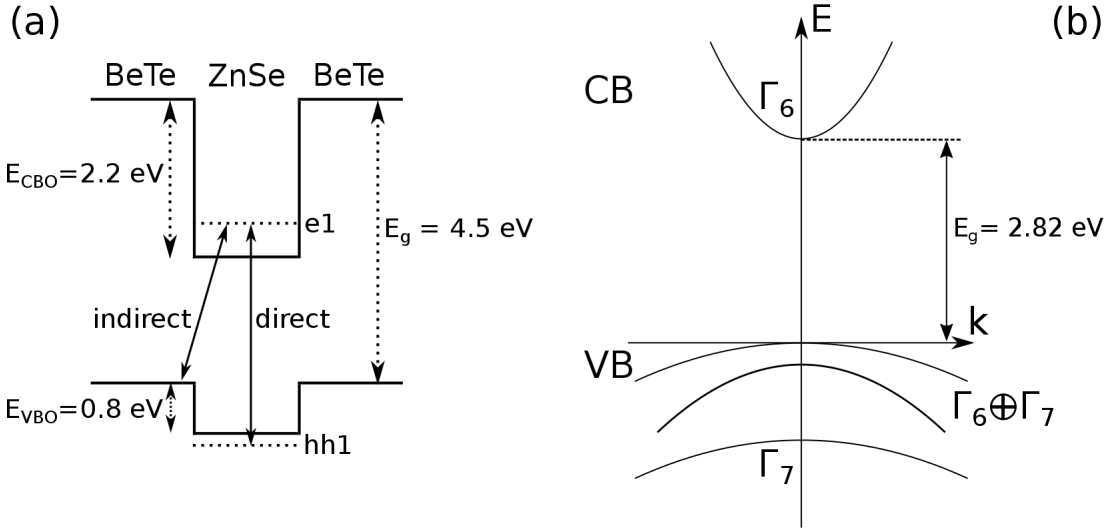

Figure 7.1: (a) Scheme of type-II valence and conduction band alignment and energies [95, 96]. Quantization levels for electron (e1) and heavy hole (hh1) are indicated. (b) Band diagram and irreducible representations of ZnSe in reduced symmetry D_{2d}.

Electrons in the ZnSe conduction band generate a shallow attracting potential for holes in the ZnSe valence band. Therefore, exciton states are stable within the ZnSe layer for low temperatures.

SHG measurements are scarce in the visible range on semiconductor heterostructures. Data shown in this thesis present the first SHG and THG experiments on a ZnSe/BeTe MQW sample that is grown by the molecular beam epitaxy method. It comprises ten periods of 20 nm ZnSe well and 10 nm BeTe barrier (sample: cb1750), grown on a 0.5 mm thick GaAs substrate oriented along the crystal [001]-direction. The direct transitions in the wells are investigated. Therefore, exciton resonances are expected in the energy range of the ZnSe bulk material band gap $E_{\mathrm{g}}^{\mathrm{ZnSe}} = 2.8222$ eV [80]. The band structure and symmetries at the Γ-point of the Brillouin zone are shown in Fig. 7.1(b). Due to the reduced dimension of ZnSe to two-dimensional quantum wells, the point group lowers to a subgroup of the bulk material, T_d ($\bar{4}$3m). In 2D, either the group C_{2v} (mm2), or D_{2d} ($\bar{4}$2m) applies, depending on the well-barrier interfaces [93, 94]. In the present sample, both interfaces are of Zn-Te type, resulting in D_{2d} symmetry. Therefore, the formerly fourfold degenerate Γ_8 valence band, see Fig. 6.1(a), is split into two bands of Γ_6 and Γ_7 symmetry [33].

After a brief introduction to general features of (type-II) quantum wells, measurement results are presented in the following sections. The results are divided into picosecond and femtosecond measurements to show a comparison of both excitations.

7.1 Theory

To start with the description of multiple quantum wells, one word might be in order to distinguish these from superlattices. In a superlattice, the barriers are grown narrow to allow for the wave functions of one well to couple to the adjacent ones. Therefore, an artificial crystal with tunable electron (mini-)bands is created. In contrast, the barriers in a MQW are broad enough to prevent any coupling between the individual wells.

A common and basic effect of quantum well structures is the quantization of valence and conduction band. The dependence of the quantization energy E_{QC} on exciton principal number n, effective electron (hole) mass m_{i} in units of electron mass m_0 and well width L_{w} for the ideal case of infinite confinement potential is given by:

$$E_{\mathrm{QC}} = \frac{\hbar^2}{2m}\left(\frac{n\pi}{L_{\mathrm{w}}}\right)^2 = 0.965\ \frac{n^2}{m_{\mathrm{i}} \cdot L_{\mathrm{w}}^2}\ \mathrm{eV}\cdot\mathrm{nm}^2. \tag{7.1}$$

For an infinite well of 20 nm width, effective bare electron mass of 0.13 [97] and hole mass of 0.89 [98], the quantization energies for the first electron and hole level would be 19 meV and 2.7 meV, respectively. As the ZnSe wells are finite the quantization energy is smaller than in the ideal case [99].

In principle, each combination of a quantized electron and hole level can exhibit an exciton series. Although parity is not a good quantum number in ZnSe, the quantized levels introduce parity selection rules. Due to the parity of the wavefunctions of the quantized states, levels of odd number have even parity and vice versa.

Apart from excitons, it is possible to observe trions in quantum well structures. These are complexes of an exciton which combines with an already existing (resident) electron or hole. Depending on the charge of the additional particle, trions can be

positively (T^+) or negatively (T^-) charged. An excess number of carriers is generated due to the separation of electrons and holes to the ZnSe and BeTe layers.

7.2 Photoluminescence and reflectivity

Before nonlinear spectra are presented, an overview of resonance energies in the ZnSe quantum wells is obtained from linear measurements. The reflectivity and PL spectra are given in Fig. 7.2(a) and (b), respectively. The reflectivity spectrum is recorded by illumination from a halogen lamp in backscattering geometry. Many maxima and minima are present. The arrows and corresponding numbers indicate transition energies from an electron level (first digit) to a hole level (second digit) calculated by A. A. Maksimov [100]. Together with the PL spectrum, more information can be extracted from these

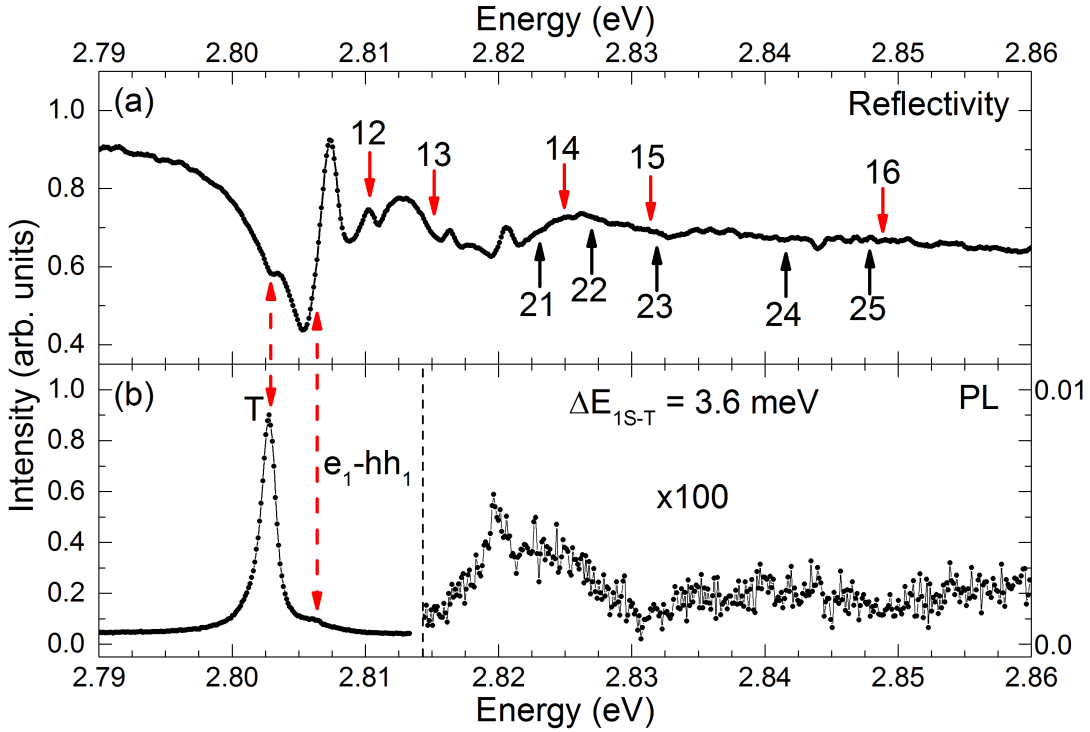

Figure 7.2: Comparison of: (a) whitelight reflectivity spectrum, and (b) photoluminescence (PL) spectrum of the sample after excitation at 3.06 eV with a cw laser. Red and black arrows indicate calculated energies of the 1S transitions between the e_1 and e_2 levels to the different heavy hole levels, respectively. The numbers xy denote the level of the electron and hole for each transistion. Note that the high energy part of the PL spectrum is magnified by a factor of 100.

measurements. The PL spectrum was detected upon excitation by a continuous wave laser at 3.06 eV (405 nm) and 7 W/cm^2. Similar to [89], the main PL peak denotes the trion state at $E_T = 2.8028$ eV. In the high energy shoulder of the trion, the 1S exciton

resonance of first electron and hole level is observed at $E_{1S} = 2.8064$ eV. This value is smaller than expected from the electron and hole quantization energies. The sum of 1S bulk energy and quantum confinement in infinite wells would amount to 2.8254 eV.

7.3 SHG with ps-pulses

This section is concerned with picosecond pulse excitation SHG measurements. In Fig. 7.3, three spectra in 0, 5 and 10 T in Voigt geometry are compared.

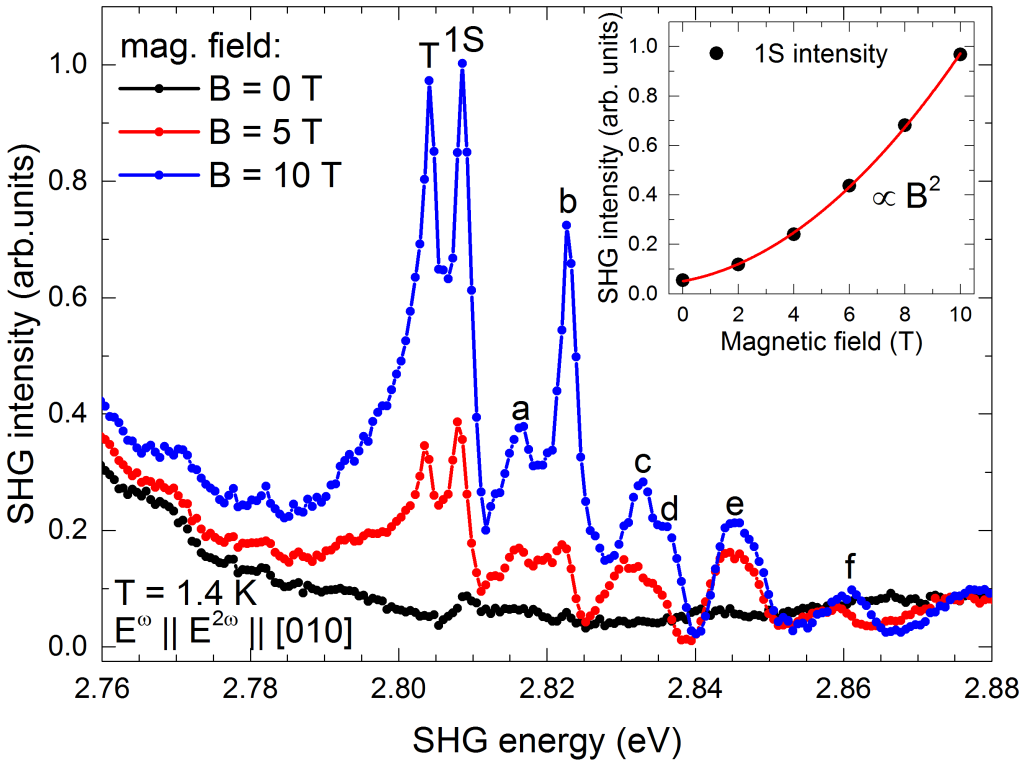

Figure 7.3: SHG spectra in the absence (black) and in magnetic field of 5 and 10 T (red and blue). Resonances are labeled by T: trion, 1S: energetically lowest 1S exciton transition, and a - f for further resonances. The inset shows the 1S exciton SHG intensity as a function of magnetic field. The solid line is the best fit to the data (black dots) with $I^{2\omega} \propto B^2$.

In absence of magnetic field, only a low intense broad line emerges slightly above the 1S peak in PL. Towards the lower energy side of the spectrum, the SHG signal increases. This behaviour might be attributed to well/barrier interface recombination of separated carriers. With increasing field, several sharp lines are induced, including the trion and 1S resonance at 2.8041 eV and 2.8086 eV, shifted to slightly higher energy.

Further lines are labelled by letters a – f. The 1S intensity in dependence of magnetic field is plotted in the inset. A square function is fitted to the data and shows very good agreement, indicating that SHG becomes allowed by magnetic field in accordance with Eq. (2.9), extended by B:

$$I^{2\omega} \propto (\mathbf{P}_i^{2\omega})^2 = |\epsilon_0 \chi_{ijkl}^{(2)} \mathbf{E}_j^{\omega} \mathbf{E}_k^{\omega} \mathbf{B}_l|^2. \tag{7.2}$$

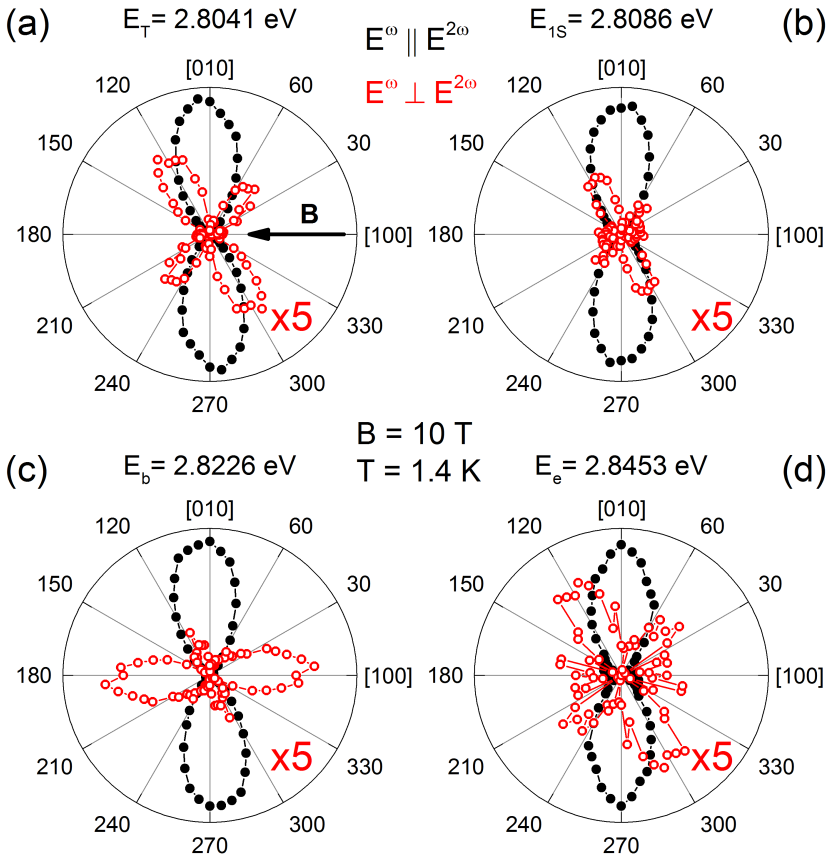

Figure 7.4: SHG rotational anisotropies of (a) the trion, (b) the 1S exciton, (c) resonance b and (d) resonance e as assigned in Fig. 7.3. Solid (black) and open (red) circles represent data for the $\mathbf{E}^{\omega} \parallel \mathbf{E}^{2\omega}$ and $\mathbf{E}^{\omega} \perp \mathbf{E}^{2\omega}$ (magnified by factor 5) configurations, respectively. The direction of the Voigt magnetic field $\mathbf{B}$ is indicated in (a).

Rotational diagrams in a magnetic field of 10 T of the trion and 1S exciton resonance, as well as of the resonances denoted by b and e are measured and presented in Fig. 7.4. The SHG signal reveals the same polarization angular dependence for $\mathbf{E}^{\omega} \parallel \mathbf{E}^{2\omega}$ for these four resonances. For $\mathbf{E}^{\omega} \perp \mathbf{E}^{2\omega}$, the signal is by a factor 5 to 10 less intense and shows different shapes. The rotational anisotropies will be analyzed in detail in Sec. 7.5.

7.4 THG with ps-pulses

THG spectra in the absence and in 10 T magnetic field are shown in Fig. 7.5(b). Signal is already present without magnetic field due to different symmetry selection rules in THG, as compared to SHG. The 1S exciton resonance is located at the same energy as in SHG and has doubled its intensity at 10 T magnetic field. The trion resonance is much broader than in SHG and increases by a factor of four in magnetic field. In

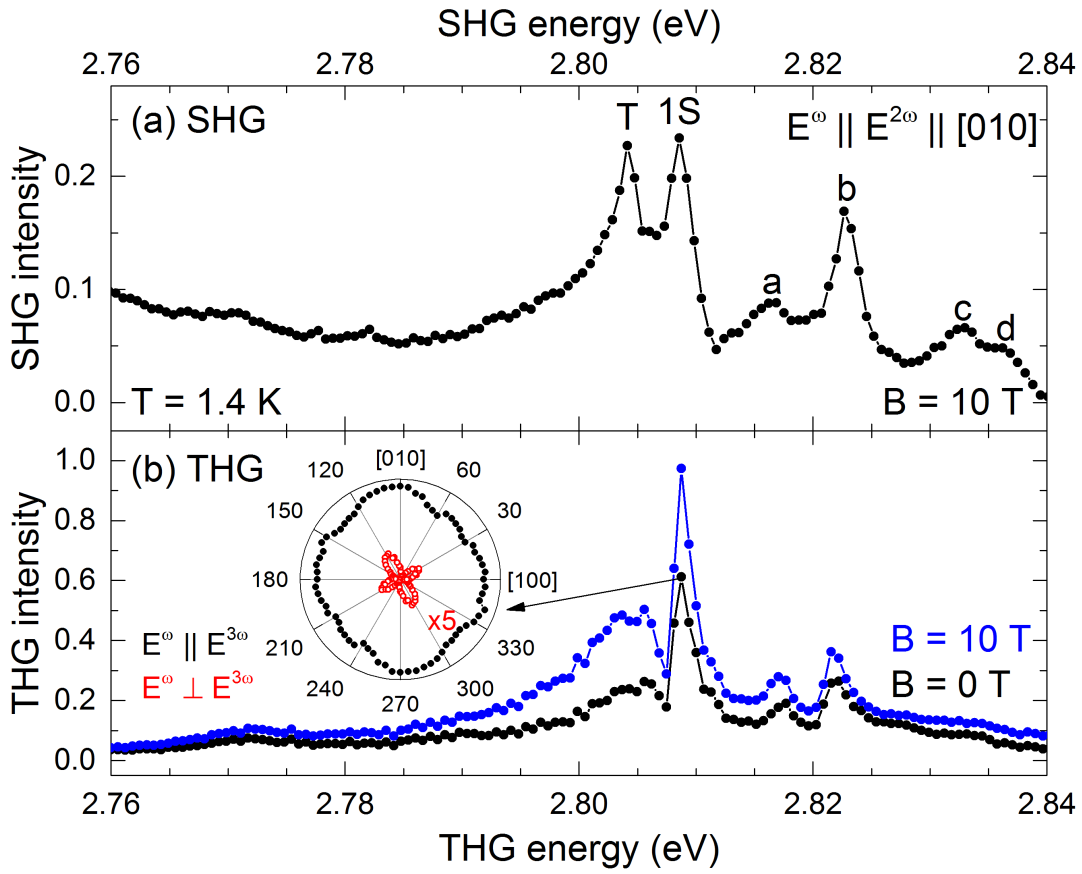

Figure 7.5: Comparison of (a) SHG spectrum in magnetic field of 10 T and (b) THG spectra in the absence (black) and in 10 T magnetic field (blue). The inset in panel (b) shows the rotational anisotropy of the 1S resonance in the absence of magnetic field for $\mathbf{E}^{\omega} \parallel \mathbf{E}^{2\omega}$, filled black dots, and $\mathbf{E}^{\omega} \perp \mathbf{E}^{2\omega}$, open red dots, configuration.

contrast to the SHG spectrum [Fig. 7.5(a)], the THG intensity does not increase below 2.78 eV. The SHG and THG spectra are measured with the same average laser power and normalized to the most intense peak value. Therefore, although THG is a one order higher nonlinear process, its signal is about 5 times more intense than SHG. This hints at a purely dipole mediated THG process in contrast to quadrupole dominated SHG.

In Fig. 7.6, further rotational anisotropies of the THG signal of the trion, a and b resonances are given. The polarization dependences for $\mathbf{E}^{\omega} \parallel \mathbf{E}^{2\omega}$ show a fourfold modulation with an isotropic background. Anisotropies for $\mathbf{E}^{\omega} \perp \mathbf{E}^{2\omega}$ are by a factor of 10 weaker and reveal fourfold shape.

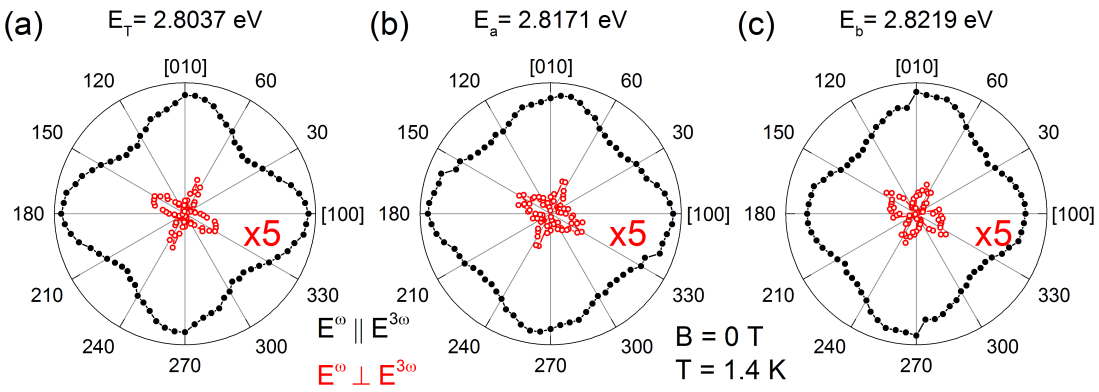

Figure 7.6: THG rotational anisotropies of (a) the trion, (b) resonance a and (c) resonance b, as assigned in Fig. 7.5. Filled black and open red circles represent data for the $\mathbf{E}^{\omega} \parallel \mathbf{E}^{2\omega}$ and $\mathbf{E}^{\omega} \perp \mathbf{E}^{2\omega}$ (magnified by factor 5) configurations, respectively.

The increase in signal intensity with increasing magnetic field, as shown in Fig. 7.5(b), is accompanied by slight changes in the anisotropies of the 1S exciton and resonance b. In Fig. 7.7, the anisotropies for $B = 0$ T and $B = 10$ T are compared. In the next section, the THG rotational anisotropies will be analyzed in detail.

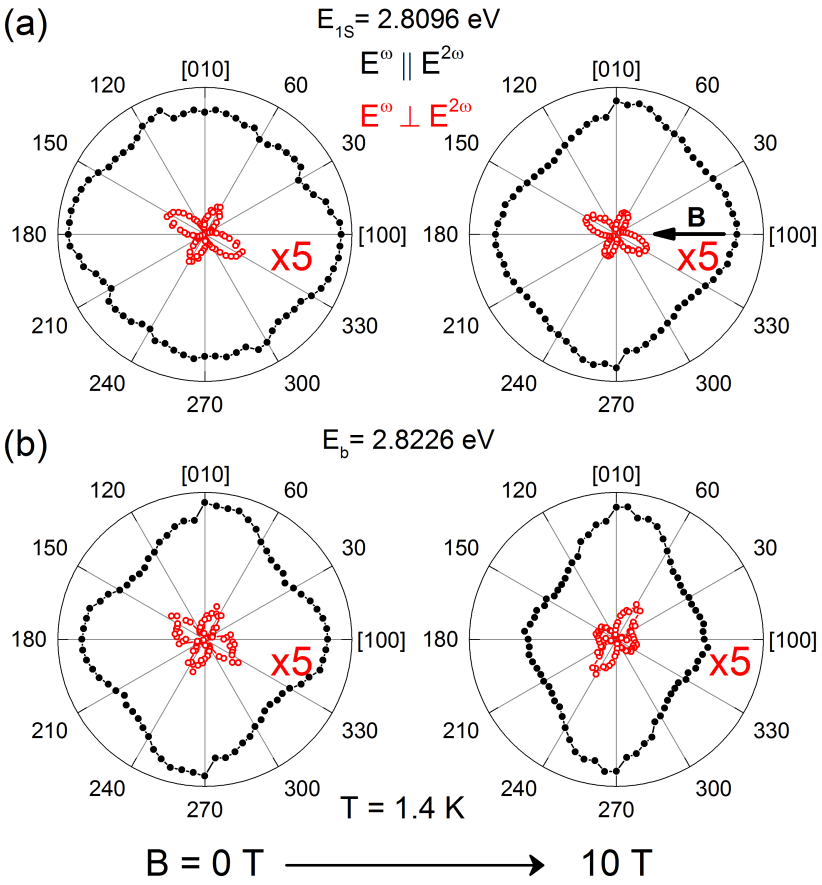

Figure 7.7: THG rotational anisotropies of (a) the 1S exciton and (b) the resonance b, as assigned in Fig. 7.5, in the absence of magnetic field (left side) and in 10 T Voigt field (right side). The direction of the magnetic field is given in the right hand side of (a). Filled black and open red circles represent data for the $\mathbf{E}^{\omega} \parallel \mathbf{E}^{2\omega}$ and $\mathbf{E}^{\omega} \perp \mathbf{E}^{2\omega}$ (magnified by factor 5) configurations, respectively.

7.5 Symmetry analysis

The SHG and THG anisotropy pattern, shown in the last section, will be analyzed and simulated. To do so, a further reduction of the quantum well symmetry by internal electric fields is required, together with the magneto-Stark effect induced by the applied magnetic field.

7.5.1 SHG selection rules

The band and exciton structure in ZnSe/BeTe MQW can become arbitrarily difficult. The formerly degenerate valence bands at the Γ-point are split in energy and build the heavy-hole (hh) and light-hole (lh) bands. Due to spatial confinement, each valence and

conduction band is quantized into sub-bands which are labelled by additional quantum numbers n_v and n_c, respectively.

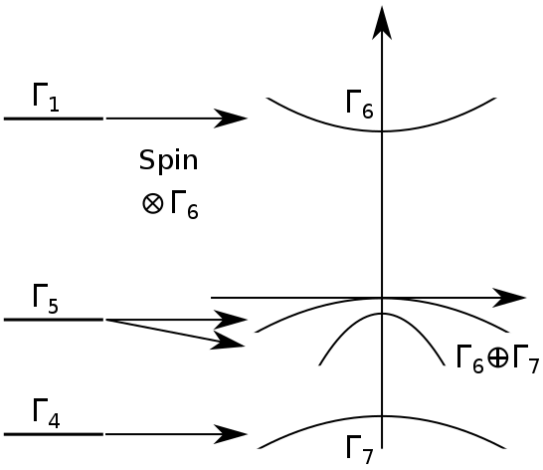

Figure 7.8: Symmetries of bands in a crystal of D_{2d} symmetry without and with spin.

In principle, for each of the sub-bands an entire exciton series with S-, P-states, etc., is present. Furthermore, the quantum well structure lowers the bulk symmetry of ZnSe (T_d) to D_{2d}. Hereby, the degeneracy of the upper valence band in T_d at the Γ-point is lifted, see Fig. 7.8. In a first step, the symmetries of S- and P-excitons, containing either a hole from a Γ_6 (S_6), or Γ_7 (S_7) valence band whose energetic order and splitting is not known, are calculated. Exciton states containing a hole from the split-off band are omitted due to the band's lower energy. The S-exciton states are represented by the symmetries given in Eqs. (7.3) and (7.4). Pure triplet states, which can not be excited optically, are plotted in red.

$$S_6 : \Gamma_6 \otimes \Gamma_6 \otimes \Gamma_1 = \Gamma_1 \oplus \Gamma_2 \oplus \Gamma_5, \tag{7.3}$$
$$S_7 : \Gamma_6 \otimes \Gamma_7 \otimes \Gamma_1 = \Gamma_3 \oplus \Gamma_4 \oplus \Gamma_5. \tag{7.4}$$

P-excitons from the singlet S-excitons, multiplied by the P_{xy} (Γ_5) and P_z (Γ_4) envelope, have the symmetries

$$\begin{aligned} P_{6xy} : \Gamma_5 \otimes \Gamma_5 &= \Gamma_1 \oplus \Gamma_2 \oplus \Gamma_3 \oplus \Gamma_4, \\ P_{6z} : \Gamma_5 \otimes \Gamma_4 &= \Gamma_5, \\ P_{7xy} : \Gamma_5 \otimes \Gamma_5 &= \Gamma_1 \oplus \Gamma_2 \oplus \Gamma_3 \oplus \Gamma_4, \\ P_{7z} : \Gamma_5 \otimes \Gamma_4 &= \Gamma_5. \end{aligned} \tag{7.5}$$

In D_{2d}, one and two photons in dipole order can excite states of the following symmetries (longitudinal z-polarization is not shown):

$$\begin{aligned} \text{one dipole} &: \Gamma_{5(x,y)}, \\ \text{two dipoles} &: \Gamma_{5(x,y)} \otimes \Gamma_{5(x,y)} = \Gamma_1 \oplus \Gamma_2 (= 0) \oplus \Gamma_3 \oplus \Gamma_4. \end{aligned} \tag{7.6}$$

Therefore, although parity is not a good quantum number in ZnSe, only P-states of corresponding representation are excited by two photons. Furthermore, one photon is emitted solely from S-states. To observe SHG, S- and P-excitons have to be mixed. Mixing of these states can not directly be achieved by applying a magnetic field of even parity which mixes only states of the same parity. In principle, states can be mixed by the odd-parity effective electric field due to the Magneto-Stark effect [101]. The field

allows mixing of all three possibly excited P-states to the Γ_5 S-state which can in turn emit one photon in dipole order. The mixing of the 1S and 2P exciton is expected to be of low efficiency because the energy distance between both is about 15 meV in bulk material (estimated from 1S exciton binding energy of 20 meV [82]). However, the mixing of 12 meV split 1S para- and ortho-exciton in Cu_2O in magnetic field allows to detect the otherwise forbidden para-exciton, too [102]. The expected anisotropies of the three mixed states are given in Fig. 7.9. None of the calculated pattern fits

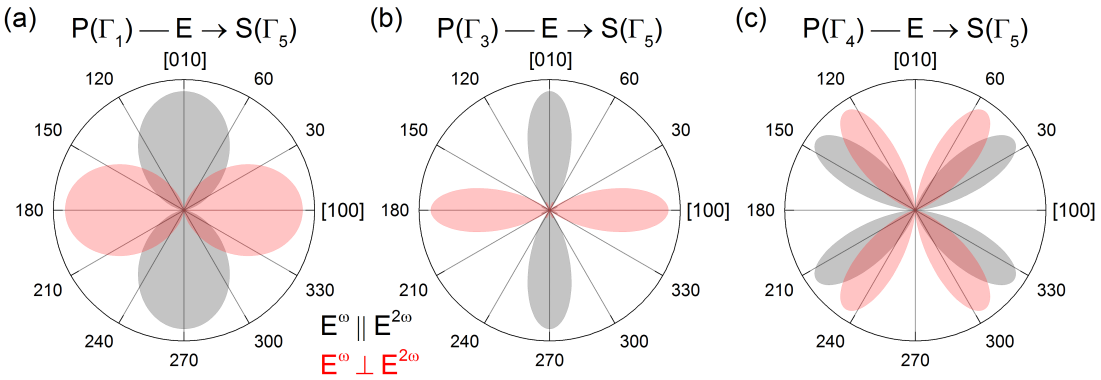

Figure 7.9: Simulation of SHG anisotropies for point group D_{2d} with an electric field mixing P-excitons of (a) Γ_1, (b) Γ_3 and (c) Γ_4 symmetry to an S-exciton of Γ_5 symmetry. Grey and red shaded areas show the pattern for the configurations $\mathbf{E}^{\omega} \parallel \mathbf{E}^{2\omega}$ and $\mathbf{E}^{\omega} \perp \mathbf{E}^{2\omega}$, respectively.

the experimental results in Fig. 7.4. Therefore, another effect, related to the type-II quantum well structure, is considered in the following.

During excitation, holes of the created excitons might move from their above barrier states in the ZnSe well to the energetically favourable region of the BeTe barriers. At the same time, the photogenerated electrons remain in the ZnSe layer. Between the oppositely charged carriers an electric field is built up that points along the crystal z-axis. Such a field reduces the MQW symmetry further to point group C_{2v} (mm2).

The symmetries of the conduction and the valence bands are all Γ_5, as seen in Fig. 7.10. Symmetries and spin contributions of S- and P-excitons with holes from the uppermost valence band are (pure triplet states are plotted in red):

$$\begin{aligned} S_1 : \Gamma_5 \otimes \Gamma_5 \otimes \Gamma_1 &= \Gamma_1 \oplus \Gamma_2 \oplus \Gamma_3 \oplus \Gamma_4, \\ P_{1x} : \Gamma_2 \otimes \Gamma_2 &= \Gamma_1, \\ P_{1y} : \Gamma_2 \otimes \Gamma_4 &= \Gamma_3, \\ P_{1z} : \Gamma_2 \otimes \Gamma_1 &= \Gamma_2. \end{aligned} \tag{7.7}$$

Accordingly, the representations of excitons with holes from the second highest valence

band, which originates from the Γ_4 level, are

$$\begin{aligned} S_2 : \Gamma_5 \otimes \Gamma_5 \otimes \Gamma_1 &= \Gamma_1 \oplus \Gamma_2 \oplus \Gamma_3 \oplus \Gamma_4, \\ P_{2x} : \Gamma_4 \otimes \Gamma_2 &= \Gamma_3, \\ P_{2y} : \Gamma_4 \otimes \Gamma_4 &= \Gamma_1, \\ P_{2z} : \Gamma_4 \otimes \Gamma_1 &= \Gamma_4. \end{aligned} \tag{7.8}$$

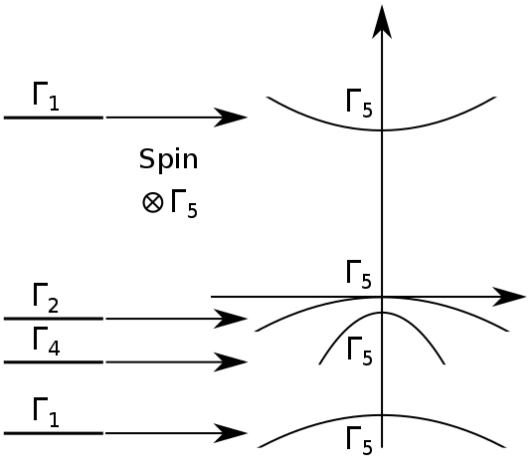

Figure 7.10: Symmetries of bands in a crystal of C_{2v} symmetry, without and with spin.

In C_{2v}, also the photon symmetries are split further. For one photon they are (z-polarization is not shown)

$$\begin{aligned} &\text{along x} : \Gamma_2, \\ &\text{along y} : \Gamma_4. \end{aligned} \tag{7.9}$$

Two photons are able to excite states of

$$\begin{aligned} \Gamma_2 \otimes \Gamma_2 &= \Gamma_1, \\ \Gamma_4 \otimes \Gamma_4 &= \Gamma_1, \\ \Gamma_2 \otimes \Gamma_4 &= \Gamma_3. \end{aligned} \tag{7.10}$$

Application of magnetic field along the x-direction induces also an effective electric field (MSE) along the y-direction. This effective field of Γ_4 symmetry mixes states of Γ_2 and Γ_3, or of Γ_1 and Γ_4, respectively. From these findings it is possible to excite the P_{1y} state of Γ_3 which is mixed with the S_1 state of Γ_2. On the other hand, the P_{2y} state of Γ_1 can be excited by either two photons polarized along x (Γ_2), or along y (Γ_4) that is mixed with S_2 of Γ_4. For these three processes the rotational anisotropies are shown in Fig. 7.11.

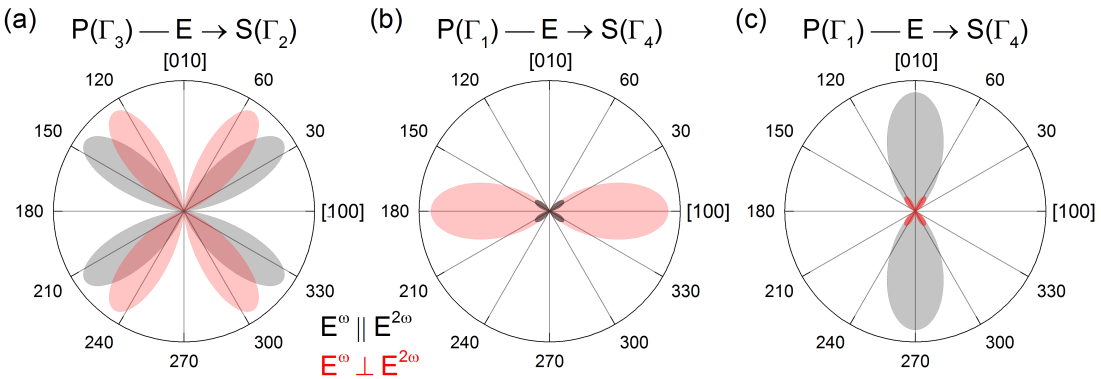

Figure 7.11: Simulation of SHG anisotropies for point group C_{2v} with an effective electric field mixing a P-exciton of (a) Γ_3 to an S-exciton of Γ_2 symmetry. (b) and (c) show the mixing of a P-exciton of Γ_1 symmetry, excited by two photons of either x, or y polarization and mixed to an S-exciton of Γ_4 symmetry.

The anisotropy pattern shown in Fig. 7.11(c) clearly matches the shape found in experiment, Fig. 7.4(a) and (b).

7.5.2 THG selection rules

The THG anisotropies in absence and in magnetic field in Figs. 7.6 and 7.7 are also treated in the point group C_{2v}. By three photons, polarized along x-, or y-direction [Eq. (7.9)] in dipole order, the following states are excited:

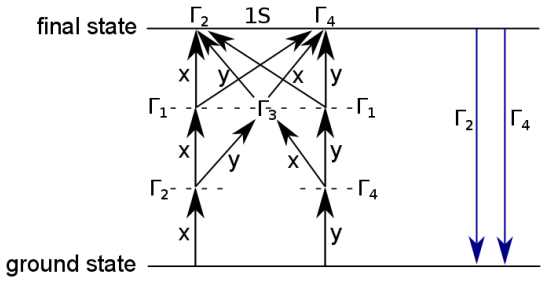

Figure 7.12: THG 1S excitation and emission channels in C_{2v}.

$$\begin{aligned} \text{xxx} &: \Gamma_2 \otimes \Gamma_2 \otimes \Gamma_2 = \Gamma_2, \\ \text{yyx} &: \Gamma_4 \otimes \Gamma_4 \otimes \Gamma_2 = \Gamma_2, \\ \text{xxy} &: \Gamma_2 \otimes \Gamma_2 \otimes \Gamma_4 = \Gamma_4, \\ \text{yyy} &: \Gamma_4 \otimes \Gamma_4 \otimes \Gamma_4 = \Gamma_4. \end{aligned} \tag{7.11}$$

Note, that further three photon excitation channels which are permutations of yyx and xxy are equal to these.

To simulate the measured anisotropies, it is necessary to include all four channels from Eq. (7.11). To achieve the signal shape, the contributions have to be added first and only then be squared to obtain the overall THG signal intensity. Therefore, it is concluded that interferences of the two 1S resonances of Γ_2 and Γ_4 are of importance. This points at a small splitting in energy of both states which can not be resolved by

the monochromator and CCD camera, cf. Sec. 5.5.4. The full fitting functions for the parallel and perpendicular configuration are

$$I^{C_{2v}}_{\mathrm{THG},\parallel} \propto (\mathrm{xxx}\,\sin^4(\psi) + \mathrm{yyy}\,\cos^4(\psi) + (\mathrm{xyy} + \mathrm{yxx})\,\sin^2(\psi)\cos^2(\psi))^2, \quad (7.12)$$

$$I^{C_{2v}}_{\mathrm{THG},\perp} \propto ((\mathrm{xyy} - \mathrm{yyy})\,\cos^3(\psi)\sin(\psi) + (\mathrm{xxx} - \mathrm{yxx})\,\cos(\psi)\sin^3(\psi))^2. \quad (7.13)$$

The fit results are plotted together with the data from Fig. 7.6 in Fig. 7.13. Values of the parameters from Eqs. (7.12 and 7.13) are given in Table 7.1. It is notable that for

Table 7.1: Parameter values from the fits of Eq. (7.12) to the experimental results in Fig. 7.13.

	Trion	1S	a	b
xxx	0.994	0.988	0.993	0.948
xyy	0.963	0.439	1.12	1.10
yyy	0.968	0.957	0.975	0.983
yxx	0.354	1.28	0.385	0.349

the 1S-exciton the parameter xyy is lower than that of the others, while for the other resonances the parameter yxx is only about one third of the other parameters. The anisotropies in crossed configuration can not be fitted with the mechanism proposed in this section. They are maybe due to quadrupole channel contributions, or due to strain in the sample.

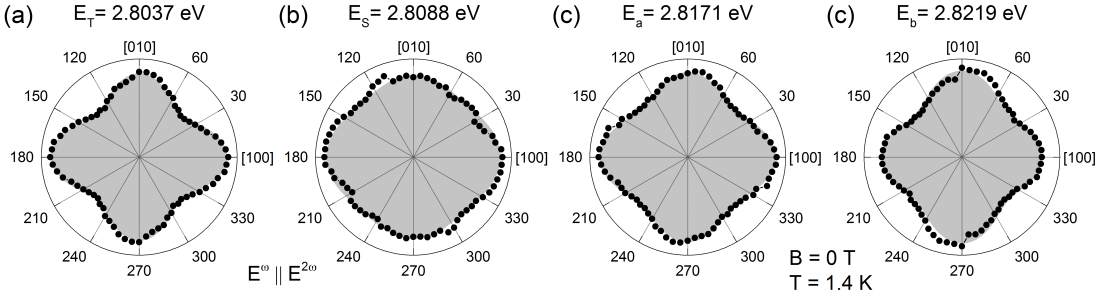

Figure 7.13: Simulation and data of THG anisotropies for point group C_{2v} for (a) trion, (b) S-exciton, (c) resonance a and (d) resonance b. Filled black dots show measurement data and grey shaded areas give the best fit to the data of Eq. (7.12) in $\mathbf{E}^{\omega} \parallel \mathbf{E}^{2\omega}$ configuration.

In magnetic field, the anisotropy patterns slightly change shape, as shown in Fig. 7.7. The magnetic field induced THG contributions are expected to be small compared to the already allowed ones [87]. Additional contributions, or redistribution of oscillator strengths might arise from mixing of allowed P- with S-excitons, or mixing to one-photon forbidden states which can not emit light after excitation with two photons.

7.6 SHG with spectrally broad fs-pulses

In the preciding sections, SHG and THG spectra of ZnSe/BeTe MQW are measured by scanning the wavelength of ps-pulses. These are now compared to SHG spectra taken by applying fs-pulses to the sample.

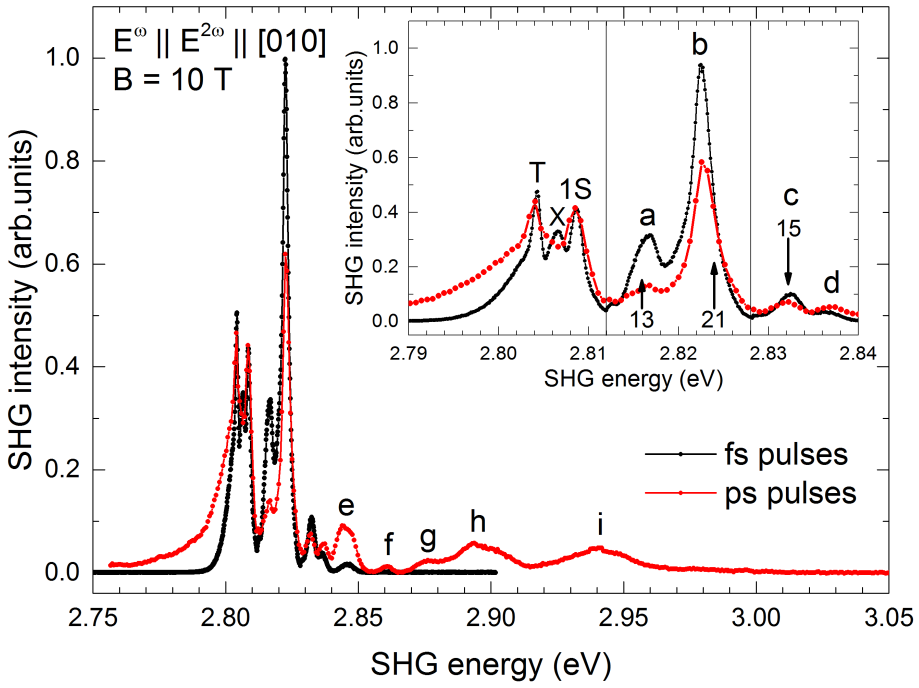

Figure 7.14: Comparison of SHG spectra at 10 T, detected with excitation by femtosecond (black dots) and picosecond laser pulses (red dots), respectively. The inset shows a zoom to the energy range of 2.79−2.84 eV. There, the trion and lowest 1S exciton are marked by T and 1S, as well as the undefined resonances X, a, b, c and d. Furthermore, the inset shows that the spectrum, excited with femtosecond laser pulses, is comprised from three spectra with the photon energy centered at 1.401 eV, 1.408 eV and 1.414 eV.

In Fig. 7.14, the SHG picosecond scan (red) is plotted together with the femtosecond SHG spectrum (black) at 10 T. Resonances g−i at energies far above the lowest exciton lines,are maybe transitions from low lying valence bands. To achieve a broader spectral range with fs-pulses, the energy of the exciting photons is set to 1.401 eV (885 nm), 1.408 eV (881 nm) and 1.414 eV (887 nm), respectively. Parts of these three spectra, divided by vertical lines, are shown in the inset of Fig. 7.14. In the fs-spectrum, exciton resonances are slightly more pronounced, e.g. line b exhibits a FWHM of 3.2 meV in the ps-spectrum and 2.7 meV in the fs-spectrum. In the case of lines a and b, the spectral intensity of the fs-pulses might increase the intensity of line b, whereas that of line a is

reduced. Picosecond pulses show the correct ratio of line intensities.

At spectral energy below the trion resonance, more intense signal is present in the ps-spectrum. Futhermore, a third resonance, labelled by X, is observed 2 meV below the 1S and 2.3 meV above the trion in the fs-spectrum.

The fs-excitation power dependence of SHG signal intensity at 5 T is shown in Fig. 7.15. In panel (a), spectra for different average excitation power in the spectral range of the trion and 1S resonance are plotted. The overall spectral intensity is given in panel (b). From theory, a quadratic increase of SHG intensity is expected. However, up to an excitation power of 24 mW the signal increases linearly before it decreases with excitation power up to 100 mW. The signal intensity remains almost constant around 50 mW excitation power. In the ranges of 24 mW to 50 mW and from 60 mW to 100 mW, the decrease can be described each time by a quadratically falling function. This might indicates that two mechanisms are responsible for the signal decay and are specific for MQWs with a type-II band alignment. With increasing excitation power, the ratio of trion and 1S exciton changes from equal intensity to a stronger 1S resonance. The

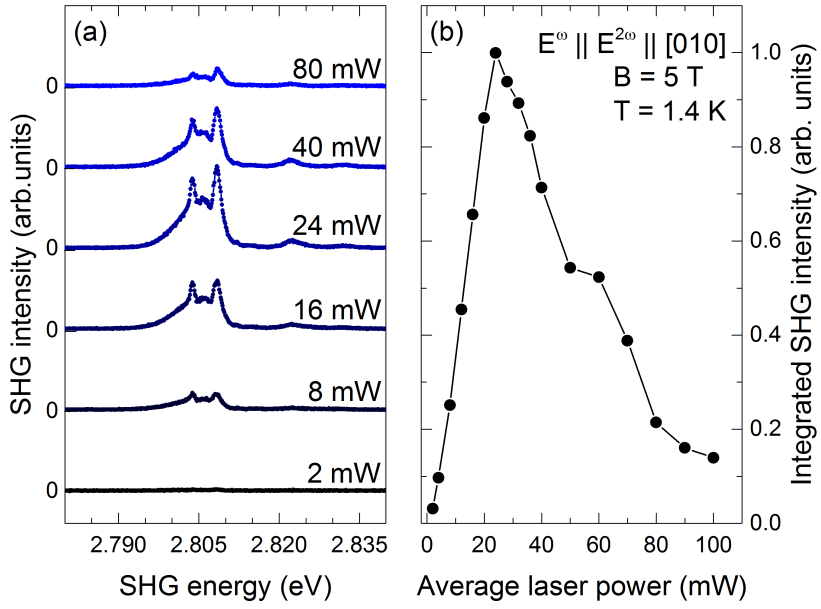

Figure 7.15: (a): SHG spectra at $B = 5$ T for increasing average laser excitation power up to $P = 80$ mW and (b) Integrated SHG intensity in dependence of average excitation laser power.

linear development of SHG intensity up to 24 mW might be due to an enhanced number of separated carriers. At low excitation power, only a few holes move from the ZnSe layer into the energetically favourable BeTe layer, introducing the internal electric field. Therefore, the MQW point group changes from D_{2d} to C_{2v} with increasing power. This effect saturates because the internal field tilts the bands building an effective barrier

for the holes between ZnSe and BeTe layer [90, 95]. At even higher excitation power it could be assumed that carriers accumulate in the ZnSe layers, build a blockade effect [46] and prevent excitons from being generated.

7.7 SHG in tilted geometry

The sample is tilted around its vertical axis, i.e. around [010], by an angle θ. The external tilting angle is $\theta = 40°$ which corresponds to about 12° internal angle due to the index of refraction. In Fig. 7.16(a), the fundamental femtosecond photon energy is set to 1.408 eV (881 nm), red data plot and to 1.387 eV (894 nm), blue plot. For the former one, SHG signal is present for an energy range of 18 meV with several intensity minima, while the signal for the latter case resembles a Gauss-function. To obtain a

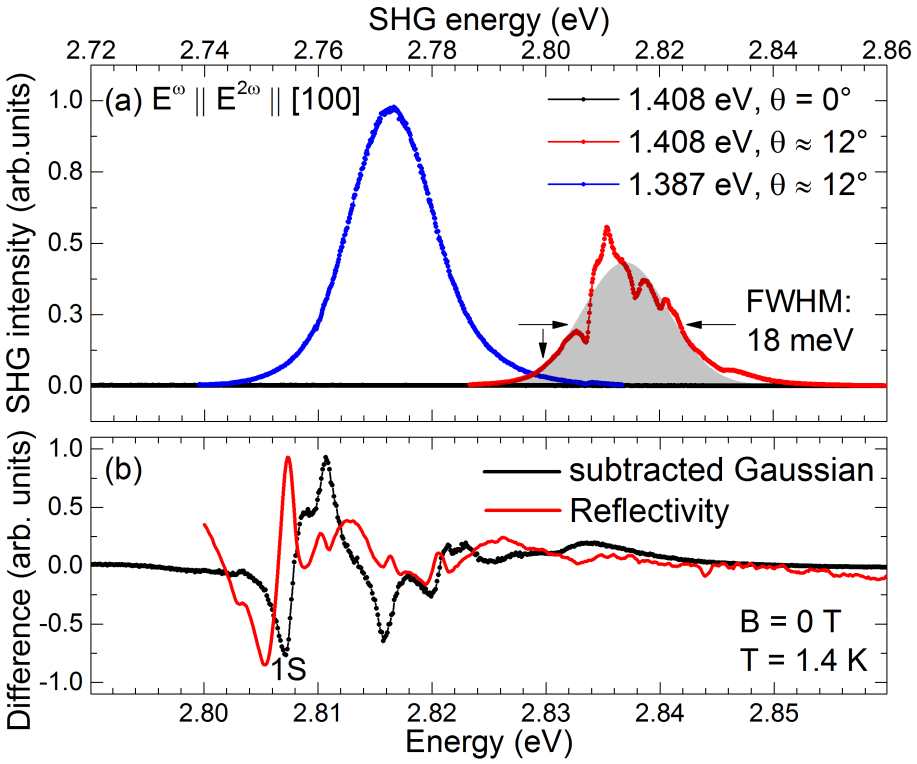

Figure 7.16: SHG signal from the sample in tilted geometry. (a): No signal with the sample at normal incidence (black). With an internal angle of $\theta \approx 12°$ the fundamental laser photon energy is set to 1.408 eV (red) and 1.387 eV (blue). The grey shaded area at the red curve is the best Gaussian fit to this data. (b): Comparison of (i) the difference between the data in tilted geometry with excitation at 1.408 eV and Gaussian fit (shaded area) in (a) (black line) and (ii) white light reflectivity spectrum (red line).

more illustrative picture of the intensity minima in the SHG spectrum, a gauss shape (grey shaded area in (a)), fitted to the data is subtracted from the detected signal. The

difference intensity is plotted in Fig. 7.16(b) and compared to the reflectivity data from Fig. 7.2. The dips in both spectra differ in their energy position. However, while in the subtracted spectrum the energies are connected to the absorption, the shape of a reflectivity resonance changes depending on the distance to the sample surface and its dispersion.

The intensity minima in the SHG spectrum, Fig. 7.16(a), are explained by the following mechanism. Tilting of the sample changes the light **k**-vector and the polarization direction relative to the crystal system. Therefore, a symmetry analysis predicts excitation of further exciton components, making SHG allowed. However, the point group of the crystal is not changed by turning it. In order to explain the gaussian shape of the SHG signal, the GaAs substrate of 0.5 mm thickness is considered. It is described by point group T_d and has a band gap energy of 1.52 eV [103] at low temperatures. Therefore, the fundamental fs-light spectrum which first passes the substrate generates SHG far above the band gap of GaAs. This frequency-doubled spectrum then passes the MQW where light is absorbed by the exciton states in one-photon processes. As soon as the fundamental photon energy is set to higher or lower values than needed to meet the exciton energy of ZnSe in SHG, the detected spectrum is of pure Gaussian shape.

The rotational anisotropy of the substrate SHG signal is shown in Fig. 7.17 together with simulations. A comparison of the current data with those of I. Sänger [13, p. 51] on GaAs bulk material reveals the shape of the simulation in (b). This contradiction

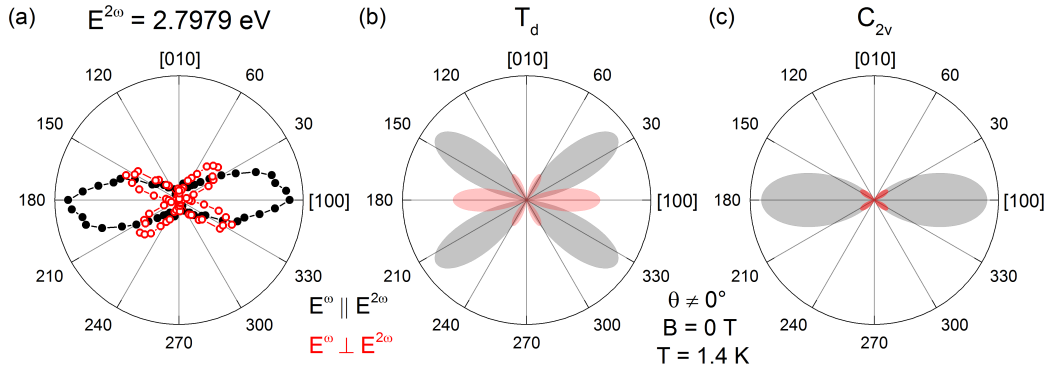

Figure 7.17: Analysis of the rotational anisotropy in tilted geometry at $E^{2\omega} = 2.7979$ eV. (a) Filled black and open red dots represent the experimental data for the configurations $\mathbf{E}^{\omega} \parallel \mathbf{E}^{2\omega}$ and $\mathbf{E}^{\omega} \perp \mathbf{E}^{2\omega}$, respectively. Simulations of the anisotropy on the basis of point groups D_{2d} and C_{2v} are given in (b) and (c). Grey and red shaded areas correspond to $\mathbf{E}^{\omega} \parallel \mathbf{E}^{2\omega}$ and $\mathbf{E}^{\omega} \perp \mathbf{E}^{2\omega}$.

could be cleared when assuming that the internal electric field from the quantum well layers also influences the GaAs substrate and its SHG signal. In Fig. 7.17(c), the point group C_{2v} which describes T_d with an electric field along the z-axis is used. The shape for parallel configuration is correct, whereas the intensity ratio of the crossed shape is too small.

7.8 Conclusions

In this chapter, the first SHG and THG spectra on a multiple quantum well structure are presented. Energetic positions of the lowest 1S exciton and trion are determined in reflectivity and PL, as well as several further states. For light incident to the sample along the crystal [001]-direction, SHG signal is only observed after application of a magnetic field. An analysis of rotational anisotropies indicates that besides the external magnetic field an internal electric field, which further reduces the crystal symmetry, is necessary to observe SHG.

The 1S exciton resonance energy is 2.8067 eV in linear measurements and is determined for SHG at 0 T to 2.8081 eV. The remaining difference of 1.4 meV is considerably smaller than for ZnSe bulk material (4-5 meV). There, the difference was assigned to the polariton dispersion. However, no shift in energy is observed between the 1S resonance in SHG and THG. If the present energy shift in SHG is also due to polaritons is still under discussion. On the one hand, polaritons form due to several circles of exciton-photon, photon-exciton conversion which is not possible within a structure much smaller than the light wavelength. On the other hand, polaritons are considered new eigenstates of the coupled exciton-photon system that can not be split up into exciton and photon. They exist throughout the whole sample, as soon as light enters the system. Therefore, the question remains whether the energy shift of the 1S resonance originates from a MQW polariton-dispersion, or from a quantization effect. In the latter case, the quantum confinement effect is smaller than expected from infinite high barrier potentials. Thus, these can not be considered high in terms of confining, or an increase of exciton binding energy in the well compensates a part of the shift.

The SHG intensity shows an unusual dependence on the excitation power. It might be assigned to the type-II band structure which allows for carrier separation. Conceivable (Blockade-) effects that reduce the SHG signal for increased excitation power should be the subject of further studies.

From the three-photon symmetries [Eq. (7.11)], two aspects of THG signal can be discussed. It is noted that the generation of separated carriers in the well and barrier layer should be smaller for the higher order nonlinear THG process. However, by two photons only P-excitons of lower oscillator strength are excited. Whereas, three photons can excite S-excitons of higher oscillator strength. Therefore, both effects could average out to produce similar quantities of separated carriers. The previous observation, that the THG signal is about four times more intense than in SHG measurements, is also explained by selection rules. While mixing of S- and P-excitons is necessary to induce SHG, THG is allowed directly. Therefore, THG, although a higher order nonlinear process, is more intense than SHG.

In tilted geometry, SHG from the GaAs substrate is the main contribution to the signal. Subsequently, the quantum well excitons absorb in one-photon processes at their energies. This mechanism could be applied for materials where lower lying bands can generate SHG signal which is absorbed by exciton states of a higher energy band. However, the two cases differ as the substrate signal is generated before it passes the quantum well structure. Whereas a lower lying band is present in all "layers" of a bulk

semiconductor. In principle, there could be a substrate contribution to the signal for SHG in magnetic field and in THG, too. These contributions are considered to be of low intensity compared to the signal of quantum well excitons. Furthermore, SHG and THG from the substrate should show no distinct resonances as the energy of two or three photons is well above the band gap in the continuum states of GaAs. In Figs. 7.3 and 7.5, the signal drops close to zero intensity outside the exciton resonance range. This proves that substrate contributions can be neglected for measurements in normal light incidence ($\mathbf{k}^{\omega} \parallel [001]$).

8 ZnO/(Zn,Mg)O multiple quantum wells

In contrast to Cu_2O and ZnSe in the preceding chapters, ZnO crystallizes in the hexagonal wurtzite structure with the point group C_{6v} (6mm). In Fig. 8.1(a), the ZnO band structure is shown. The valence band is split into three bands, denoted by A, B and C. Their energetic order is still a subject of discussion. Here, the "inverted" order is presented [104]. The band gap between conduction band and A-valence band is given by $E_{\mathrm{g}}^{\mathrm{ZnO}} = 3.441$ eV at 6 K [105] and the difference between A and B band by 5 meV. The exciton binding energy is about $E_{\mathrm{bind}}^{ex} = 60$ meV with a Bohr radius of $a_{\mathrm{b}}^{\mathrm{ZnO}} = 1.8$ nm. SHG measurements were performed on ZnO bulk material [106] and the Magneto-Stark effect proposed [101]. An overview of the extensive research on ZnO can be found in [107, 108].

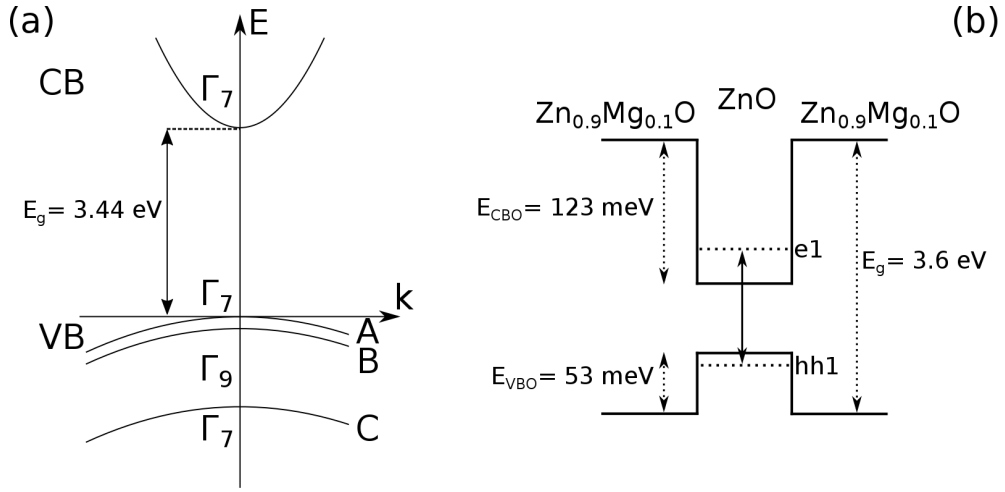

Figure 8.1: (a) Band diagram and irreducible representations of ZnO in symmetry C_{6v}. (b) Scheme of type-I valence and conduction band alignment and energies.

The band gap of ZnO can be enlarged (reduced) by admixture of magnesium (cadmium) [109]. Therefore, MQW structures with ZnO as well material and ZnMgO as barrier layer are feasible. In contrast to the ZnSe/BeTe-MQW, this structure shows a type-I band alignment where both, electrons and holes, have their energy minimum in the ZnO wells, see Fig. 8.1(b). The confinement potentials shown are calculated from values given for barriers with 12 % Mg [110] by assuming linear dependence on the Mg concentration. An overview of excitons in ZnO-based quantum wells is given in [110].

8.1 Samples

Samples of different well widths are provided by C. Meier from Universität Paderborn (L_w = 1.8 nm) and by S. Sadofev from Humbolt-Universität zu Berlin (L_w = 2.9 – 10 nm). Their compositions and layer order are shown in Fig. 8.2. The barriers in all samples contain 10 % Mg ($ZnO/Zn_{0.9}Mg_{0.1}O$) which is far below the solubility limit of Mg in ZnO of 33 % in thin films [111].

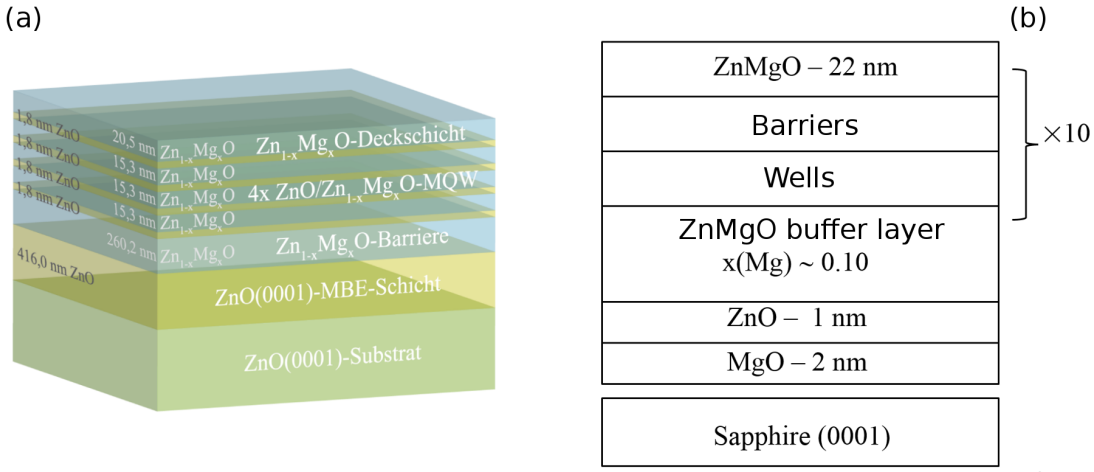

Figure 8.2: Structures of (a) 1.8 nm multiple quantum well and (b) 2.9 – 10 nm multiple quantum well samples.

The parameters for the samples are summarized in Tab. 8.1. Given are sample number (no), well width L_w, barrier width L_b, number of periods, thickness of ZnMgO buffer layer and the substrate material. All samples are grown either on ZnO (a) or sapphire (b) (0001) substrate.

Table 8.1: Parameters of ZnO/(Zn,Mg)O-MQW samples.

no	L_w (nm)	L_b (nm)	periods	ZnMgO buffer layer (nm)	substrate
133	1.8	15.3	4	260.2	ZnO
2262	2.9	7.2	20	593	sapphire
2182	3.2	8	10	660	sapphire
2183	4.5	8	10	690	sapphire
2187.2	10	8	10	770	sapphire

8.2 Theory

Similar to the case of ZnSe/BeTe-MQW, valence and conduction band are quantized in the well layers. The quantization energies of the first electron and hole level for infinite high barrier potentials are calculated by Eq. (7.1) for each sample. Effective masses for electron and hole of $m_e = 0.28\ m_0$ and $m_h = 1.8\ m_0$ are used [112]. The quantization energies for the different well widths are summarized in Table 8.2. As

Table 8.2: Quantization energies of first electron (e1) and heavy-hole (hh1) level in the ZnO well layers, calculated for infinite high barrier potentials.

no	L_w (nm)	E(e1) (meV)	E(hh1) (meV)
133	1.8	1060	165
2262	2.9	410	63.7
2182	3.2	337	52.4
2183	4.5	170	26.5
2187.2	10	34.5	5.36

the confining potentials are in the range of 100 meV, i.e. being far from infinite, the quantization energies can be expected much lower than the calculated ones for infinite barrier potential. Furthermore, except for the 10 nm MQW, the quantization energies are much larger than the confinement potentials. Therefore, only the e1 and hh1 level will be bound, as there is always one bound state [99], but no higher states will be present.

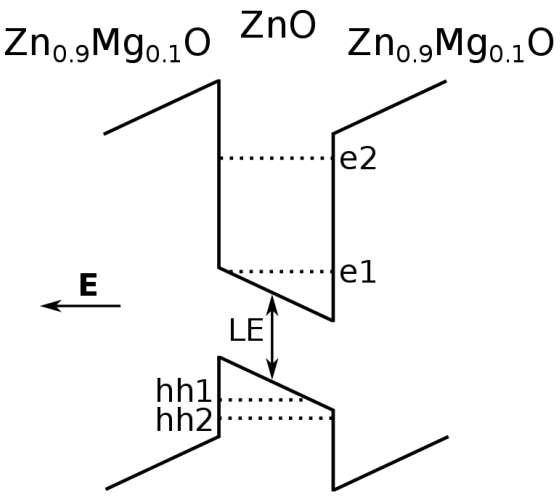

Figure 8.3: ZnO-MQW bandstructure under the influence of an internal electric field **E**.

While quantum confinement dominates the exciton energy shifts in the narrow quantum well regime, the piezoelectric effect is known to have greater influence on resonances in broad quantum wells [113, 114]. It is due to lattice mismatch between wells and barriers. This results in spontaneous and piezoelectric polarization, as observed in GaN/AlN superlattices [115], and finally in built-in electric fields along the growth (0001)-direction (c-axis of the sample). Exciton states are influenced by this internal field as electrons and holes are forced to opposite sides of the wells. Thus, their binding energy and the oscillator strength are reduced and exciton lifetimes extended. As shown in Fig. 8.3, the band structure gets tilted by the electric field and quantization levels shifted towards lower energies. Furthermore, at lower energy, emission from localized excitons

(LE) can appear which is due to well layer thickness fluctuations. The built-in fields are expected to be dependent on at least three parameters.

(i) The Mg-concentration in the barriers influences the lattice mismatch between wells and barriers. Therefore, a higher Mg-concentration increases the mismatch which linearly increases the internal electric fields [116].

(ii) The effect of the built-in fields increases linearly with the well width L_{w}. As shown in Fig. 8.3, the energy difference between the interfaces of the well will be larger for a broader well.

(iii) In addition, the width of the barriers, L_{b}, effects the internal fields, too. The field increases proportional to the ratio [117]:

$$L_{\mathrm{b}}/\left(L_{\mathrm{w}}+L_{\mathrm{b}}\right). \tag{8.1}$$

All samples in this study contain the same ratio of Mg in the barriers. Also the ratios of barrier to well width only slightly decreases with well width. Therefore, an increasing effect of internal electric field is expected exclusively by broadening of the well layers.

8.3 PL measurements

The samples and resonance energies are first characterized by photoluminescence measurements in reflection geometry. Therefore, excitation is performed by ps-pulses at 3.8 eV (325 nm). To avoid absorption by air and silver mirrors (and their replacement by Al-mirrors), the ps-OPA is set to 650 nm and is frequency doubled by a BBO-crystal in front of the cryostat.

In Fig. 8.4(a), PL signals of all samples are shown. The sample with $L_{\mathrm{w}} = 1.8$ nm exhibits two broad peaks at 3.4175 eV and 3.3756 eV with 30 meV FWHM and in addition two narrow lines at 3.360 eV and 3.3562 eV which might be assigned to excitons bound to neutral acceptors [118, 119]. The samples of 2.9 nm to 4.5 nm show narrow lines, with a FWHM of about 5 meV. In contrast, in the sample with 10 nm wells, the resonances are broadened to about 15 meV which is might due to enhanced exciton-phonon coupling by internal electric field. For the samples of well width 3.2 nm and 4.5 nm, an additional peak in the low energy shoulder of the most intense peak is present. Much less intense peaks, marked by arrows, appear for samples of well width 2.9 nm, 3.2 nm and 10 nm. They show an energy difference of 73.7 meV, close to the LO-phonon energy in ZnO [120], to the peaks marked by the same colour by dots and are therefore phonon replica of these.

There are several potential assignments of the peaks in Fig. 8.4(a). Observation of the lowest exciton state, the 1S, could be possible. It is, however, shifted to higher energies due to quantum confinement [Eq. (7.1)] and to lower energies by increasing binding energy. Frequently a localized exciton (LE) is reported [121]. This peak is stokes-shifted by about 20 meV with respect to the exciton absorption due to quantum-well thickness fluctuations and imperfections [110]. Energetically close to, or below the LE, negatively charged trions (X^-) and bi-excitons (XX) are observed with binding energies of 13 meV [122] and 19 meV [123], respectively. The bi-exciton binding energy

in ZnO bulk is 15 meV [124]. At even lower energy, the emission from exciton-exciton scattering was observed and denoted by P band which is about the exciton binding energy below the exciton [125]. This process has a higher excitation power threshold than XX emission [123]. For broader wells, or samples with higher Mg concentration in the barriers the piezoelectric effect can lead to additional emission as discussed in Sec. 8.2. Reported shifts are 40 meV below the LE line [121].

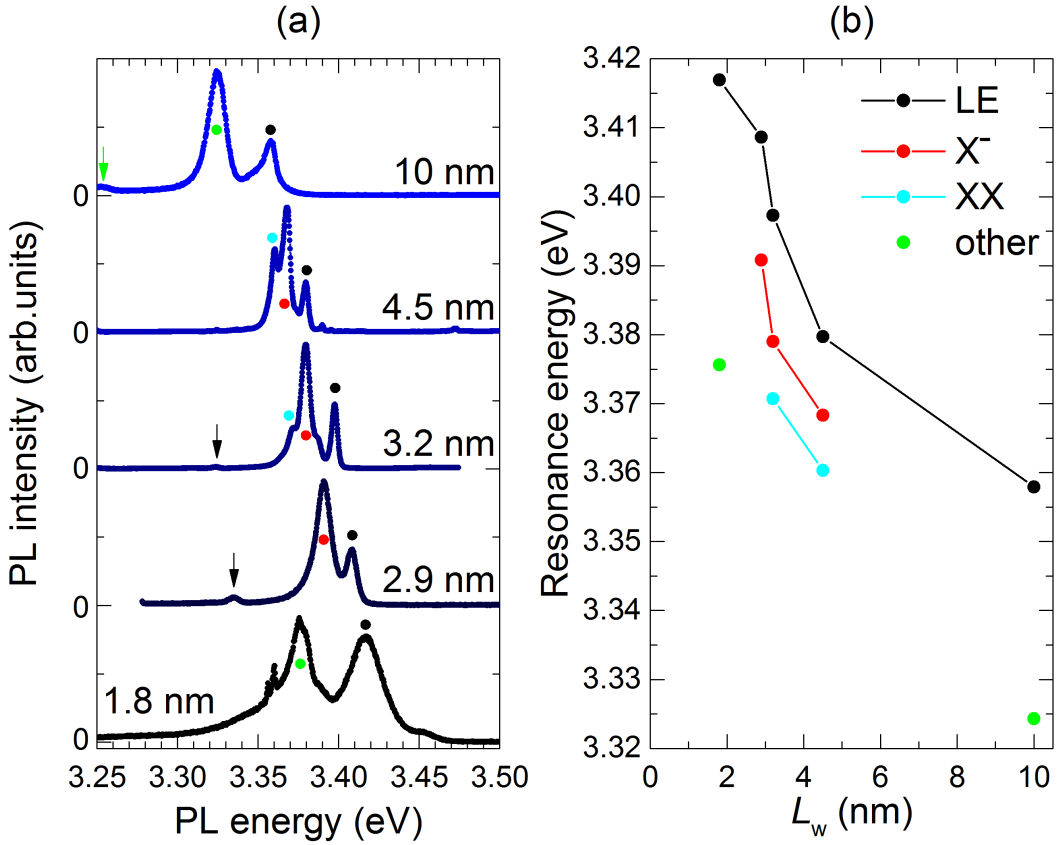

Figure 8.4: (a): PL spectra of samples with different well widths L_w. Resonances are marked with dots of different colours. LO-phonon replicas are marked by arrows of the corresponding peak colour. (b): Energies of PL peaks in the spectra in (a). Colours indicate the respective resonances in the PL spectra.

In Fig. 8.4(b), the peak energies are plotted in dependence of the well width to gain more information about the origin of the states. The energetically highest peak observed in each MQW (black dots) might be of one common origin and are therefore connected by a line. They are either resonances of the 1S exciton, or of the corresponding LE, shifted to slightly lower energies. For well width of 4.5 nm to 2.9 nm, the resonances show a steep increase in energy with decreasing well width which is attributed to quantum

confinement. The peak position for the 1.8 nm MQW does not follow this trend. One reason might be the relatively small well width. For those, the exciton binding energy decreases due to increasing penetration of the exciton wave function into the barrier layers, as calculated by Coli and Bajaj [126] and experimentally observed [110]. A second reason could be a different sample quality as all samples except the 1.8 nm wells originate from the same source.

The highest resonance in the 10 nm sample might be influenced by the built-in electric fields as its energy is shifted below the 1S resonance energy in ZnO bulk of 3.3759 eV [127]. Next, the second highest peak for samples with 2.9 nm to 4.5 nm wells are thought to be of the same origin (red dots). The energy difference to the highest peaks in each sample is 17.8, 18.3 and 11.4 meV, for the MQW with 2.9, 3.2 and 4.5 nm, respectively. These values are in the range of reported binding energies for trions of 13 meV (3.5 nm) [122] and XX of 19 meV for well widths of 3.5 nm [122] and 3.7 nm [123]. The resonances will be assigned to trions after discussion of the intensity dependence on excitation power in Fig. 8.5. In the samples of well width 3.2 and 4.5 nm, a low energy shoulder of the X^- resonances is present (light blue dots). They are located 26.6 and 19.4 meV below the LE resonance, being comparable to reported XX binding energies of 19 meV [110, 122]. The remaining peaks of the spectra in Fig. 8.4(a) are shown by green dots in Fig. 8.4(b). The origin of the peak for the 1.8 nm MQW might be the LE for the higher peak, shifted by 42 meV to lower energy. The ZnO substrate and buffer layer could also be the origin of this line as its energy is close to the 1S exciton energy in ZnO bulk material. The red-shift of the resonance at 3.325 eV in the 10 nm MQW is assigned to an internal electric field, as shown in Fig. 8.3. Furthermore, a LO-phonon replica of this line is present in the spectrum (marked by an arrow). Due to the greater distance of the electron and hole in the electric field, its coupling to phonons is enhanced [28].

The assignment of resonances is supported by excitation-power dependent PL measurements. For samples of well widths $2.9 - 10$ nm, these measurements are shown in Fig. 8.5. With increasing power, more free carriers are generated, able to screen the built-in electric field. The degree of screening is measured by the increase of resonance energy. Therefore, the piezoelectric field could be estimated from the shift as was tested in [113]. In the 10 nm sample, Fig. 8.5 (d), the peak at lower energy displays a small shift of 1.5 meV towards higher energies up to 2 mW, before shifting back at higher excitation powers. However, no such effect is observed in the other narrow-well samples indicating that internal fields play a minor role there. With increasing well width the XX resonance becomes more dominant. In 2.9 nm wells, no resonance is observed while it can be resolved for 3.2 nm wells and grows superlinearly and overtakes the LE resonance in 4.5 nm wells for increasing excitation powers. By Eq. (4.3), the excitation power is calculated to be 13 kW/cm^2 for 1 mW average laser power and an unfocussed beam of 1 cm diameter. It is also seen that the intensity of the LO-phonon replica of the LE resonance decreases with increasing well width. This is contrary to the statement that the phonon coupling to the LE should increase with exciton radius [28], as exciton binding energy increases (radius decreases) with smaller well width. The formerly mentioned P band is not observed here, as it has a larger excitation threshold than the

bi-exciton [123].

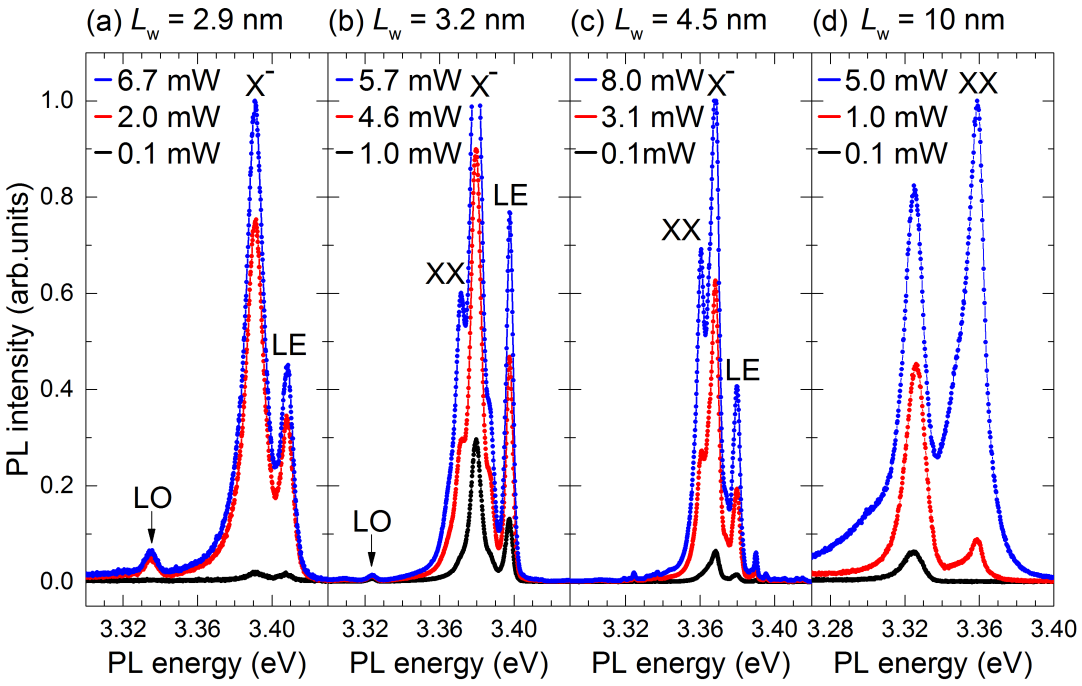

Figure 8.5: Excitation-power dependent photoluminescence spectra of samples with (a) 2.9 nm, (b) 3.2 nm, (c) 4.5 nm and (d) 10 nm well width. Resonances are labelled with LE: localized exciton, X^-: trion, XX: bi-exciton and LO: longitudinal-optical phonon replica of LE.

8.4 SHG measurements

SHG spectra with light shone to the sample surface in normal incidence, i.e. $\mathbf{k}^{\omega} \parallel [0001]$, of the five samples are shown in Fig. 8.6(a). Care was taken to excite the samples from the substrate side to avoid possible reabsorption of the SHG signal.

For the sample with 1.8 nm quantum wells, no SHG signal is detected which might be attributed to the low amount of well material in four quantum wells, or to sample quality. SHG signal is also very weak for the 10 nm MQW sample. Two shallow resonances, separated by the LO-phonon energy, are indicated by arrows. The reason for the low signal intensity is probably the internal electric field which reduces the exciton oscillator strength. Samples of intermediate well width of 2.9 to 4.5 nm show an intense resonance (red dots) and on its low energy side a less intense peak (black dots) that corresponds, by comparison with PL resonance energies in Fig. 8.6(b), to the LE state. Another resonance is present in wells of width 3.2 and 4.5 nm (green dots) which can have several origins. It might be the 1S exciton of the ZnO C band

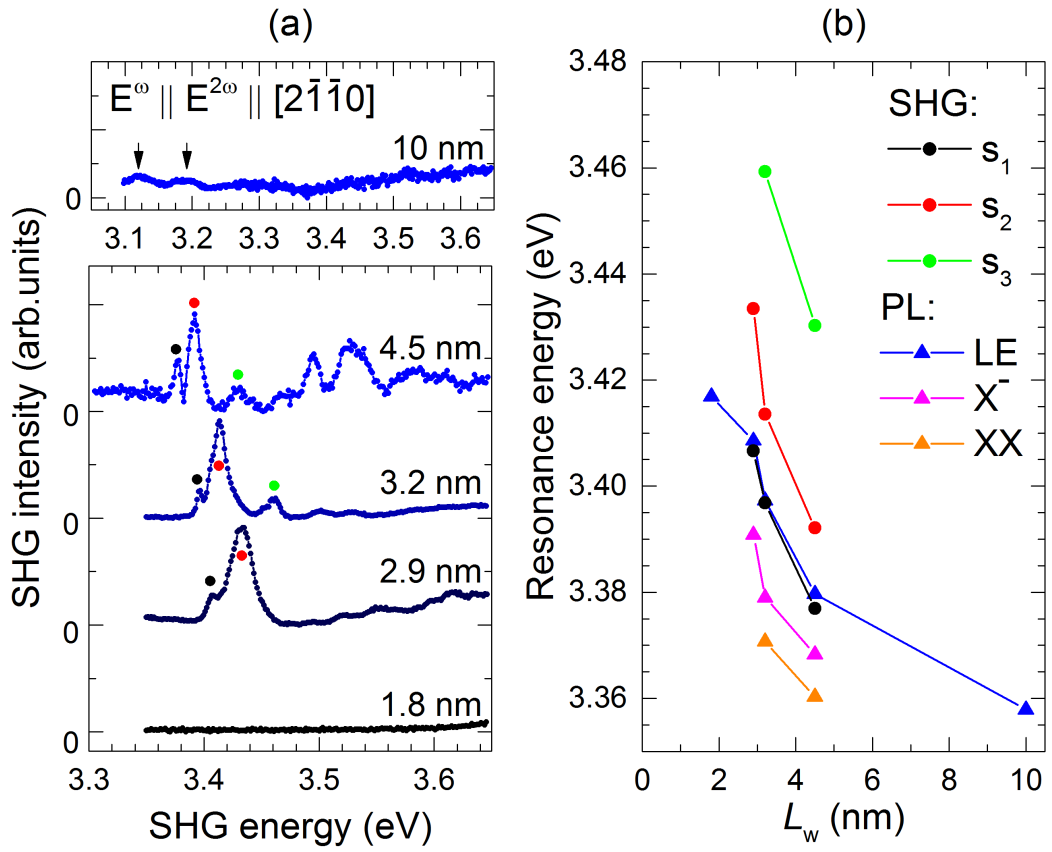

Figure 8.6: (a) SHG spectra of all quantum well samples for excitation ($\mathbf{E}^{\omega}$) and detection ($\mathbf{E}^{2\omega}$) polarization along crystal [2$\bar{1}\bar{1}$0] direction. Note the different energy scales in the upper and lower panel. Resonances are marked by coloured dots and plotted in (b) according to well width L_w against energy.

transition, the 2S state of the A transition, the light hole exciton, or the A 1S of the next quantized energy level. SHG signal increases slightly at energies above 3.5 eV for samples with $L_w \geqslant 2.9$ nm.

A direct comparison of the SHG and PL spectra of the 3.2 nm MQW is given in Fig. 8.7(a). No resonances of trion or bi-exciton are detected in SHG, whereas the LE state is observed and broader resonances at 3.4168 eV and 3.4640 eV, labelled by a and b, respectively. In the energy range of $3.50-3.55$ eV, two more resonances are present in SHG and PL spectra. Particularly by the observation in the PL spectrum, these could be assigned to lowest barrier states. In panels (b-d), the parallel and crossed rotational anisotropies of the SHG resonances LE, a and b are shown. The parallel anisotropies in panels (b) and (c) are tilted from the [2$\bar{1}\bar{1}$0] direction and differ in their crossed anisotropies, the parallel anisotropy in panel (d) is colinear to that crystal direction.

An analysis of the anisotropies is carried out in Sec. 8.5.

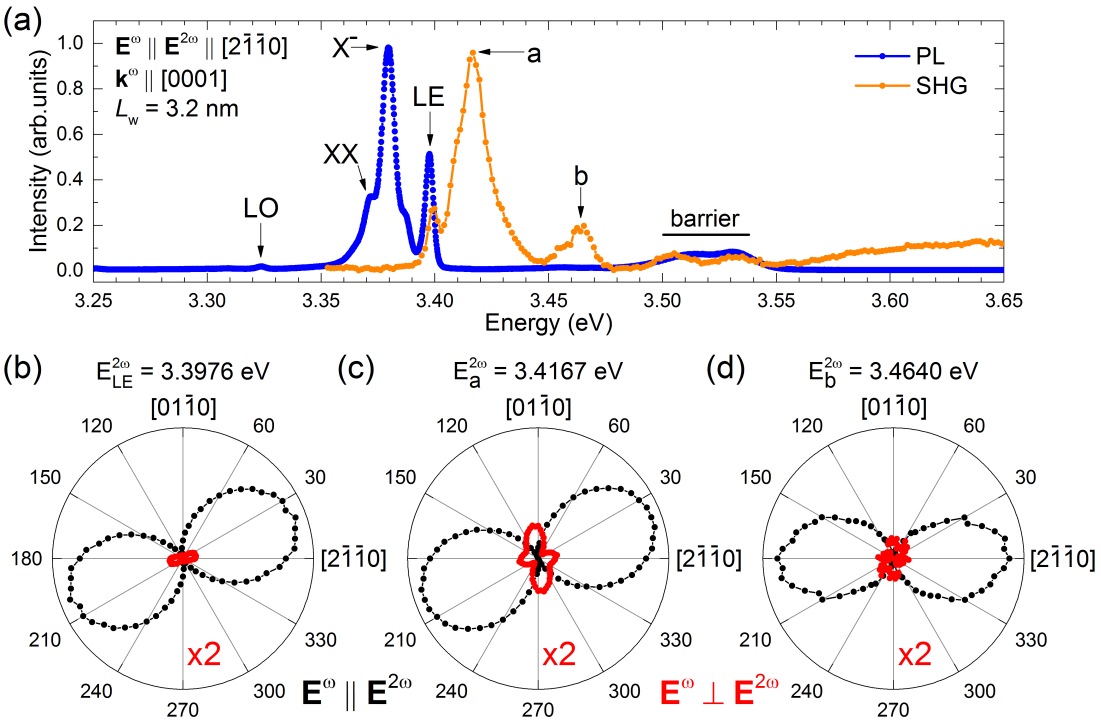

Figure 8.7: (a) Comparison of PL (blue) and SHG (orange) spectra of the 3.2 nm well width MQW sample. (b-d): Parallel (black) and crossed (red) SHG rotational anisotropies of resonances LE, a and b, as indicated in (a).

The possibility of SHG signal from the ZnMgO barriers is considered by measurements on a 590 nm thick $Zn_{0.9}Mg_{0.1}O$-layer (sample: 2261-MZO), grown on sapphire substrate. As no signal is observed in the layer, a contribution from the ZnMgO barriers, other than the signal in Fig. 8.7(a), in the MQW samples to the SHG spectrum can be excluded.

So far, for all measurements in this chapter the light **k**-vector was chosen to impinge perpendicularly at the crystal surface, i.e. $\mathbf{k}^{\omega} \parallel [0001]$. For this normal incidence geometry, no SHG signal should be detectable, as will be derived in Sec. 8.5. As soon as the sample is tilted by the angle θ around the vertical laboratory axis, SHG becomes allowed [Fig.8.8(d)]. Note, that the external tilting angle is divided by its index of refraction inside the crystal.

In Fig. 8.8, the SHG signal from the 3.2 nm well width sample, tilted by $\theta_{\mathrm{int}} = 13°$ (internal angle) around the vertical laboratory axis, is shown and compared to the signal for light incidence perpendicular to the sample surface. The SHG signal in tilted geometry is 40 times more intense than in normal incidence. In the inset, an anisotropy, representative for the whole SHG spectrum in tilted geometry, is plotted as well. It

shows different shape than in normal incidence [Fig. 8.7(b-d)]. Resonances a and b are resolved in both spectra, whereas the signal at energies above 3.48 eV is more pronounced in tilted geometry.

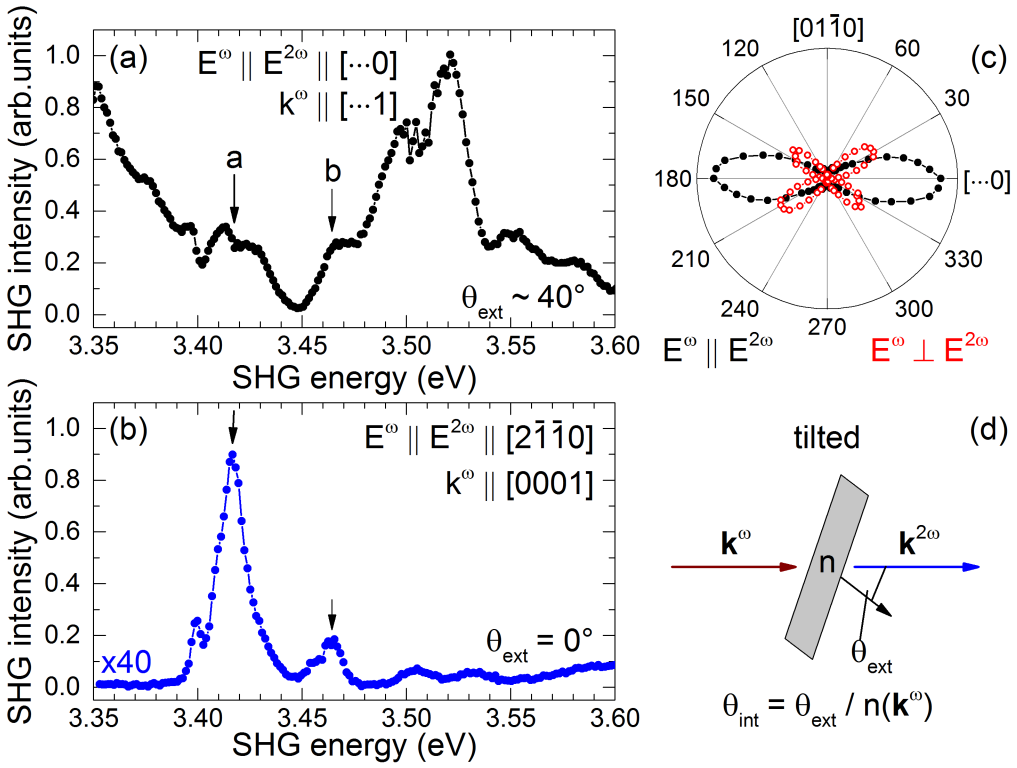

Figure 8.8: Comparison of (a): the sample normal vector tilted by $\theta_{ext} = 40°$ with respect to the laser $\mathbf{k}^\omega$ vector (black) and (b): SHG spectrum with the laser incident perpendicularly to the sample surface (blue). The rotational anisotropy of SHG in tilted geometry is presented in (c). It is representative for the whole spectrum in (a). Filled black and open red circles represent data for the $\mathbf{E}^\omega \parallel \mathbf{E}^{2\omega}$ and $\mathbf{E}^\omega \perp \mathbf{E}^{2\omega}$ configurations, respectively. The definition of external and internal angles is shown in (d).

8.5 Symmetry analysis

The discussion of symmetries is started in terms of the point group C_{6v} (6mm) of ZnO. The c-axis is set parallel to the crystal z-direction, [0001]. As the lattice is hexagonal, the **x**- and **y**-direction correspond to $[2\bar{1}\bar{1}0]$ and $[01\bar{1}0]$, respectively [21]. The A-, B- and C-valence bands are described by Γ_7, Γ_9 and Γ_7 and the conduction band by Γ_7 symmetry, see Fig. 8.1(b). Therefore, the irreducible representations of S-excitons with

holes from the respective valence bands are,

$$\begin{aligned} S_{\mathrm{A}} : \Gamma_7 \otimes \Gamma_7 \otimes \Gamma_1 &= \Gamma_1 \oplus \Gamma_2 \oplus \Gamma_5, \\ S_{\mathrm{B}} : \Gamma_7 \otimes \Gamma_9 \otimes \Gamma_1 &= \Gamma_5 \oplus \Gamma_6, \\ S_{\mathrm{C}} : \Gamma_7 \otimes \Gamma_7 \otimes \Gamma_1 &= \Gamma_1 \oplus \Gamma_2 \oplus \Gamma_5, \end{aligned} \tag{8.2}$$

with forbidden pure spin-triplet states plotted in red. P-exciton states with spin-singlet contributions are

$$\begin{aligned} P_{\mathrm{A}} &= \Gamma_1 \oplus \Gamma_6, \\ P_{\mathrm{B}} &= \Gamma_1 \oplus \Gamma_6, \\ P_{\mathrm{C}} &= \Gamma_5. \end{aligned} \tag{8.3}$$

In C_{6v}, a photon can be polarized along the crystal z-axis (Γ_1), or perpendicular to it in the xy-plane ($\Gamma_{5(\mathrm{x,y})}$). Therefore, one and two photons in electric-dipole approximation can excite states of the following symmetries:

$$\begin{aligned} \text{one dipole} \quad &: \quad \Gamma_{5(\mathrm{x,y})}, \quad \Gamma_1, \\ \text{two dipoles} \quad &: \quad \Gamma_{5(\mathrm{x,y})} \otimes \Gamma_{5(\mathrm{x,y})} = \Gamma_1 \oplus \Gamma_2 \oplus \Gamma_6 \\ &\quad\;\; \Gamma_{5(\mathrm{x,y})} \otimes \Gamma_1 = \Gamma_{5(\mathrm{x,y})} \\ &\quad\;\; \Gamma_1 \otimes \Gamma_1 = \Gamma_1 \end{aligned} \tag{8.4}$$

In the case of light incident along the crystal [0001]-axis (z-direction), the light has to be polarized perpendicularly to it, i.e. photons are represented by Γ_5. From Eqs. (8.2-8.4) it is deduced that in this geometry S-excitons are only one-photon dipole-allowed, whereas P-states are allowed for two-photon excitation. However, as soon as the sample is tilted, as was done in Fig. 8.8(a), the polarization of the incident photons is partly projected to the crystal z-axis, corresponding to Γ_1 symmetry. This allows for two-photon excitation of Γ_5 excitons and one-photon emission of Γ_1 photons. The simulation of the rotational anisotropy for tilted geometry is shown in Fig. 8.9. The simulated SHG pattern for the Γ_1 exciton, (b), resembles the measurement, despite lower intensity for the crossed configuration. In the simulation for the Γ_5 exciton, the crossed signal is missing and the parallel shape is broader than in the experimental data.

Anisotropies for $\mathbf{k}^{\omega} \parallel \mathbf{z}$, are shown in Fig. 8.7(b−d). As ZnO is described by the point group C_{6v}, no SHG is allowed for this configuration. Also the reduction to a quantum well structure, grown along the crystal c-axis and an internal electric field parallel to this axis do not impose a change to the overall symmetry. Possible explanations for the observed SHG signals might be exciton mixing by strain, induced by the interfaces between wells and barriers. By the internal electric field along the **z**-direction, excitons polarized in the xy-plane could be tilted slightly to the **z**-direction and be thereby mixed to the z-state.

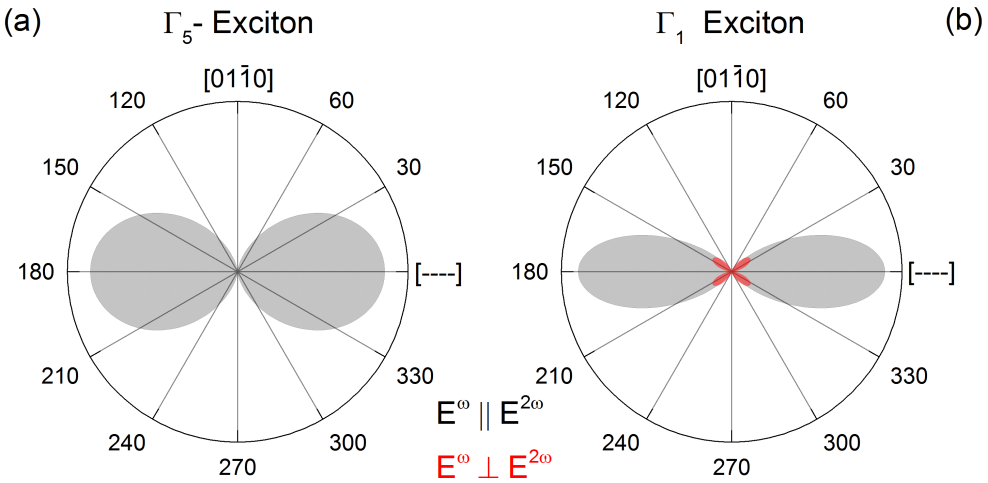

Figure 8.9: Simulated rotational anisotropies for ZnO in tilted geometry. Excitation and emission by (a) a Γ_5 and (b) Γ_1 exciton state. No crystal axis is given for 0° due to the tilted sample around the vertical axis. Grey and red shaded areas show the simulated pattern for the configurations $\mathbf{E}^{\omega} \parallel \mathbf{E}^{2\omega}$ and $\mathbf{E}^{\omega} \perp \mathbf{E}^{2\omega}$, respectively.

8.6 Conclusions

In the first step, the resonances in a set of ZnO/$Zn_{0.9}Mg_{0.1}$O-MQW samples are characterized by PL measurements. Thereby, the energies of the localized exciton, trion and bi-exciton are determined. The influence of internal electric fields by the piezoelectric effect is present mainly in the 10 nm quantum well sample. To be observable in narrower wells, the barrier Mg-concentration and therefore interlayer strain is too low.

In the second step, SHG measurements are performed on the MQW samples. Intense signal is found for wells of $2.9 - 4.5$ nm while almost no intensity is present in the 10 nm wells sample. This hints again at the effect of internal electric fields that separate electron and hole of the exciton, thereby reducing its oscillator strength.

Rotational anisotropies reveal different patterns for measurements in normal incidence ($\mathbf{k}^{\omega} \parallel [0001]$) and tilted ($\mathbf{k}^{\omega} \nparallel [0001]$) sample geometry. Whereas the anisotropy for tilted sample is explained by group theory, the shapes for normal incidence need further investigation. Additional application of an magnetic field might give insight into relevant symmetries. Another approach can be the strain-induced mixing of exciton states which requires an adaption of the theory for strain in Cu_2O, see Sec. 5.5. Also the internal electric field might have an effect, despite not changing the crystal symmetry directly, e.g. tilting an exciton that is polarized in the xy-plane slightly into the **z** direction.

9 Conclusions

The use of spectrally broad femtosecond laser pulses for fast and high resolution ($\geqslant$ 30 μeV) detection of SHG and THG spectra is introduced as a new measurement protocol. SHG-experiments are performed on the model semiconductor Cu_2O of highest possible crystal symmetry. It is known to reveal P-exciton states of particularly high principal quantum number n in linear optics experiments. The same holds true for SHG measurements presented here. As complementary selection rules, compared to linear optics, are active for SHG, S- and D-exciton states are detected up to $n = 9$. Still, it is not completely understood what the prerequisites for successful fs-nonlinear spectroscopy are. Whereas spectra of high resolution are obtained in Cu_2O (yellow series), ZnSe, CdTe, GaAs, Cr_2O_3 and perovskites, no such results are seen in ZnO, CuCl and $KNiF_3$. One might speculate that exciton-polariton lifetimes and their coherence properties, such as coherence length and time are of importance. Also intermediate states in the processes of SHG and THG could influence linewidths in the spectra.

A new approach for the measurement of exciton lifetimes using SHG in combination with a magnetic field is presented. Results for the relatively long lived 1S exciton in Cu_2O are in agreement with reported values. Difficulties occur due to mixing of the exciton components by magnetic field and in the special case of the 1S by internal strain. Despite these complications, also the question remains, whether the exciton lifetime is determined, or rather its coherence time.

The appearance of SHG signal at the 1S exciton resonance in Cu_2O in symmetry forbidden crystal directions is clarified by careful analysis of rotational anisotropies. Internal local strain is found to be the origin of this finding. Parameters of the strain tensor and related energy splitting of the 1S exciton are determined of the order of 10^{-6} in several crystal directions. By this, energy splittings of a few μeV are obtained, which is a challenging task also in linear optics.

Measurements on ZnSe bulk material reveal a 4 meV shift of the 1S exciton resonance towards higher energy in SHG as compared to linear spectra. This is explained by inclusion of the exciton-polariton dispersion. Depending on laser light wavelength and corresponding index of refraction, different points of the dispersion are probed. Therefore, SHG and THG resonance energies allow for a primitive form of k-space spectroscopy with application of only one laser beam.

Nevertheless, ZnSe seems to be particularly suited to study the polariton-dispersion at the 1S exciton by SHG and THG. Similar materials of T_d symmetry have smaller exciton binding energies, e.g. CdTe (10 meV) and GaAs (4 meV), leading to lower oscillator strength and close lying higher S-states. ZnO, on the other hand, has an exciton binding energy of 60 meV that should give a larger polariton shift. However, due to the C_{6v} wurtzite structure, S-excitons are only observable weakly in tilted geometry, or

in applied magnetic field in SHG. Finally, Cu_2O has a high exciton binding energy of 150 meV. Still, no polariton shift can be observed in SHG [Sec. 5]. This hints at a small oscillator strength due to the necessary quadrupole emission from the S-exciton state, i.e. oscillator strength is **k**-dependent.

Exciton states are detected and analyzed in type-II ZnSe/BeTe and type-I ZnO/$Zn_{0.9}Mg_{0.1}O$ heterostructures. SHG and THG spectra, in combination with linear reflectivity and PL measurements, allow for peak identification. In ZnSe/BeTe, SHG is induced by a magnetic field. Thereby, the symmetry of the structure is reduced to C_{2v}, as is deduced from rotational anisotropies. In tilted geometry, SHG is generated in the GaAs substrate of the sample, in principle, allowing for measuring one-photon absorption of the quantum wells.

In the $ZnO/Zn_{0.9}Mg_{0.1}O$ samples of varying well widths, the effect of quantum confinement is observed, as well as the influence of the piezoelectric effect due to strain from the layer interfaces. The samples are characterized by linear and nonlinear spectra wherein the exciton, trion and bi-exciton are observed.

Appendices

A Laser system problems

Common problems of the LC-laser system and possible solutions are summarized in this section.

PulsePicker high-voltage Sometimes the PulsePicker high-voltage has to be switched on manually. This is the case if there is no output from the OPAs and no green light is emitted by the SHBC. To switch it on, the field "PP HV Supply" in the RA panel in the main laser programme has to be clicked. In the new window, the message "Last error: Voltage too high" is shown. By clicking the field "Turn On" the laser system should work again.

Low OPA output power After changing the output wavelength of an OPA by more than a few nm, or changing laboratory environment conditions, the output power can be low. In that case, it is necessary to readjust the ingoing OPA beams by mirrors PVBS and BRM9 (fs-OPA), or by BRM6 and BRM8 (ps-OPA), see Fig. 3.3. Care has to be taken, to adjust only the screws on the diagonal of the BRMs. While measuring the output power, the screws should be turned carefully alternating one after another until maximum power is achieved.

At rare occasions, it might be necessary to adjust the beam path inside the SHBC. For this action, the manual has to be consulted.

Unstable OPA output power This problem concerns rather the ps-OPA, but can occur with the fs-OPA as well. Usually, it is solved by adjusting the input beam paths until maximum output power is achieved. Another possibility is to open the corresponding OPA and rotate the crystal for white light generation a bit further (see the manual).

Wrong output wavelength When changing the USB-cable of an OPA from one computer to another, the TOPAS programmes must be set to the same wavelength. The reason is that the physical wavelength which is set at computer 1, is kept, but at computer 2 a different value is set in the programme. If the initialization files are present at the computer, the motors inside the OPA can be resetted in the "Win TOPAS 3" programme to obtain the correct wavelength. Therefore, the field "Motors" has to be clicked, followed by "Direct Access". Here, "Reset" has to be clicked for each motor.

B Group theory

In this chapter, the full group theoretical analysis of a transition is given. To apply group theory, knowledge about the crystal symmetry and the corresponding tables, e.g. in the book by Koster *et al.* [33], is sufficient. The procedure is demonstrated for the 1S exciton transition in Cu_2O with point group O_h.

Symmetries of electron bands In Cu_2O, the valence (conduction) band originates from the 3d (4s) copper orbital which implies an orbital momentum of $l = 2$ (0). This corresponds to an irreducible representation, Γ_i, in the O_h group. All assignments of momenta are listed in the *Full Rotation Group Compatibility Table*. Thus, the valence band is split by the crystal field into a Γ_3^+ and Γ_5^+ band. The superscript indicates the parity, which is a good quantum number in O_h, of the representation. Note, that the total number of dimensions is maintained in all operations. Therefore, the five-dimensional $l = 2$ orbital has to be represented by symmetries of dimension five in total. The dimension of each Γ_i is found in the first column, E, of the *Character Table*. From group theory, the energetic order of the bands is not determined. However, experiments yielded higher energy for the Γ_5^+ band which is therefore the uppermost valence band. The conduction band is described by Γ_1^+.

In the next step, the spin is coupled to the bands. The electron spin is 1/2 and of positive parity, transforming as Γ_6^+. The results of tensor products can be obtained from the *Multiplication Table* of a group. Therefore, the conduction band has symmetry $\Gamma_1^+ \otimes \Gamma_6^+ = \Gamma_6^+$ and the valence band $\Gamma_5^+ \otimes \Gamma_6^+ = \Gamma_7^+ \oplus \Gamma_8^+$. Again, the Γ_7^+ band was determined to have higher energy.

Symmetries of excitons The symmetry of excitons is the product of the irreducible representations of the conduction band of the participating electron, valence band of the hole and exciton envelope function, see Eq. (2.29). To evaluate the spin-structure of the exciton states, it is necessary to calculate the spin orientations of the bands instead of just multiplying their symmetries. The structure of the conduction band is

$$\Gamma_1^+ \otimes \Gamma_6^+ \longrightarrow \Gamma_6^+ = \begin{pmatrix} \uparrow \\ \downarrow \end{pmatrix}, \tag{B.1}$$

and for the Γ_7^+ valence band

$$\Gamma_5^+ \otimes \Gamma_6^+ \longrightarrow \Gamma_7^+ = \frac{1}{\sqrt{3}} \begin{pmatrix} \Gamma_{5xz}^+ \downarrow -i \left(\Gamma_{5yz}^+ \downarrow + \Gamma_{5xy}^+ \uparrow \right) \\ -\Gamma_{5xz}^+ \uparrow + i \left(\Gamma_{5xy}^+ \downarrow - \Gamma_{5yz}^+ \uparrow \right) \end{pmatrix}. \tag{B.2}$$

The full symmetry of the 1S exciton is given by

$$\Gamma_{\mathrm{exc}} = \Gamma_6^+ \otimes \Gamma_7^+ = \Gamma_2^+ \oplus \Gamma_5^+, \tag{B.3}$$

with explicit forms

$$\Gamma_2^+ = \frac{1}{\sqrt{6}} \left(-\Gamma_{5\mathrm{xz}}^+ (\uparrow\uparrow + \downarrow\downarrow) + i\Gamma_{5\mathrm{xy}}^+ (\uparrow\downarrow + \downarrow\uparrow) - i\Gamma_{5\mathrm{yz}}^+ (\uparrow\uparrow - \downarrow\downarrow) \right), \tag{B.4}$$

$$\Gamma_5^+ = \frac{i}{\sqrt{6}} \begin{pmatrix} \Gamma_{5\mathrm{xz}}^+ (\uparrow\downarrow + \downarrow\uparrow) - i\Gamma_{5\mathrm{xy}}^+ (\uparrow\uparrow + \downarrow\downarrow) - i\Gamma_{5\mathrm{yz}}^+ (\uparrow\downarrow - \downarrow\uparrow) \\ -i \left[\Gamma_{5\mathrm{xz}}^+ (\uparrow\downarrow - \downarrow\uparrow) - i\Gamma_{5\mathrm{xy}}^+ (\uparrow\uparrow - \downarrow\downarrow) - i\Gamma_{5\mathrm{yz}}^+ (\uparrow\downarrow + \downarrow\uparrow) \right] \\ - \left[\Gamma_{5\mathrm{xz}}^+ (\downarrow\downarrow - \uparrow\uparrow) - i\Gamma_{5\mathrm{xy}}^+ (\downarrow\uparrow - \uparrow\downarrow) - i\Gamma_{5\mathrm{yz}}^+ (\downarrow\uparrow + \uparrow\uparrow) \right] \end{pmatrix}. \tag{B.5}$$

From Eqs. (B.4) and (B.5) it gets clear that only exciton states of Γ_5^+ symmetry contain singlet, i.e. $(\uparrow\downarrow - \downarrow\uparrow)$, contributions that are optically excitable.

In the case of a four-dimensional band, e.g. the Γ_8 valence band in ZnSe, heavy and light holes of spin $\pm 3/2$ and $\pm 1/2$ have to be considered. However, the overall principle remains the same.

Symmetries of photons The symmetry of a photon in dipole, or quadrupole approximation is deduced from Eq. (2.16). An electric dipole corresponds to V_{D} which is basically the momentum operator $\mathbf{p}$. This transforms like a vector, i.e. as the basis functions x, y and z. They are represented in O_h by Γ_4^- symmetry.

The next higher order, the electric quadrupole and magnetic dipole, is the scalar product of light vector $\mathbf{k}$ and momentum $\mathbf{p}$. Both transform like a vector, resulting in the tensor-product

$$\Gamma_4^- \otimes \Gamma_4^- = \Gamma_1^+ \oplus \Gamma_3^+ \oplus \Gamma_4^+ \oplus \Gamma_5^+. \tag{B.6}$$

From these four, only Γ_3^+ and Γ_5^+ are non-zero.

Now the polarization dependence of the whole SHG process, comprising the two-photon excitation and one-photon emission, can be calculated. In the case of Cu_2O, this is done in Sec. 5.5 for four $\mathbf{k}$-directions. The two-photon excitation is described by the operator O_{TPDD} and the one-photon emission by O_{D}.

Transitions at $\mathbf{k} \neq 0$ So far, only exciton transitions at the Γ-point, the centre of the Brillouin zone ($\mathbf{k} = 0$), were considered. If this is not the case, e.g. in perovskites where the transition of lowest energy is located at $\mathbf{k} = [111]$, the R-point [128], the point group of the material can be reduced. Information on that topic can be found in Ref. [129].

C Mathematica

In this chapter, a minimal example of Mathematica-code is presented which is used to simulate rotational anisotropies. The example can be used for S-excitons in the geometry $\mathbf{k}^{\omega} \parallel [111]$ in Cu_2O.

Define the arbitrary rotation matrix T in three dimensions with a rotation of "theta" radians around an "axis":

$$T[\text{axis\_, theta\_}] \tag{C.1}$$

Define the normalized crystal vectors:

$$\text{xcrys} := \frac{1}{\sqrt{2}} * \{1, -1,0\}, \quad \text{ycrys} := \frac{1}{\sqrt{6}} * \{1,1, -2\}, \quad \text{zcrys} := \frac{1}{\sqrt{3}} * \{1,1,1\} \tag{C.2}$$

The light $\mathbf{k}$-direction is defined parallel to $\mathbf{z}$:

$$\text{k} := \text{zcrys} \tag{C.3}$$

The polarization Pol is turned by an angle "phi" around "k" with zero angle corresponding to xcrys:

$$\text{Pol[phi\_]} := T[\text{k, phi}].\text{xcrys} \tag{C.4}$$

One photon in dipole approximation, El1Dipole, is defined as:

$$\text{El1Dipole[phi\_]} := \{\text{Pol[phi][[1]]},\text{Pol[phi][[2]]},\text{Pol[phi][[3]]}\} \tag{C.5}$$

The S-exciton is excited by two photons in dipole approximation, El2Dipole:

$$\begin{aligned} \text{El2Dipole[phi\_]} := (\sqrt{2}) \quad * \quad & \{\text{Pol[phi][[2]]} * \text{Pol[phi][[3]]}, \\ & \text{Pol[phi][[1]]} * \text{Pol[phi][[3]]}, \\ & \text{Pol[phi][[1]]} * \text{Pol[phi][[2]]}\} \end{aligned} \tag{C.6}$$

One photon in electric quadrupole approximation, El1Quad, which is emitted from S-excitons, is defined as:

$$\begin{aligned} \text{El1Quad[phi\_]} := \frac{1}{\sqrt{2}} \quad * \quad & \{\text{k[[2]]} * \text{Pol[phi][[3]]} + \text{k[[3]]} * \text{Pol[phi][[2]]}, \\ & \text{k[[1]]} * \text{Pol[phi][[3]]} + \text{k[[3]]} * \text{Pol[phi][[1]]}, \\ & \text{k[[1]]} * \text{Pol[phi][[2]]} + \text{k[[2]]} * \text{Pol[phi][[1]]}\} \end{aligned} \tag{C.7}$$

The full anisotropy, with ingoing and outgoing polarizations "phiIn" and "phiOut", is given by:

$$\text{Sexc[phiIn\_, phiOut\_]} := (\text{El1Quad[phiOut\_]}.\text{El1Dipole[phiIn\_]})^2 \tag{C.8}$$

Formulas, e.g. for the parallel and crossed configurations, are printed by:

$$\begin{aligned} &\text{FullSimplify[Sexc[phi, phi]]} \\ &\text{FullSimplify[Sexc[phi, phi + } \pi/2\text{]]} \end{aligned} \tag{C.9}$$

A polar plot of the anisotropies is shown by:

$$\text{PolarPlot[\{Sexc[phi, phi], Sexc[phi, phi + } \pi/2\text{]\},\{phi,0,2}\pi\text{\}]} \tag{C.10}$$

Bibliography

[1] Y. R. Shen. *The principles of Nonlinear Optics.* Wiley, New York, 1984.

[2] R. W. Boyd. *Nonlinear Optics.* 3rd ed, Academic Press, online resource, 2008.

[3] T. H. Maiman. "*Stimulated Optical Radiation in Ruby*". *Nature* **187** (1960), p. 493.

[4] P. A. Franken, A. E. Hill, C. W. Peters, and G. Weinreich. "*Generation of Optical Harmonics*". *Phys. Rev. Lett.* **7** (1961), p. 118.

[5] W. Kaiser and C. G. B. Garrett. "*Two-Photon Excitation in CaF_2:Eu^{2+}*". *Phys. Rev. Lett.* **7** (1961), p. 229.

[6] J. J. Hopfield, J. M. Worlock, and K. Park. "*Two-quantum absorption spectrum of KI*". *Phys. Rev. Lett.* **11** (1963), p. 414.

[7] H. Mahr. *Two-photon absorption spectroscopy.* Quantum Electronics **1A**, p. 285, eds. H. Rabin and C. L. Tang (Academic Press, New York, 1975).

[8] M. Göppert-Mayer. "*Über Elementarakte mit zwei Quantensprüngen*". *Ann. der Phys.* **401** (1931), p. 273.

[9] D. Fröhlich. *Aspects of Nonlinear Spectroscopy.* Festkörperprobleme (Advances in Solid State Physics), Volume XXI, 363, J.Treusch (ed.), Vieweg, Braunschweig, 1981.

[10] R. C. Prince, R. R. Frontiera, and E. O. Potma. "*Stimulated Raman Scattering: From Bulk to Nano*". *Chem. Rev.* **117** (2017), p. 5070.

[11] R. P. Seisyan. "*Diamagnetic Excitons in Semiconductors (Review)*". *Phys. Solid State* **58** (2016), p. 859.

[12] D. R. Yakovlev, V. V. Pavlov, A. V. Rodina, R. V. Pisarev, J. Mund, W. Warkentin, and M. Bayer. "*Exciton spectroscopy of semiconductors by the method of optical harmonics generation (review)*". *Phys. Solid State* **60** (2018), p. 1471.

[13] I. Sänger. *Magnetic-Field-Induced Second Harmonic Generation in Semiconductors and Insulators.* PhD thesis, U Dortmund, 2006.

[14] B. Kaminski. *New Mechanisms of Optical Harmonic Generation in Semiconductors.* PhD thesis, TU Dortmund, 2009.

[15] M. Lafrentz. *Magnetic Field Induced Optical Harmonic Generation in the Semiconductors ZnO and EuX.* PhD thesis, TU Dortmund, 2013.

[16] D. S. Brunne. *Optical harmonic generation at exciton resonances in GaAs, GaN, and Cu_2O semiconductors.* PhD thesis, TU Dortmund, 2014.

[17] E. L. Ivchenko and G. E. Pikus. *Superlattices and Other Heterostructures.* 2nd ed., Springer, Berlin, 1997.

[18] L. Esaki and R. Tsu. "*Superlattice and negative differential conductivity in semiconductors*". *IBM J. Res. Devel.* **14** (1970), p. 61.

[19] K. v. Klitzing, G. Dorda, and M. Pepper. "*New Method for High-Accuracy Determination of the Fine-Structure Constant Based on Quantized Hall Resistance*". *Phys. Rev. Lett.* **45** (1980), p. 494.

[20] J. Faist, F. Capasso, D. L. Sivco, C. Sirtori, A. L. Hutchinson, and A. Y. Cho. "*Quantum Cascade Laser*". *Science* **264** (1994), p. 553.

[21] R. R. Birss. *Symmetry and magnetism.* North-Holland Publ. Comp., Amsterdam, 1964.

[22] S. V. Popov, Yu. P. Svirko, and N. I. Zheludev. *Susceptibility Tensors for Nonlinear Optics.* The Institude of Physics, London, 1995.

[23] R. Loudon. *The quantum theory of light.* 2. ed, Clarendon Pr, Oxford, 1983.

[24] P. Y. Yu and M. Cardona. *Fundamentals of Semiconductors.* Springer-Verlag Berlin Heidelberg, 2001.

[25] J. Frenkel. "*On the Transformation of light into Heat in Solids. I*". *Phys. Rev.* **37** (1931), p. 17.

[26] G. H. Wannier. "*The Structure of Electronic Excitation Levels in Insulating Crystals*". *Phys. Rev.* **52** (1937), p. 191.

[27] U. Fano. "*Atomic Theory of Electromagnetic Interactions in Dense Materials*". *Phys. Rev.* **103** (1956), p. 1202.

[28] J. J. Hopfield. "*Theory of the Contribution of Excitons to the Complex Dielectric Constant of Crystals*". *Phys. Rev.* **112** (1958), p. 1555.

[29] L. C. Andreani. "*Exciton-polaritons in bulk semiconductors and in confined electron and photon systems*". *Phys. Rev.* **132** (2013), p. 563.

[30] C. Klingshirn. *Semiconductor Optics.* 2nd ed, Springer-Verlag Berlin Heidelberg, 2007.

[31] M. S. Dresselhaus, G. Dresselhaus, and A. Jorio. *Group Theory, Application to the Physics of Condenced Matter.* Springer-Verlag Berlin Heidelberg, 2008.

[32] D. W. Snoke. *Solid State Physics, Essential Concepts.* Pearson Education, Inc., publishing as Addison-Wesley, 2009.

[33] G. F. Koster, J. O. Dimmock, R. G. Wheeler, and Hermann Statz. *Properties of the thirty-two point groups.* M.I.T. Press, Cambridge, Massachusetts, 1963.

[34] D. Strickland and G. Mourou. "*Compression of amplified chirped optical pulses*". *Opt. Commun.* **55** (1985), p. 447.

[35] National Institute of Standards and Technology. *NIST Atomic Spectra Database Lines Form.* Mar. 2019. URL: `https://physics.nist.gov/PhysRefData/ASD/lines_form.html`.

[36] B. Edlén. "*The Refractive Index of Air*". *Metrologia* **2** (1966), p. 71.

[37] Teledyne Princeton Instruments. *Teledyne Princeton Instruments*. July 2019. URL: `https://www.princetoninstruments.com/products/PyLoN-CCD`.

[38] V. N. Gridnev, V. V. Pavlov, R. V. Pisarev, A. Kirilyuk, and Th. Rasing. "*Second harmonic generation in anisotropic magnetic films*". *Phys. Rev. B* **63** (2001), p. 184407.

[39] D. Fröhlich and K. Reimann. "*Two-photon K-space spectroscopy to determine the mixed-mode polariton dispersion in $AgGaS_2$*". *Physica B+C* **117-118** (1983), p. 392.

[40] L. Hanke, J. Uhlenhut, D. Fröhlich, and H. Stolz. "*Time-Resolved Stimulated Two-Photon Emission in Cu_2O*". *Phys. Status Solidi B* **206** (1998), p. 65.

[41] C. Rullière. *Femtosecond Laser Pulses: Principles and Experiments*. Springer Verlag, 2005.

[42] J.-C. Diels. *Ultrashort laser pulse phenomena*. Academic Press Limited, London, 1995.

[43] K. Zhao, Q. Zhang, M. Chini, Y. Wu, X. Wang, and Z. Chang. "*Tailoring a 67 attosecond pulse through advantageous phase-mismatch*". *Opt. Lett.* **37** (2012), p. 3891.

[44] E. F. Gross and I. A. Karryjew. "*The optical spectrum of the exciton*". *Dokl. Akad. Nauk. SSSR* **84** (1952), p. 471.

[45] H. Matsumoto, K. Saito, M. Hasuo, S. Kono, and N. Nagasawa. "*Revived interest on yellow-exciton series in Cu_2O*". *Solid State Commun.* **97** (1996), p. 125.

[46] T. Kazimierczuk, D. Fröhlich, S. Scheel, H. Stolz, and M. Bayer. "*Giant Rydberg excitons in the copper oxide Cu_2O*". *Nature* **514** (2014), p. 343.

[47] M. Y. Shen, S. Koyama, M. Saito, T. Goto, and N. Kuroda. "*Second-harmonic generation resonant to the 1S orthoexciton level of cuprous oxide*". *Phys. Rev. B* **53** (1996), p. 13477.

[48] R. J. Elliott. "*Symmetry of Excitons in Cu_2O*". *Phys. Rev.* **124** (1961), p. 340.

[49] F. Schweiner, J. Main, G. Wunner, and Ch. Uihlein. "*Even exciton series in Cu_2O*". *Phys. Rev. B* **95** (2017), p. 195201.

[50] Ch. Uihlein, D. Fröhlich, and R. Kenklies. "*Investigation of exciton fine structure in Cu_2O*". *Phys. Rev. B* **23** (1981), p. 2731.

[51] G. Dasbach, D. Fröhlich, R. Klieber, D. Suter, M. Bayer, and H. Stolz. "*Wave-Vector-Dependent exchange interaction and its relevance for the effective exciton mass in Cu_2O*". *Phys. Rev. B* **70** (2004), p. 045206.

[52] M. M. Glazov. *private communication*.

[53] D. Fröhlich and R. Kenklies. "*Polarization dependence of two photon magnetoabsorption of the 1S exciton in Cu_2O*". *Phys. Status Solidi B* **111** (1982), p. 247.

[54] D. Fröhlich, K. Reimann, and R. Wille. "*Time-resolved two-photon emission in Cu_2O*". *Europhys. Lett.* **3** (1987), p. 853.

[55] K. Yoshioka and M. Kuwata-Gonokami. "*Dark excitons in Cu_2Ocrystals for two-photon coherence storage in semiconductors*". *Phys. Rev. B* **73** (2006), 081202(R).

[56] R. G. Waters, F. H. Pollak, R. H. Bruce, and H. Z. Cummins. "*Effects of uniaxial stress on excitons in Cu_2O*". *Phys. Rev. B* **21** (1980), p. 1665.

[57] H.-R. Trebin, H. Z. Cummins, and J. L. Birman. "*Excitons in cuprous oxide under uniaxial stress*". *Phys. Rev. B* **23** (1981), p. 597.

[58] F. Schweiner, J. Main, M. Feldmaier, G. Wunner, and Ch. Uihlein. "*Impact of the valence band structure of Cu_2O on excitonic spectra*". *Phys. Rev. B* **93** (2016), p. 195203.

[59] J. I. Jang and J. P. Wolfe. "*Relaxation of stress-split orthoexcitons in Cu_2O*". *Phys. Rev. B* **73** (2006), p. 075207.

[60] G. Dasbach, D. Fröhlich, H. Stolz, R. Klieber, D. Suter, and M. Bayer. "*Wave-Vector-Dependent Exciton Exchange Interaction*". *Phys. Rev. Lett.* **91** (2003), p. 107401.

[61] A. Mysyrowicz, D. Hulin, and A. Antonetti. "*Long Exciton Lifetime in Cu_2O*". *Phys. Rev. Lett.* **43** (1979), p. 1123.

[62] K. Reimann and R. Wille. "*Temperature dependence of exciton lifetime in Cu_2O*". *J. Lumin.* **38** (1987), p. 60.

[63] J. I. Jang, K. E. O'Hara, and J. P. Wolfe. "*Spin-exchange kinetics of excitons in Cu_2O: Transverse acoustic phonon mechanism*". *Phys. Rev. B* **70** (2004), p. 195205.

[64] Ch. Uihlein. *private communication.*

[65] M. Freitag. *Hochauflösende Laserspektroskopie an 1S- und Rydberg-Exzitonen in Cu_2O in statischen und optischen Feldern.* M. Sc. thesis, TU Dortmund, 2016.

[66] Inc. Wolfram Research. *Mathematica.* Version 8.0. 2010. URL: `https://www.wolfram.com/mathematica/`.

[67] J. Heckötter, M. Freitag, D. Fröhlich, M. Aßmann, M. Bayer, P. Grünwald, F. Schöne, D. Semkat, H. Stolz, and S. Scheel. "*Rydberg Excitons in the Presence of an Ultralow-Density Electron-Hole Plasma*". *Phys. Rev. Lett.* **121** (2018), p. 097401.

[68] F. Schöne, H. Stolz, and N. Naka. "*Phonon-assisted absorption of excitons in Cu_2O*". *Phys. Rev. B* **96** (2017), p. 115207.

[69] D. Fröhlich, G. Dasbach, G. Baldassarri Höger von Högersthal, M. Bayer, R. Klieber, D. Suter, and H. Stolz. "*High resolution spectroscopy of yellow 1S excitons in Cu_2O*". *Solid State Commun.* **134** (2005), p. 139.

[70] A. Farenbruch. *Erzeugung der zweiten Harmonischen an Exzitonen in Cu_2O.* M. Sc. thesis, TU Dortmund, 2018.

[71] D. Fröhlich and H. Volkenandt. "*Determination of Γ_3 valence band in CuCl by two-photon absorption*". *Solid State Commun.* **43** (1982), p. 189.

[72] M. Aven, D. T. F. Marple, and B. Segall. "*Some electrical and Optical Properties of ZnSe*". *J. Appl. Phys.* **32** (1961), p. 2261.

[73] G. E. Hite, D. T. F. Marple, M. Aven, and B. Segall. "*Excitons and the Absorption Edge in ZnSe*". *Phys. Rev.* **156** (1966), p. 850.

[74] M. Sondergeld and R. G. Stafford. "*Exciton Fine Structure via Envelope-Hole Coupling in Cubic ZnSe*". *Phys. Rev. Lett.* **35** (1975), p. 1529.

[75] H. W. Hölscher, A. Nöthe, and Ch. Uihlein. "*Investigation of band masses and g values of ZnSe by two-photon magnetoabsorption*". *Phys. Rev. B* **31** (1985), p. 2379.

[76] D. W. Langer, R. N. Euwema, Koh Era, and Takao Koda. "*Spin Exchange in Excitons, the Quasicubic Model and Deformation Potentials in II-VI Compounds*". *Phys. Rev. B* **2** (1970), p. 4005.

[77] D. Fröhlich, W. Nieswand, U. W. Pohl, and J. Wrzesinski. "*Two-photon spectroscopy of ZnSe under uniaxial stress*". *Phys. Rev. B* **52** (1995), p. 14652.

[78] K. Reimann and M. Steube. "*Nonlinear Optical Spectroscopy of Semiconductors under Pressure*". *Phys. Status Solidi B* **211** (1998), p. 189.

[79] J. Mund. *Erzeugung der zweiten Harmonischen durch Anregung von Magneto-Exzitonen in ZnSe*. M. Sc. thesis, TU Dortmund, 2015.

[80] A. Mang, K. Reimann, and St. Rübenacke. *Proc. 22nd Int. Conf. Phys. Semicond.* Vancouver 1994, Lockwood, D. j. (ed.), World Scientific (Singapore), p. 317, 1995.

[81] O. Madelung. *Semiconductors - Basic Data*. Madelung, O. (ed.), 2nd ed. Springer-Verlag Berlin Heidelberg, p. 183, 1996.

[82] M. Wörz, E. Griebl, Th. Reisinger, R. Flierl, B. Haserer, T. Semmler, T. Frey, and W. Gebhardt. "*Gap energies, Exciton Binding Energies and Band Offsets in Ternary ZnMgSe Compounds and ZnSe/ZnMgSe Heterostructures*". *Phys. Status Solidi B* **202** (1997), p. 805.

[83] R. M. Park, C. M. Rouleau, M. B. Troffer, T. Koyama, and T. Yodo. "*Strain-free, ultra-high purity ZnSe layers grown by molecular beam epitaxy*". *J. Mater. Res.* **5** (1990), p. 475.

[84] U. W. Pohl, G. H. Kudlek, A. Klimakow, and A. Hoffmann. "*Shallow impurity- and defect-related complexes in undoped ZnSe crystals*". *J. Cryst. Growth* **138** (1994), p. 385.

[85] D. T. F. Marple. "*Refractive Index of ZnSe, ZnTe and CdTe*". *J. Appl. Phys.* **35** (1964), p. 539.

[86] S. Adachi and T. Taguchi. "*Optical properties of ZnSe*". *Phys. Rev. B* **43** (1991), p. 9569.

[87] W. Warkentin, J. Mund, D. R. Yakovlev, V. V. Pavlov, R. V. Pisarev, A. V. Rodina, M. A. Semina, M. M. Glazov, E. L. Ivchenko, and M. Bayer. "*Third harmonic generation on exciton-polaritons in bulk semiconductors subject to a magnetic field*". *Phys. Rev. B* **98** (2018), p. 075204.

[88] Y. Nozue, M. Itoh, and K. Cho. "*Excitonic Polariton Dispersion in ZnSe Determined by the Resonant Raman Scattering under Two-Photon Excitation of Excitonic Molecules*". *J. Phys. Soc. Japan* **50** (1981), p. 889.

[89] A. V. Platonov, D. R. Yakovlev, U. Zehnder, V. P. Kochereshko, W. Ossau, F. Fischer, Th. Litz, A. Waag, and G. Landwehr. "*Homogeneous linewidth of the direct exciton in a type-II ZnSe/BeTe quantum well*". *J. Cryst. Growth* **184/185** (1998), p. 801.

[90] S. V. Zaitsev, V. D. Kulakovskii, A. A. Maksimov, I. I. Tartakovskii, N. A. Gippius, M. Th. Litz, F. Fischer, A. Waag, D. R. Yakovlev, W. Ossau, and G. Landwehr. "*Giant blue shift of photoluminescence in strongly excited type-II ZnSe/BeTe superlattices*". *JETP Lett.* **66** (1997), p. 376.

[91] A. A. Maksimov, S. V. Zaitsev, I. I. Tartakovskii, D. R. Yakovlev, W. Ossau, M. Keim, G. Reuscher, A. Waag, and G. Landwehr. "*Kinetics of radiative recombination in strongly excited ZnSe/BeTe superlattices with a type-II band alignment*". *Appl. Phys. Lett.* **75** (1999), p. 1231.

[92] A. V. Platonov, V. P. Kochereshko, E. L. Ivchenko, G. V. Mikhailov, D. R. Yakovlev, M. Keim, W. Ossau, A. Waag, and G. Landwehr. "*Giant Electro-optical Anisotropy in Type-II Heterostructures*". *Phys. Rev. Lett.* **83** (1999), p. 3546.

[93] D. R. Yakovlev, E. L. Ivchenko, V. P. Kochereshko, A. V. Platonov, S. V. Zaitsev, A. A. Maksimov, I. I. Tartakovskii, V. D. Kulakovskii, W. Ossau, M. Keim, A. Waag, and G. Landwehr. "*Orientation of chemical bonds at type II heterointerfaces probed by polarized optical spectroscopy*". *Physical Review B* **61** (2000), R2421.

[94] S. V. Zaitsev, A. A. Maksimov, V. D. Kulakovskii, I. I. Tartakovskii, D. R. Yakovlev, W. Ossau, L. Hansen, G. Landwehr, and A. Waag. "*Interface properties and in-plane linear photoluminescence polarization in highly excited type-II ZnSe/BeTe heterostructures with equivalent and nonequivalent interfaces*". *J. Appl. Phys.* **91** (2002), p. 652.

[95] A. A. Maksimov, S. V. Zaitsev, E. V. Filatov, A. V. Larionov, I. I. Tartakovskii, D. R. Yakovlev, and A. Waag. "*Formation of Metastable Above-Barrier Hole States in ZnSe/BeTe Type II Heterostructures under High-Density Optical Excitation*". *JETP Lett.* **88** (2008), p. 511.

[96] M. Nagelstraßer, H. Dröge, H.-P. Steinrück, F. Fischer, T. Litz, A. Waag, and W. Hanke. "*Band structure of BeTe: A combined experimental and theoretical study*". *Phys. Rev. B* **58** (1998), p. 10394.

[97] G. N. Aliev, R. M. Datsiev, S. V. Ivanov, P. S. Kop'ev, R. P Seisyan, and S. V. Sorokin. "*Optics and magneto-optics of ZnSe heteroepitaxial layers*". *J. Cryst. Growth* **159** (1996), p. 523.

[98] M. Isshiki. "*Photoluminescence and cyclotron resonance studies on highly purified ZnSe single crystals*". *J. Cryst. Growth* **86** (1988), p. 615.

[99] J. H. Davies. *The Physics of low-dimensional Semiconductors*. Cambridge University Press, 1998.

[100] A. A. Maksimov. *private communication*.

[101] M. Lafrentz, D. Brunne, B. Kaminski, V. V. Pavlov, A. V. Rodina, R. V. Pisarev, D. R. Yakovlev, A. Bakin, and M. Bayer. "*Magneto-Stark Effect of Excitons as the Origin of Second Harmonic Generation in ZnO*". *Phys. Rev. Lett.* **110** (2013), p. 116402.

[102] J. Brandt, D. Fröhlich, C. Sandfort, M. Bayer, H. Stolz, and N. Naka. "*Ultranarrow Optical Absorption and Two-Phonon Excitation Spectroscopy of Cu_2O Paraexcitons in a High Magnetic Field*". *Phys. Rev. Lett.* **99** (2007), p. 217403.

[103] D. D. Sell. "*Resolved Free-Exciton Transitions in the Optical-Absorption Spectrum of GaAs*". *Phys. Rev. B* **6** (1972), p. 3750.

[104] W. R. L. Lambrecht, A. V. Rodina, S. Limpijumnong, B. Segall, and B. K. Meyer. "*Valence-band ordering and magneto-optic exciton fine structure in ZnO*". *Phys. Rev. B* **65** (2002), p. 075207.

[105] A. Mang, K. Reimann, and St. Rübenacke. "*Band gaps, crystal-field splitting, spin-orbit coupling, and exciton binding energies in ZnO under hydrostatic pressure*". *Solid State Commun.* **94** (1995), p. 251.

[106] M. Lafrentz, D. Brunne, A. V. Rodina, V. V. Pavlov, R. V. Pisarev, D. R. Yakovlev, A. Bakin, and M. Bayer. "*Second-harmonic generation spectroscopy of excitons in ZnO*". *Phys. Rev. B* **88** (2013), p. 235207.

[107] C. Klingshirn. "*ZnO: From basics towards applications*". *Phys. Status Solidi B* **244** (2007), p. 3027.

[108] Ü. Özgür, Ya. I. Aliov, C. Liu, A. Teke, M. A. Reshchikov, S. Dogan, V. Avrutin, S.-J. Cho, and H. Morkoc. "*A comprehensive Review of ZnO Materials and Devices*". *J. Appl. Phys.* **98** (2005), p. 041301.

[109] T. Makino, Y. Segawa, M. Kawasaki, A. Ohtomo, R. Shiroki, K. Tamura, T. Yasuda, and H. Koinuma. "*Band gap engineering based on $Mg_xZn_{1-x}O$ and $Cd_yZn_{1-y}O$ ternary alloy films*". *Appl. Phys. Lett.* **78** (2001), p. 1237.

[110] T. Makino, Y. Segawa, M. Kawasaki, and H. Koinuma. "*Optical properties of excitons in ZnO-based quantum well heterostructures*". *Semicond. Sci. Technol.* **20** (2005), p. 78.

[111] A. Ohtomo, M. Kawasaki, T. Koida, K. Masubuchi, H. Koinuma, Y. Sakurai, Y. Yoshida, T. Yasuda, and Y. Segawa. "*$Mg_xZn_{1-x}O$ as a II-VI widegap semiconductor alloy*". *Appl. Phys. Lett.* **72** (1998), p. 2466.

[112] A. Ohtomo, M. Kawasaki, I. Ohkubo, H. Koinuma, T. Yasuda, and Y. Segawa. "*Structure and optical properties of ZnO/$Mg_{0.2}Zn_{0.8}O$ superlattices*". *Appl. Phys. Lett.* **75** (1999), p. 980.

[113] C. Morhain, T. Bretagnon, P. Lefebvre, X. Tang, P. Valvin, T. Guillet, B. Gil, T. Taliercio, M. Teisseire-Doninelli, B. Vinter, and C. Deparis. "*Internal electric field in wurtzite ZnO/$Zn_{0.78}Mg_{0.22}O$ quantum wells*". *Phys. Rev.* **112** (1958), p. 1555.

[114] C. Xia, H. Zhang, J. An, S. Wei, and Y. Jia. "*Tunable built-in electric field and optical properties in wurtzite ZnO/MgZnO quantum wells*". *Phys. Lett. A* **378** (2014), p. 2251.

[115] F. Bernardini and V. Fiorentini. "*Macroscopic polarization and band offsets at nitride heterojunctions*". *Phys. Rev. B* **57** (1997), R9427.

[116] T. Bretagnon, P. Lefebvre, T. Guillet, T. Taliercio, B. Gil, and C. Morhain. "*Barrier composition dependence of the internal electric field in ZnO/$Zn_{1-x}Mg_xO$ quantum wells*". *Appl. Phys. Lett.* **90** (2007), p. 201912.

[117] M. Leroux, N. Grandjean, J. Massies, B. Gil, P. Lefebvre, and P. Biegenwald. "*Barrier-width dependence of group-III nitrides quantum-well transition energies*". *Phys. Rev. B* **60** (1999), p. 1496.

[118] G. Blattner, C. Klingshirn, R. Helbig, and R. Meinl. "*The Influence of a Magnetic Field on the Ground and Excited States of Bound Exciton Complexes in ZnO*". *Phys. Status Solidi B* **107** (1981), p. 105.

[119] J. Gutowski, N. Presser, and I. Broser. "*Acceptor-exciton complexes in ZnO: A comprehensive analysis of their electronic states by high-resolution magnetooptics and excitation spectroscopy*". *Phys. Rev. B* **38** (1988), p. 9746.

[120] *Landolt-Börnstein, New Series, Group III, Vol. **17B**, **22**, **41B***. Springer, Heidelberg, Berlin, Editor U. Rössler, 1999.

[121] T. Makino, K. Tamura, C. H. Chia, Y. Segawa, M. Kawasaki, A. Ohtomo, and H. Koinuma. "*Radiative recombination of electron-hole pairs spatially separated due to quantum-confined Stark and Franz-Keldish effects in ZnO/$Mg_{0.27}Zn_{0.73}O$ quantum wells*". *Appl. Phys. Lett.* **81** (2002), p. 2355.

[122] J. Puls, S. Sadofev, and F. Henneberger. "*Trions in ZnO quantum wells and verification of the valence band ordering*". *Phys. Rev. B* **85** (2012), p. 041307.

[123] H. D. Sun, Y. Segawa, T. Makino, C. H. Chia, M. Kawasaki, A. Ohtomo, K. Tamura, and H. Koinuma. "*Observation of Biexciton Emission in ZnO/ZnMgO Multi-Quantum Wells*". *Phys. Status Solidi B* **229** (2002), p. 867.

[124] J. M. Hvam, G. Blattner, M. Reuscher, and C. Klingshirn. "*The Biexciton Levels and Nonlinear Optical Transitions in ZnO*". *Phys. Status Solidi B* **118** (1983), p. 179.

[125] H. D. Sun, T. Makino, N. T. Tuan, Y. Segawa, Z. K. Tang, G. K. L. Wong, M. Kawasaki, A. Ohtomo, K. Tamura, and H. Koinuma. "*Stimulated emission induced by exciton-exciton scattering in ZnO/ZnMgO multiquantum wells up to room temperature*". *Appl. Phys. Lett.* **77** (2000), p. 4250.

[126] G. Coli and K. K. Bajaj. "*Excitonic transitions in ZnO/MgZnO quantum well heterostructures*". *Appl. Phys. Lett.* **78** (2001), p. 2861.

[127] M. Fiebig, D. Fröhlich, and Ch. Pahlke-Lerch. "*Multiphoton Polariton Spectroscopy on ZnO*". *Phys. Status Solidi B* **177** (1993), p. 187.

[128] D. Fröhlich, F. Heidrich, H. Künzel, G. Trendel, and J. Treusch. "*Cesium-Trihalogen-Plumbates a new Class of Ionic Semiconductors*". *J. Lumin.* **18/19** (1979), p. 385.

[129] C. J. Bradley and A. P. Cracknell. *The Mathematical Theory of Symmetry in Solids*. Clarendon Press, Oxford, 1972.

List of Figures

List of Tables

Symbols and Abbreviations

BBO beta barium borate

BCC body-centered cubic

CCD charge coupled device

FCC face-centered cubic

FWHM full width at half maximum

MQW multiple quantum well

OPA optical parametric amplifier

PL photoluminescence

PLE photoluminescence excitation

RA regenerative amplifier

SFG sum-frequency generation

SHBC second harmonic bandwidth compressor

SHG second harmonic generation

THG third harmonic generation

TPA two-photon absorption

Yb:KGW ytterbium-doped potassium gadolinium tungstate

List of Publications

[A1] D. R. Yakovlev, W. Warkentin, J. Mund, V. V. Pavlov, A. V. Rodina, R. V. Pisarev and M. Bayer, *Novel mechanisms of optical harmonic generation on excitons in semiconductors*, *Proc. SPIE 9503* Nonlinear Optics and Applications IX **950302** (2015)

[A2] D. Feng, D. R. Yakovlev, V. V. Pavlov, A. V. Rodina, E. V. Shornikova, J. Mund, and M. Bayer, *Dynamic Evolution from Negative to Positive Photocharging in Colloidal CdS Quantum Dots*, *Nano Letters* **17**, 2844 (2017)

[A3] A. Riefer, N. Weber, J. Mund, D. R. Yakovlev, M. Bayer, A. Schindlmayr, C. Meier, and W. G. Schmidt, *Zn-VI quasiparticle gaps and optical spectra from many-body calculations*, *J. Phys.: Condens. Matter* **29**, 215702 (2017)

[A4] D. R. Yakovlev, V. V. Pavlov, A. V. Rodina, R. V. Pisarev, J. Mund, W. Warkentin, and M. Bayer, *Exciton Spectroscopy of Semiconductors by the Method of Optical Harmonics Generation (Review)*, *Fizika Tverdogo Tela* **60**, 1463 (2018)

[A5] W. Warkentin, J. Mund, D. R. Yakovlev, V. V. Pavlov, R. V. Pisarev, A. V. Rodina, M. A. Semina, M. M. Glazov, E. L. Ivchenko, and M. Bayer, *Third harmonic generation on exciton-polaritons in bulk semiconductors subject to a magnetic field*, *Phys. Rev. B* **98**, 075204 (2018)

[A6] J. Mund, D. Fröhlich, D. R. Yakovlev, and M. Bayer, *High-resolution second harmonic generation spectroscopy with femtosecond laser pulses on excitons in Cu_2O*, *Phys. Rev. B* **98**, 085203 (2018)

[A7] J. Mund, Ch. Uihlein, D. Fröhlich, D. R. Yakovlev, and M. Bayer, *Second harmonic generation on the yellow 1S exciton in Cu_2O in symmetry-forbidden geometries*, *Phys. Rev. B* **99**, 195204 (2019)

[A8] A. Farenbruch, J. Mund, D. Fröhlich, D. R. Yakovlev, M. A. Semina, M. M. Glazov, and M. Bayer, *Nonlinear magneto optics of excitons in Cu_2O*, in preparation for *Phys. Rev. B*

Acknowledgements

It is time to thank all the people who supported me in one way or another in writing this thesis.

I am especially grateful to Prof. Dr. Dmitri R. Yakovlev for giving me the opportunity to do research under his guidance and for his continuous advice. I thank Prof. Dr. Manfred Bayer for providing me the chance to work and learn at E2 since my bachelor thesis. I very much appreciate all efforts by Prof. Dr. em. Dietmar Fröhlich in unravelling group theory to me in many fruitful discussions and a never ending motivation for new experiments on Cu_2O. In this context I want to thank Dr. Uihlein, too, for further discussions and insights.

Many thanks to our Russian colleagues, particularly Prof. Dr. Victor V. Pavlov, Prof. Dr. Roman V. Pisarev, Dr. Marina A. Semina and Prof. Dr. Mikhail M. Glazov, for discussion and interpreting data.

I would also like to thank Michaela Wäscher, Nina Sesemann-Collette and Katharina Sparka for great support in all administrational issues. None of the research in this thesis would have been possible without the work of Lars Wieschollek, Daniel Tüttmann and Klaus Wiegers. Therefore, many thanks for the continuous flow of helium and technical support.

Thanks to Andreas Farenbruch and Julian Heckötter for the nice atmosphere in the office and discussions about Γ_4 and Γ_5. Only you can understand how life at the Γ-point feels. A big "thank you" to all the members of the E2-chair, you made this more than half a decade of experimenting a most thrilling experience.

However, there is more in life than sitting in the lab. Thus, many thanks to the Hochschulsport for hours and hours of sports throughout countless evenings.

Finally, there is also more in life than being at the university. Therefore, I would like to thank my parents, Ute Mund and Dr. Karsten Mund, and my brother Christian Mund for their enormous support ever since. I thank Maxime Eppendorf for preventing me from going to the lab too often at weekends. Nuff respect and blessings to my friends for the good time - and sorry, too - I had no luck, neither in inventing the yellow laser, nor the laser sword.